Thesis for the Degree of Doctor of Philosophy

In Silico Studies of Carbon Nanotubes and Metal Clusters

Anders Börjesson

UNIVERSITY OF GOTHENBURG

Department of Physics,
University of Gothenburg
SE-412 96, Gothenburg, Sweden
Göteborg 2010

In silico studies of carbon nanotubes and metal clusters
Anders Börjesson
Doktorsavhandling vid Göteborgs Universitet
Avhandlingen ingår i serien: Skrifter från Högskolan i Borås, nr. 26
ISSN 0280-381X
ISBN 978-91-628-8204-4

Department of Physics,
University of Gothenburg
SE-412 96, Gothenburg
Sweden
Telephone: +46 (0)31 772 1000

The project was mainly conducted at:

UNIVERSITY OF BORÅS
SCIENCE FOR THE PROFESSIONS

School of Engineering,
University of Borås
SE-501 90, Borås
Sweden
Telephone: +46 (0)33 435 4000

Typeset in LaTeX

All figures were created using free software, e.g., GIMP, XMgrace and POV-Ray.

Printed at Chalmers Reproservice
Chalmers University of Technology
Göteborg, Sweden 2010

In Silico Studies of Carbon Nanotubes and Metal Clusters

Anders Börjesson
Department of Physics
University of Gothenburg
SE-412 96, Gothenburg, Sweden

Abstract

Carbon nanotubes have been envisioned to become a very important material in various applications. This is due to the unique properties of carbon nanotubes which can be exploited in applications on length scales spanning from the nano world to our macroscopic world. For example, the electronic properties of carbon nanotubes makes them utterly suitable for nano electronics while the strength of them makes them suitable for reinforcements in plastics. Both of these applications do however require the ability for systematic production of carbon nanotubes with certain properties. This is called selective carbon nanotube growth and today this has not been achieved with total success.

In the work presented in the thesis several different computational methods have been applied in our contribution to the systematic search for selective carbon nanotube growth. Put in a context of previous knowledge about carbon nanotube growth our results provide valuable clues to which parameters that control the carbon nanotube growth. In association with the latest results we even dare to, with all modesty, speculate about a plausible control mechanism.

The studies presented in the thesis addressed different stages of carbon nanotube growth, spanning from the properties affecting the initiation of the growth to the parameters affecting the termination of the growth. In some more detail this included studies of the melting temperatures of nanoscaled metal clusters. The expected size dependence of the melting temperatures was confirmed and the melting temperatures of clusters on substrates were seen to depend both on the material and shape of the surface. As this constitute the premises prior to the carbon nanotube growth it was followed by studies of the interaction between carbon nanotubes and metal clusters of different size and constitution. This was done using different computational methods and at different temperatures. It soon became apparent that the clusters adapted to the carbon nanotube and not *vice versa*. This held true irrespectively of the constitution of the cluster, that is for both pure metal and metal carbide. It was also seen that there exist a minimum cluster size that prevent the carbon nanotube end from closing. Closure of the carbon nanotube end is likely to lead to the termination of the growth which lead to studies of other reasons for growth termination, e.g., Ostwald ripening of the catalyst particles. This was investigated with the result that the rate of the Ostwald ripening may depend on both the chirality and diameter of the carbon nanotubes. It is suggested that this may provide some answers to the controlled growth of carbon nanotubes.

Keywords: Carbon nanotubes, metal clusters, melting temperatures, nanotechnology, molecular dynamics, Monte-Carlo, tight binding, density functional theory.

Appended Papers

This thesis is based on the work reported in the following publications, which are referred to by their roman numerals:

I A. Börjesson, S. Curtarolo, A. R. Harutyunyan and K. Bolton, Computational study of the thermal behaviour of iron clusters on a porous substrate, Physical Review B **77**, 115450 (2008)

II A. Börjesson, W. Zhu, H. Amara, C. Bichara and K. Bolton, Computational studies of metal-carbon nanotube interfaces for regrowth and electronic transport, Nano Letters **9**, 1117-1120 (2009)

III A. Börjesson and K. Bolton, First principles studies of the effect of nickel carbide catalyst composition on carbon nanotube growth, J. Phys. Chem. C 114, 18045-18050 (2010)

IV W. Zhu, A. Börjesson and K. Bolton, DFT and tight binding Monte Carlo calculations related to single-walled carbon nanotube nucleation and growth, Carbon **48**, 470 (2010)

V A. Börjesson and K. Bolton, First principles studies of the effect of Ostwald ripening on carbon nanotube chirality distributions, submitted 2010

VI A. Börjesson and K. Bolton, Modelling of Ostwald ripening of metal clusters attached to carbon nanotubes, manuscript in preparation 2010

These publications are printed in the appendix.

AB's contributions to the appended papers:

Paper I - AB developed parts of the computer program, performed the simulations, led the analysis of the results and wrote the paper.
Paper II - AB performed the Monte Carlo simulations, led the analysis of the results and wrote the paper.
Paper III - AB performed all calculations, led the analysis of the results and wrote the paper.
Paper IV - AB performed the tight binding simulations and contributed to the analysis of the results.
Paper V - AB designed and performed all calculations, led the analysis of the results and wrote the paper.
Paper VI - AB developed the model, performed the calculations, led the analysis of the results and wrote the paper.

Publications by the author which are not included since they are beyond the scope of the thesis:

1 A. Jiang, N. Awasthi, A. N. Kolmogorov, W. Setyawan, A. Börjesson, K. Bolton, A. R. Harutyunyan, and S. Curtarolo, Theoretical study of thermal behaviour of free and alumina-supported Fe-C nanoparticles, Phys. Rev. B **75**, 205426 (2007)

2 K. Bolton, F. Ding, A. Börjesson, W. Zhu, H. Duan, A. Rosen, A. R. Harutyunyan, and S. Curtarolo, Computational studies of catalytic particles for carbon nanotube growth, Journal of Theoretical and Computational Nanoscience, **6**, 1-15 (2009)

3 K. Bolton, A. Börjesson, W. Zhu, H. Amara and C. Bichara, DFT and Tight Binding based Dynamical Studies of Carbon-Metal Systems of Relevance to CNT Growth, Nano Research, **2**, 774 (2009)

4 K. Bolton, A. Börjesson, P. Ahlström and F. Bazooyar, Jubileumsskrift vid Högskolan i Borås (2009)

5 K. Bolton and A. Börjesson, SNIC Progress Report 2008-2009.

All data presented in the thesis originate from data acquired by the author unless otherwise stated.
All figures are the original art work of the author unless otherwise stated.

Contents

CHAPTER 1

Introduction

Carbon nanotubes (CNTs) is fascinating material with extraordinary mechanical, electrical and thermal properties. These properties have spurred an enormous interest in CNTs within the scientific community and over the past (almost) twenty years numerous potential applications of CNTs have been proposed. The nature of these applications span from products now available on the market, e.g., bicycles with CNT reinforced frames, to products seemingly taken from science fiction novels, e.g., space elevators. Irrespectively of how realistic the applications are they do require the ability to produce large amounts of CNTs, preferably of high quality at a low cost. Although it is possible make a recipe on how to produce CNTs this is an issue that is complicated by the existence of numerous different types of CNTs with different properties, something that may be particularly important for construction of electronic devices as the electronic properties vary with the CNTs. To this date, the parameters controlling the CNT production, often referred to as CNT growth, remain elusive and despite the enormous effort put into to solve this problem, no standard method has been proposed for the production of a specific type of CNT. Due to the large number of parameters that may be of importance to the CNT growth, it is necessary to investigate each of these parameters in a systematic way to understand how that parameter affect the CNT growth.

This thesis is dedicated to computational studies of some parameters that are of importance throughout the CNT growth process, i.e., parameters that may affect the initiation as well as the termination of the CNT growth.

The thesis is divided into three main sections where the first will give the reader an introduction to CNTs and previous computational studies of CNTs. In this section, the remarkable mechanical and electrical properties are discussed in some detail as well as one of the most common production methods. Since the thesis is dedicated to computational studies, a few general computational methods are introduced and it is then discussed how these methods can be applied to systems involving CNTs. This discussion includes several different situations, spanning from the properties prior to growth to direct simulations of CNT growth.

The second section of the thesis will introdue the computational tools used through the course of this work. Since many different computational methods have been used, this section

does only provide a brief overview while the details are found in the references. To a large extent this section reflect my contribution to the studies and computational implementations. For the parts where I have been involved in the writing of the computational program, some more details are given while for the methods where I have not contributed to the writing of the computational software, e.g., the density functional theory section, only the details needed to understand the premises and parameters of the calculations are discussed. Some discussions, e.g., the section about plane wave basis sets, do however contain more information since I failed to make them comprehensible with less information.

The third and last part of the thesis contain a short review of the results obtained during these years. This section is based on the material in six papers which are appended to the thesis. In this section, I have tried to avoid having a large overlap with the appended papers. Instead, some extra material that was not included in the papers has been provided as well as a short presentation the most interesting results. The focus of the discussions in this part of the thesis may be slightly different from the publication, e.g., following some loose ends that were not throughly discussed in the papers. I have tried to present the content of the appended papers in both a chronological order as well as following a red thread, starting from the clusters used as catalysts followed by studies of individual CNTs to end in a discussion of relevance to large CNT systems. Also this section reflect my contributions to the studies. For example, the discussions of Papers I and II are rather long since much time and hard work was spent before the these results became real. On the other hand, the discussion of Paper IV is slightly shorter since my contribution to this work was not as large.

As a short review of the focus of the calculations, the first appended paper discuss whether the metal clusters used as catalysts for CNT growth are solid or liquid during the growth. It was also elucidated how the melting temperatures of the clusters are affected by the introduction of substrate on which the clusters are mounted. In Papers II - IV this is followed by discussions of the properties of existing CNTs that have been attached to clusters. Here the geometries of the systems are discussed as well as the stability when they are attached to clusters with different properties, e.g., size and carbon content. Some of the knowledge acquired from these studies was then transfered to studies of large ensembles of CNTs. In Papers V and VI the question of what will happen to the clusters if atoms are allowed to diffuse between the different clusters was addressed by two different methods. This provided some information about what may happen to these systems after long time.

Finally, some ongoing projects are presented in order to give an outlook of what work that will be performed in the near future.

Anders Börjesson
Krokslätt, October 22, 2010

CHAPTER 2

Background

The earths crust contain only 0.025% carbon making it, by weight, the nineteenth most abundant element on earth[1]. Despite this moderate concentration carbon is one of the most important elements found in nature. All living organisms contain carbon and for us humans this means that most food and drinks (except water) contain carbon as well as many of the materials we have around us, e.g. soil, wood, plastics and petroleum products. If a material does not contain carbon, it is not uncommon to add it in order to change the properties of the material, e.g. the addition of carbon to iron in order to form steel[2]. All these compounds, exhibiting completely different properties indicate that carbon has rather unique properties and an ability to form chemical bonds to many other elements. To this day, more than a million carbon compounds have been described in the chemical literature[1].

Carbon has not only an ability to form molecules with other elements but also pure carbon has the possibility to form aggregates of very different structure and properties. In nature (at least) three such carbon forms, called allotropes, are found. The most abundant form may be the the amorphous structure soot while the crystalline forms graphite and diamond are less common. Schematic pictures of graphite and diamond can be seen in Fig. 2.1. In addition to the commonly occurring allotropes, new carbon allotropes have been synthesised in laboratories [3], e.g. carbyne, fullerenes, nanotubes, graphene, carbon foams, fibers and onions

One new carbon allotrope was first synthesised in 1985 when Kroto *et al.* [4] reported about the discovery of the Buckminster Fullerene (C_{60} fullerene). In succeeding studies other C_x molecules have been synthesised and this class of C molecules are now referred to as fullerenes. These can be described as a hollow sphere or ellipsoid where the surface is a one atom thick carbon structure. For the special case of the Buckminster fullerene, it can be compared to a football sewn from a number of hexagonal and pentagonal leather pieces. In the fullerene, the carbon atoms are positioned at the intersection where three seams meet. A schematic picture of the structure of a C_{60} fullerene can be seen in Fig. 2.1.

Reports of another synthetic carbon allotrope came in 1991 when Iijima *et al.* described the material now known as carbon nanotubes (CNTs)[5]. The CNTs can be described as an extremely elongated ellipsoid fullerene, forming a hollow tube. In an every day comparison

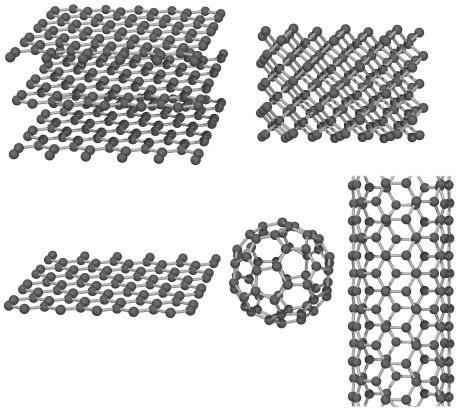

Figure 2.1: Schematic pictures of different forms of pure carbon. Top row from left, graphite and diamond. Bottom row from left, a graphene sheet, a fullerene (C_{60}) and a carbon nanotube.

a nanotube can be compared to a roll of net (e.g.,. the Swedish hönsnät) where a hexagonal mesh is formed by metal wires. In the CNT, the carbon atoms are located in the junction between wires, i.e. where three wires meet. The typical structure of a CNT can be seen in Fig. 2.1. One important difference between the CNT and the roll of net is the diameter scales. While the net is truly a macroscopic object with diameters in the order of meters, the CNTs have diameters in the nano meter scale, i.e., it is a size difference of 1 billion times.

A more recent progress in the field of carbon research is the experimental production of graphene[6] which can be described as a carbon sheet with the thickness of one atomic layer This can be compared to the unrolling of the previously mentioned net and a schematic image of a graphene sheet seen on the bottom row to the right of Fig. 2.1.

2.1 Carbon nanotubes

In this section, some interesting properties of CNTs will be discussed and some potential applications as well as some of the difficulties obstructing the realisation of these applications will be mentioned. Finally, some computational studies of CNT related systems will be mentioned. This will constitute the background of the work presented later in the thesis.

Carbon nanotubes comes in many variations which together present a wide variety of properties. One first distinction can be made into single walled carbon nanotubes (SWNTs) and multi walled carbon nanotubes (MWNTs). A SWNT can be described as the roll of net mentioned above while a MWNT can be described as several SWNTs, with different diameters that are inserted into eachother to form a telescopic structure. A schematic picture of a MWNT, constructed of three SWNTs, is seen in Fig. 2.2. The work presented in this thesis has involved SWNTs only and for that reason the MWNTs will not be discussed further.

The idea that a SWNT can be thought of as a cylinder rolled from a rectangular graphene sheet can also be helpful to understand another property of SWNTs, called the chirality. The chirality of a SWNT is a description of the structure of the SWNT, i.e., a description of how the C atoms are positioned in relation to eachother and the SWNT orientation. This

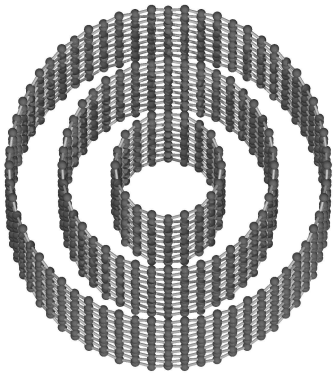

Figure 2.2: A schematic illustration of a MWNT constructed from three SWNTs.

is illustrated in Fig. 2.3 where one rectangular graphene sheet has been used to fold two different SWNTs. From the figure, it is clear that the rolling the sheet around the horizontal axis leads to a SWNT with a completely different structure compared to rolling around the vertical axis. For every SWNT, this difference in structure (chirality) can be characterised by two chiral indices, (n, m) where $n \geq m$[7]. The chiral indices can be understood as the vector, called chiral vector, that will constitute the base of the CNT upon cutting and rolling the graphene sheet, i.e., the sheet should be rolled around a vector that is perpendicular to the chiral vector. In Fig. 2.4, the chiral vectors

$$\mathbf{C} = n\mathbf{a}_1 + m\mathbf{a}_2 \tag{2.1}$$

of three different SWNTs are plotted in a graphene sheet. The chiral vectors are described in a basis that is constructed from the orientation of the graphene sheet. Here the the basis vectors $(\mathbf{a}_1, \mathbf{a}_2)$ are seen in the figure and in this basis the chiral indices for the three SWNTs are $(10, 0)$, $(8, 2)$ and $(5, 5)$. These three CNTs are seen in the bottom of Fig. 2.4 and the structural difference is apparent. The $(10, 0)$ has a sawtooth like zig-zag end which is a common property of all CNTs with chirality $(n, 0)$. These CNTs are referred to as zig-zag CNTs. The end of the $(5, 5)$ CNT show a structure that resembles an armchair and all CNT with chirality (n, n) are called armchair nanotubes. All other CNTs, with chirality (n, m), $n \neq m$, $m \neq 0$, do not have individual names but are referred to as chiral SWNTs. In the previous section it was mentioned that CNTs are nanosized materials but this is only partially true. The diameters of SWNTs span from 4.3Å[8] to a few nanometers while MWNTs have slightly larger diameters, although still on the nanoscale. The lengths of CNTs span from the nano scale, having only one carbon ring in the smallest molecules resembling a CNT [9], to the dm scale[10]. This means that that the length of the SWNT may be of the order of a billion times the diameter.

2.1.1 Mechanical properties

Carbon nanotubes are the strongest materials known today [11, 12] with a confirmed tensile strength that exceeds that of carbon fibres [13, 14] and with predictions of even higher tensile strengths[15]. This unique strength could be exploited by using CNTs as reinforcements in other materials, much in the same way as carbon fibres are used today.

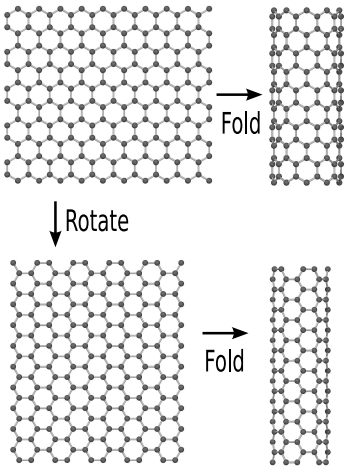

Figure 2.3: A schematic illustration showing how two SWNTs with different chiralities can be folded from the same graphene sheet. When folding the graphene sheet in the top row around the vertical axis a $(10, 0)$ SWNT is obtained. In the bottom row, the graphene sheet has been rotated 90° and folding around the vertical axis will now result in a $(5, 5)$ SWNT.

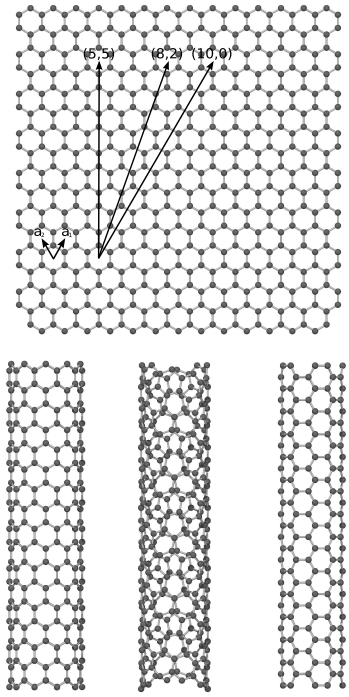

Figure 2.4: (top) The chiral vectors of $(10, 0)$, $(8, 2)$ and $(5, 5)$ SWNTs are plotted in a graphene sheet. The vectors are given in the basis $\mathbf{a}_1$ and $\mathbf{a}_2$ and the three SWNTs that could be obtained upon folding around a vector that is perpendicular to the chiral vector are shown (bottom). The chiralities of the SWNTs are from left to right $(10, 0)$, $(8, 2)$ and $(5, 5)$.

A recent report has showed that the effect of CNT reinforcement depends on both the length and the orientation of the CNTs and the most effective reinforcement is obtained with long, directionally aligned CNTs. Also the thermal and electronic conductance of the composites depend on the orientation of the CNTs[16]. Not only was there a difference for composites that were reinforced with CNTs of random and directional alignment but for the composite with directionally aligned CNTs, there was also a difference in the directions that were parallell and perpendicular to the CNTs. This means that CNTs can be used in the construction of materials that are conducting in one direction while they may be insulating in another direction.

Although CNTs are used as reinforcements today[17] there are a few obstructions to be overcome before CNTs can be used as reinforcements in the same extent as carbon fibres are used today. One such obstruction is that the strength of individual CNTs have not yet been transferred and utilised in CNT based composites. Composites with CNT reinforcement have shown strengths that are comparable to that of to carbon fibre reinforced composites[15] which means that much work remains before CNT reinforcement will become standard procedure.

A second, more practical obstruction is that the prices of CNTs today (May 2010) are relatively high, spanning from approximately 550 \$/kg for MWNTs to 80000 \$/kg for SWNTs[18]. These prices limit the use of CNTs in products in the mainstream price segment. This is especially crucial for the reinforcement of larger products requiring larger amounts if reinforcing material.

A very serious obstruction that must be considered before CNTs are introduced into society on a large scale are the possible negative health effects. Since the long CNTs have a constitution that is similar to asbestos, which is well known for it's negative impact on living organsims, it is necessary to evaluate the risks of CNTs with great care before repeating the mistake with asbestos. Reports have shown that CNTs may cause cell death[19] and that they have an asbestos-like behaviour[20]. This imposes a need of further studies of the health effects of CNTs.

2.1.2 Electrical properties

Also the electronic properties of CNTs are highly remarkable [12, 21–24]. For example, the chirality of a SWNT will determine whether it will exhibit a conducting or semiconducting behaviour. This has lead to the suggestion that CNTs may become important building blocks of the future nanoscaled electronics[25, 26].

Not only does the chirality determine whether the SWNTs are conductors or semi-conductors, it does also determine the band gap of the semi-conductors. This means that it is (in principle) possible to choose a material with a desirable bandgap as the building block of electronic components on the nano scale. Investigations have shown that a SWNT with chirality (n, m) will be metallic if $n - m = 3i$, where i is a non-negative integer, and semi conducting if $n - m \neq 3i$. The band gap has been shown to decrease with increasing diameter[23, 24] to finally approach the zero bandgap of graphene.

These trends in the band structure can be readily obtained by simple tight binding calculations, yielding analytical expressions for the energy levels[27–29]. These indicative results did not include any curvature effects but more sophisticated *ab initio* calculations have shown that for small CNTs, the curvature may affect the electronic structure of the CNTs[30]. For example, the $(4, 0)$ and $(5, 0)$ SWNTs which, according to the simple TB scheme, should be semi conducting are in fact metallic. It has also been seen that bundles of CNTs may exhibit

different electronic properties than the individual CNTs[31]

Another remarkable electronic property of CNTs is the low resistance for electronic transport. For comparison, CNTs can carry a current density that is orders of magnitude higher than the possible current density of copper[32], commonly used due to its good conductance properties. This makes CNTs appropriate for use as conductors in nano and micro scaled electronic applications but the low resistance may also be utilised in macroscopic applications, e.g. conducting composites.

2.2 Production of CNTs

As a few of the virtues of CNTs have been discussed, it has become apparent that CNTs have the potential of being an important material in many future applications. Although a few problems, such as the high cost and possible toxicity, were discussed the full extent of the problems of realising CNT based applications have not been considered yet. The problem concerning the production of large quantities of long CNTs of a certain chirality, preferably produced at a certain position in an electronic circuit, will be discussed in this section.

There are three common methods for CNT production called arc-discharge, laser ablation and chemical vapour deposition (CVD). In arc-discharge, the CNTs are produced in the soot formed after an arc discharge when passing a high current between graphite electrodes.

In the laser ablation method, a laser is used to evaporate carbon atoms from a graphite substrate. The carbon gas diffuses in the growth chamber and CNTs are formed during condensation.

These two methods will not be discussed further since the work presented in the thesis is more closely related to the circumstances of the CVD technique which will be discussed in some more detail.

2.2.1 Chemical vapour deposition

As the name chemical vapour deposition implies are atoms, initially in the gas (vapour) phase, deposited on a target material. For CNTs this means that feedstock molecules, containing carbon atoms, are usually decomposed in the vicinity of a metal particle acting as a catalyst for the decomposition. During the process, the C atoms will be deposited at the catalyst particle, which can be either free[33] or mounted on a substrate[34], while the residue of the feedstock, e.g., hydrogen atoms, may recombine and are thought to remain in the gas phase. Details of the CVD method have been reported in Refs. [34–37] and a more extensive review is found in Ref. [38]

The initial stages of CVD growth of CNTs are seen in the schematic illustrations in panels (a) and (b) of Fig. 2.5 where the feedstock molecules are deposited on a catalyst particle mounted on a substrate. The details of this stage of the CNT nucleation has remained a much debated issue where different sources state that the C atoms may either go in to the metal particle[39] or remain at the surface[40]. It appears reasonable to state that the catalyst particle become saturated with C before the CNT growth starts but it is not known wether the entire catalyst needs to be filled with carbon or if it is sufficient to form small carbon islands of the surface to nucleate growth.

For catalyst particles that are mounted on a substrate two different growth mechanism are possible. If the interaction between the catalyst and substrate is strong, the catalyst will remain attached to the substrate and the CNT will grow out from the catalyst particle[41, 42].

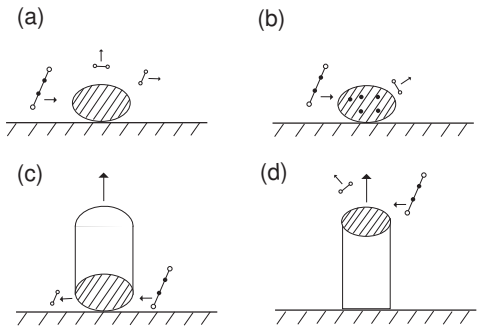

Figure 2.5: CNTs growing from a catalyst particle that has been mounted on a substrate. The feedstock molecules decompose (a) on the catalyst particle, saturates the catalyst (b) and nucleate a CNT. Panel (c) shows the base growth mechanism where the cluster remains on the substrate. Panel (d) show the top growth mechanism where the cluster lifts off and elevates at the top of the growing CNT.

This is referred to as the root growth mechanism. If the interaction between the catalyst and the substrate is weak, the nucleated CNTs will attach to the substrate while the metal particle will detach from the substrate and elevate at the top of the CNT[43, 44]. This growth mechanism is referred to as top growth. Schematic pictures of root growth and top growth are seen in panels (c) and (d) in Fig. 2.5 respectively.

A large number of parameters are known to affect the CVD growth mechanism as well as the properties of the CNTs grown. These parameters include the temperature, the feedstock, the catalyst material, the substrate and additional substances available in the growth chamber.

Typically, successful CVD growth of CNTs is achieved in the temperature window between 800K to 1200K. Lower temperatures have been seen to lead to carbon encapsulation of the catalyst[45] or defective CNTs[46] while higher temperatures appears to lead to formation of increased amounts of amorphous carbon structures[46]. Many of the finite temperature calculations presented later in the thesis were performed for temperatures around 1000K since this temperature is reasonable during CVD growth.

Some common feedstocks include methane[41, 47], acetylene[47] and ethanol[48] while e.g. fullerenes constitute a less common feedstock[49, 50]. Both the reactivity and molecular structure of the feedstock appears to be of importance for the growth process and quality of the grown CNTs. Certain feestocks, e.g., acetylene, require lower growth temperature than others. Larger molecules, e.g., fullerenes, decompose only partially which affects the characteristics of the grown C structure.

Common catalysts for CNT growth are Fe, Ni and Co or some alloy thereof[38], although there are recent reports telling about growth from other metals (e.g., Cu and Au)[51, 52] and semiconducting particles[53]. It has been suggested that the adhesion strength between the catalyst particle and the CNT is of great importance and that if the adhesion is too strong, the catalyst will become encapsulated while a weak adhesion will lead to detachment of the CNT[54].

Not only the constitution but also the size of the catalyst particle may be a parameter of importance for CNT growth [55–60]. The diameter of the catalysts have been reported to be slightly larger than the CNTs grown, typically $1.1 - 1.6$ times the CNT diameter.

Other important issues regarding the growth are the carbon diffusion from the decomposition site, on or near the catalyst surface, to the growing CNT[61]. Depending on the growth mechanism, this may be limited by the C diffusion rate in[62] or on[63] the catalyst particle.

The thermodynamic state of the catalyst particle[64] has been suggested as a factor of importance for the CVD growth. Although the bulk melting temperature of the catalyst is generally far above the temperatures relevant to CNT growth, numerous studies have shown that small size of the catalyst lead to a decrease in melting temperature[65–71].

Not only the direct properties of the catalyst particles are important for the CNTs but also the parameters that are induced by the substrate on which the catalysts have been mounted prior to CNT growth. Some common substrates are silicon, silicon carbide, aluminium and aluminium oxide[38]. The materials used as substrates may be flat[51, 52, 72] but may also contain defects such as protrusions and pores. In fact, porous substrates are often used for nanotube growth since they prevent diffusion of the catalyst particles. By the prevention of formation of larger particles, thin single-walled CNTs with a narrow diameter distribution can be grown[73]. Recent reports have shown that the diffusion of catalyst particles plays an important role in the termination of growth of CNTs[74, 75]. A complication, rather typical for the field of CNT growth, is that the same catalyst may exhibit a different behaviour depending on the substrate on which it is mounted on[76]. This means that the two growth parameters catalyst particle and substrate may not be chosen completely independently.

One factor that may limit the CNT yield is the life time of the catalyst particles. It has been seen that a small amount of water in the growth chamber has a positive effect on the growth of CNT forests[77, 78] by increasing the lifetime of the growth time. The addition of water has proved so valuable that it has been given a separate name, i.e. water assisted CVD growth or even super growth. Recent studies suggest that the water inhibit the diffusion of catalyst particles[74]. Another result of this study was that Ostwald ripening, i.e., growth of larger particles and shrinkage of smaller particles is observed in the absence of water.

2.2.2 Control of CNT growth

Despite the extensive research effort, the systematic production single chirality ensembles of SWNTs has not yet been achieved for any SWNT chirality. This means that the production of SWNTs with chosen chirality, desirable for electronic applications, has not been achieved either.

There are two plausible methods to achieve this task, either by choosing the CNT chirality prior to growth[73, 79] or by separation of nanotubes after growth[80–82]. In Ref.[83], a combination of the two methods has been used to achieve a production of $(8, 4)$ SWNTs with high purity.

It has been seen that CNT growth can be interrupted and then continued again after docking of nanometer sized metal particles to the open ends of the initial CNTs[84]. The new CNTs were seen to inherit the diameter and chirality of the initial CNTs. However, it is not yet known if one nanotube continue growing with the same chirality or if it is the overall distribution of chiralities that remains the same. In the study of Wang *et al*[84], it was also seen that the parent (initial) CNTs had to be handled with care in order for the continued growth to work in a satisfactory manner. This was assigned to the necessity of having an uncompromised CNT end to dock the metal particle on to.

CHAPTER 3

Computational studies of carbon nanotubes

Since this thesis is dedicated to computational studies of CNTs, it may be interesting present a short review of a few the computational efforts made this field. In general, computational studies can complement the experimental studies and deepen the understanding of CNTs by monitoring certain properties or stages, such as nucleation or growth, at an atomistic level. An advantage of computational modelling compared to experimental studies is that it allows for total control of specific parameters, such as temperature, pressure and atomic positions.

These positive aspects of computational modelling do not come for free but are also associated with a price that must be paid. In this case the price is time, referring to the time used on the computers and a calculation that require much time on the computers will be referred to as a computationally expensive calculation. The most crucial issue of an atomistic calculation is the description of the interactions between the atoms in the system, i.e., the potential energy of the system and the forces that act on the atoms. As discussed in more detail in chapter 4, this can be calculated in different ways having different computational cost and accuracy. In general the computational cost and accuracy are just two different currencies that can be exchanged, i.e. high accuracy generally means a high cost and *vice versa.*

3.1 An introduction to atomistic calculations and simulations

The basics of atomistic simulations and calculations will be outlined in this section while some details will be described in chapters 4 and 5. In the discussion, the interatomic interactions, also referred to as the potential energy surface(PES), will be divided into three categories depending on the level of physics included in the description. This categorisation may not be completely unambiguous but since it is commonly used it is worth keeping it in the discussion.

The first category contains the first principles, sometimes referred to as *ab initio*, calculations. This include methods like Hartree-Fock, post Hartree-Fock and quantum Monte-Carlo but in this thesis it will exclusively mean density functional theory (DFT). In general the first principles calculations are the most accurate since they take the full electronic structure , i.e. quantum mechanics, into account. However, it should be noted that even the first principles

methods rely heavily on approximations.

Moving a step down in cost and, generally a step down in accuracy, the semi empirical methods are reached. These take some quantum mechanics into account while other effects are modelled by empirical approximations. This makes the computations significantly faster than the first principles methods. These methods include tight binding (TB), density functional tight binding (DFTB), Hückel and PM3.

The final category contains the purely empirical methods, having no electronic structure at all but relying solely on how atoms are known to interact with eachother in a certain situation. These models are generally constructed by a sophisticated system of mathematical functions depending on the atomic surrounding, e.g., of the bonding distances and angles to other atoms. Two common models to describe the C-C interactions are the Brenner potential[85] and ReaxFF[86], both of which have been applied to studies of CNTs. The simplicity of these models make the calculations very fast although the accuracy is limited to qualitative trends. These models are very sensitive to changes of the chemical environment of the atoms. Usually the models perform well for situations similar to those considered when constructing the model while the performance is worse for other situations. This property is called the transferability of the model and while the first principles are highly transferable the empirical methods are less transferable, i.e., DFT should have a high performance for most situations while the empirical methods performs well only for few situations.

Not only the computational cost, accuracy and transferability of the potential energy surfaces vary but also the areas for which they are applicable. The applicability shows the same tendency as the accuracy, meaning that the first principles methods can formally, i.e. in theory, be used for many different types of calculations while the empirical methods are less useful. The empirical models are restricted to studies of the behaviour of atomic systems under certain conditions, e.g. temperature change, stress, introduction of new atoms etc., while the first principles methods are also able to reproduce the electronic structure of the material with all that comes with that, e.g. band structures, chemical reactions, conductance, magnetic properties etc.

Most atomistic first principles calculations of CNTs use an optimisation technique, e.g., quasi-Newton or conjugate gradient algorithms, to find the minimum energy structure of a certain system. This gives the opportunity to compare the minimum energies of different, but related, systems in order to evaluate which is the most stable, and hence the most likely to occur. Although structure optimisations do not provide information about the equilibrium properties of the system, they are helpful tools for DFT calculations where dynamical methods are unaffordable.

If the energy and force calculations are computationally cheap, there are two common methods to perform atomistic simulations at finite temperature. These techniques are called Molecular Dynamics (MD) and Monte Carlo (MC) simulations and the two are fundamentally different and hence suitable for different types of simulations.

Molecular Dynamics (MD) simulation is a technique to calculate numerical solutions to the classical equations of motion for the atomic nuclei. From a given initial atomic configuration, the system can then be propagated in time. Within the simulation time, dynamical properties can be studied as well as equilibrium properties, under the condition that the relaxation time lies well within the simulated time. For example, MD may be used to simulate the time evolution of systems containing metal and carbon which in time will grow as CNTs, i.e., a true simulation of CNT growth. The length of the simulated time is very much dependent of the size of the atomic system and on the type of interatomic interaction used.

For simple, empirical interactions the simulated time is typically limited to sub-microsecond trajectories while simulations with quantum interactions are even more limited (typically to ps trajectories).

Monte Carlo (MC) is the collective name of various computational methods used many different disciplines such as physics, chemistry, mathematics and finance[87] (and literature[88]). All MC methods make extensive use of random numbers (chance) and have been given the name after the famous casino. The atomistic MC methods are suitable for studies of equilibrium properties of atomic systems, for example structural properties, solubility and phase coexistence. An important difference to the MD method is that there is no time concept present in a MC simulation and the qualitative change of an atomic system during a MC simulation can not be interpreted as a change in time.

After the introduction of the finite temperature simulation methods it is no longer evident that the first principles methods are always preferred over an empirical method. This is due to the better statistical convergence of the faster methods, i.e., the accuracy of the PES must be put against the possibility to converge the simulation which may equally important for the calculation. Hence, a formally very accurate calculation may have little chemical meaning while a formally less accurate calculation may contribute with important qualitative information.

3.2 Carbon nanotubes

The great interest in CNTs has spurred an enormous effort in the theoretical calculations of different properties and applications of CNTs. In this section a few interesting computational studies on CNTs will be discussed with the focus on studies that provide a background to the studies presented in the appended papers.

This means that a large number of calculations on CNTs will be left without any discussion. These calculations include early predictions of band structure of the CNTs[23, 89, 90], structural data of MWNTs[91] and SWNT bundles[92],strain in and bending and buckling of CNTs[93–100], the junctions between CNTs[101–104] and between CNTs and metal[105–108]. While some of the calculations use highly sophisticated techniques to model quantum phenomenon e.g., conductance, other studies have shown that macroscopic concepts can be directly transferred to the nano scale, e.g., the CNT based piston engine[109–111].

Many of these results are discussed more extensively in Ref. [112].

3.3 Metallic systems - clusters and bulk

As mentioned in the previous chapter, successful CVD growth of CNTs takes place at temperatures around 1000 K where a feedstock is usually decomposed at a nanometer sized catalyst particle, being either free in vacuum or supported by a substate. It was also mentioned that the thermodynamic state of the catalyst particle may be an important parameter during CNT growth.

When considering Fe, being a common catalyst metal, as an example there should not be any need for studies of the state of the particle since a typical CVD growth temperature of 1000 K is significantly lower than the bulk melting temperature of Fe which is approximately 1800 K.

However, the bulk melting temperature may not be applicable when entering the nano scale and already in 1909[113] it was suggested that the melting temperature of finite systems depend on the size and that smaller particles should have melting temperature below the bulk melting temperature. Experimental studies have confirmed this melting behaviour for clusters supported on a substrate[114–117] and for free clusters[118, 119].

In parallell with the experimental work, numerous theoretical studies of the thermal properties of small particles have been performed. These studies have focused on free clusters[120–129], clusters on flat substrates [65–71] and clusters in confined geometries[130, 131].

Most of these calculations have been performed using MD simulations with empirical potential energy surfaces although MC simulations are possible as well[131].

The theoretical studies of free clusters agree with the experiments, stating that the melting temperature of finite sized clusters is lower than for bulk and that the melting temperature is inversely proportional to the particle diameter.

Comparisons between free clusters and clusters on a substrate have shown that that clusters that are mounted on a flat substrate tend to have a higher melting temperature than a free particle with the same number of atoms. This has been attributed to the geometrical change of the cluster that is induced by the substrate and it has been suggested that the size of the supported cluster is better described by an effective radius, corresponding to a larger cluster[66] with a higher melting temperature. The larger clusters were also seen to melt via a surface melting mechanism[129] while smaller clusters experience a dynamic coexistence between solid and liquid[70]. Surface curvature has also been discussed as a factor affecting the stability of the cluster[132] and hence the melting temperature.

The computational methods allow a detailed study of the atomic geometries and effects of atomic scale defects can be included. It has been discussed that particular cluster sizes exhibit melting temperatures which are higher than the slightly larger sizes[70]. This behaviour has been attributed to the higher geometrical stabilities of these clusters, causing the so called magic sizes to arise. Also the geometries of the magic numbers have been studied[133]. Two examples of the magic sizes are the Fe_{13} and Fe_{55} clusters consisting of an atom that has been encapsulated by one and two filled atomic shells.

Metal carbides may be important for CNT growth and the melting behaviour of metal carbides[134] have been studied using MD simulations. These calculations provided information about the phase diagrams and melting temperatures of the metal carbides. It was concluded that larger metal-carbide clusters may not be completely molten at the temperatures relevant for CNT growth.

Other data of relevance for CNT growth concern the diffusion rates of C in or on the catalyst metal. The diffusion of C atoms on Ni clusters have been studied using DFT calculations[135]. From comparisons of the diffusion paths of C atoms on the clusters surface, through the subsurface layers or through the bulk of the metal it was concluded that surface diffusion and subsurface diffusion are plausible while the bulk diffusion is more unlikely. Another study presented similar results[61] and added DFT information about the stability of feedstock molecules on the Ni surface. In addition to the lower C diffusion rate through the bulk, it was concluded that there is an energy barrier associated with the feedstock decomposition and that this may be a factor limiting the CNT growth. It has been suggested that the use of a feedstock with a lower dissociation barrier could be used to achieve CNT growth at lower temperatures[136]. Other DFT studies have reported similar results[137–141].

3.4 Carbon nanotubes and clusters

In order to understand the growth mechanism of CNTs it is important to understand what happen to the system between nucleation and growth termination.

One issue that may be of great importance is the carbon-catalyst, and CNT-catalyst, interactions. This has been studied in a number of DFT calculations[54, 142–144]. Total energy DFT calculations of different C structures were employed to determine the energetic preference to create different carbon structures at a metal surface[142]. It was concluded that the energy associated with the introduction of pentagon defects, i.e. curvature, in the C structure is overcome by a reduction of the number of dangling C bonds, i.e. lowering the energy. It should hence be favourable to nucleate a CNT cap instead of graphene flakes. In association with this, it has also been suggested that the chirality distribution of the SWNTs grown may be dependent on the stability and number of caps available for a specific chirality[145, 146]. The stability of the caps on the substrate may be important for the CNTs grown[143] and the matching of the end atoms of the CNT cap and a Ni surface could affect the stability of the cap on the surface. The stability was seen to differ for different CNT chiralities which led to the suggestion that this matching could play an important role in the formation of CNT caps at low temperature where the excess energy needed for certain caps may not be provided at the growth temperature. This means that CNT chiralities that have many energetically stable cap structures should be more abundant than CNT chiralities with fewer and less stable caps.

Other studies have discussed the importance of the adhesion between the CNT caps and metal[39, 54, 144, 147–149]. It was seen that the adhesion strength is expected to lie within a interval for CNT growth to be successful and that a weak adhesion would lead to detachment of the CNT while a strong adhesion would lead to encapsulation of the catalyst particle. It was seen that common catalyst metals, e.g. Ni, Co and Fe, have a stronger adhesion compared to, for example, Au. Studies of composite clusters have revealed that composites capable of CNT growth had CNT-composite adhesion strengths that were more comparable to the adhesion strength between CNTs and common catalyst metals[149].

It has also been seen that a metal ring is sufficient to study the CNT-metal adhesion which may be convenient compared to having a complete metal cluster as this leads to an increased number of electrons which in turn leads to increased computational cost for the first principles methods[144].

First principles calculations have been applied to study the stability of C atoms when included into existing CNT structures [150]. This study showed that it is energetically favourable to include C atoms on positions such that new hexagons are formed with as few intermedate steps as possible. This lead to the conclusion that the more such positions that are available, the faster the CNT should grow which in effect would mean that armchair CNTs should grow faster than zig-zag since there are more possible inclusion cites.

3.5 Simulated growth of carbon nanotubes

To understand CNT growth, it desirable to be able to simulate all stages of the CNT growth process, from C deposition on the catalyst via cap nucleation to cap liftoff and growth.

This highly intricate issue has been addressed by several research teams and a quite a few interesting results have been published. A more extensive review of MD simulations of CNT

growth if found in Ref. [151].

3.5.1 Empirical potential energy surfaces

Many empirical MD simulations have based the C-C interactions on the Brenner[85] or ReaxFF[86] force fields while the force fields describing the metal-metal and C-metal interactions have been developed by different research groups[152–154].

Some keypoint results of these simulations were that, at the early stages of CNT nucleation, the C atoms move into the cluster[153, 155]. When a sufficient amount of C is added to the system, the cluster becomes saturated and C polygons starts to form. The formation of these polygons can be either in[155] or on[153] the cluster. If formed on the cluster, these structures form graphitic islands that will facilitate the small CNT caps which lift off and grow as CNTs. The typical lengths of these simulations are in the order hundreds of ns and the attempted temperatures span from room temperature up to 2500 K. It has been seen that the growth temperature is of great importance for the structures produced[39] and that for low temperatures, the attraction between the graphitic islands and catalyst is not overcome and the cluster becomes encapsulated. At higher temperatures, the caps lift off but the number of defects of the grown C structure is radically increased[39].

The studies have shown that the diameter of the CNTs grown depend on the diameter of the catalyst particles[153], a relation is also found experimentally[55–60].

The importance of the substrate during CNT growth has been investigated by Balbuena *et al.*[156] who concluded that the increased melting point that is observed with stronger catalyst-substrate adhesion strength may affect the nucleation and growth of CNTs.

3.5.2 Semi-empirical potential energy surfaces

Tight binding Monte Carlo simulations by Amara *et al.*[157] have shown a similar growth mechanism as described above, with polygonal C structures forming a graphitic island on the catalyst surface. This study emphasised that the solubility of C atoms in Ni is, in agreement with abovementioned DFT results, limited to the subsurface layer. The cap formation took place only in a narrow interval of the chemical potential, which is correlated to the feedstock pressure. If the chemical potential (feedstock pressure) was too small, very limited C absorption on the surface was observed while if the the chemical potential was too large too much C was absorbed on the surface with the consequence of encapsulation of the metal particle. It was seen that C atoms forming sp^2 structures were more stable than other C atoms in the bulk or on the surface. The increased stability of these atoms is a likely to be a partial explanation of the cap lift off.

Tight binding MD simulations have been performed to study the continued growth of existing CNTs[158]. This study succeeded with continued CNT growth although the CNT chirality after the continued growth remained uncertain. It was seen that short C chains were added to the existing CNT and that these chains where then woven to a web that became part of the existing CNT.

The temperature dependence on the continued growth was studied and showed that a the CNT grow faster on a Fe cluster at temperature 1500K compared to 1000K and 2000K[159]. At the higher temperature, the deformation of the CNT became more pronounced while at the lower temperature, polygons and chains were formed but the clusters were not rejected, i.e., the polygons remained on the cluster surface. These studies were extended study the

CNT growth from a small cap fragment, available at the beginning of the simulation[160]. CNTs were seen to grow from the seeds and the series of calculations of continued growth and cap lift of support a growth mechanism where a cap fragment is nucleated, additional C atoms attach to the cap, the cap lift off and continue growth as a CNT. Comparisons between Fe and Ni as catalyst metals established that growth from the Ni nanoparticle was approximately twice as fast as growth from a Fe particle of the same size[161].

3.5.3 First-principles potential energy surfaces

Ab initio molecular dynamics simulations of CNT growth have been performed by Gaviellet[162] and by Raty *et al*[163]. During a simulation time of 25 ps the segregation of C and Co in a cluster was observed with C atoms diffusing from the cluster to the surface[162] where C strings and polygons were formed. Diffusion of C atoms on the surface was observed with the result that a few C atoms were incorporated into an existing cap structure at the end of the simulation.

Raty *et al*[163] reported of fast C diffusion on a Fe surface which resulted in the formation of a cap structure. It was also seen that the C solubility in Fe clusters was low, i.e, no C atoms were seen to dissolve into the cluster. In addition, studies of the formation of C strings on an Au surface showed that the weak C-metal adhesion make the strings leave the surface, i.e. no CNT cap structure was formed on the surface.

CHAPTER 4

Computational Methods

The concepts of atomistic calculations and simulations that were introduced in section 3.1 will be discussed in more detail in this chapter. The separation into empirical, semi-empirical and first principles energy calculations will be kept and discussed in the context of the methods used for the work presented in the thesis. This means that the force fields for Fe-Fe and Fe-Al_2O_3, used in Paper I, will represent the empirical methods, the fourth moment tight binding approximation, used in Paper II, will represent the semi-empirical methods and the density functional theory implementation in VASP, used in papers II - V, will represent the first principles methods. The idea with this chapter is not to provide extensive descriptions of the theoretical backround of the methods but rather to provide sufficient information in order to motivate the method of calculation, choice of parameters and methods of analysis.

4.1 Introduction to atomistic calculations

The starting point of an atomistic simulation (or calculation) is to construct an atomic structure, e.g., a CNT, that defines the positions of the atoms. This system is then subjected to some kind of manipulation, e.g. time evolution or relaxation, that require knowledge about the energy of the system and/or the forces that act on the atoms.

In general, the total energy of an atomic system can be obtained by solving the Schrödinger equation (or Dirac equation if relativistic effects are of importance) for the system. For a system with M atoms, each having having a number of electrons which in total sums up to N electrons for the entire system, this leads to a many-body problem with $3 \times (M + N)$ independent variables.

For any such system, the Schrödinger equation is given by

$$H|\Psi_i\rangle = E_i|\Psi_i\rangle \tag{4.1}$$

where H is the Hamiltonian operator, E_i is an energy eigenvalue and $|\Psi_i\rangle$ is an energy eigen state, which is the ground state if it is associated with the lowest energy eigen value. The

Hamiltonian operator is given by

$$H = -\frac{\hbar^2}{2m_e}\sum_i \nabla_i^2 - \sum_{i,l}\frac{Z_l e^2}{|\mathbf{r}_i - \mathbf{R}_l|} + \frac{1}{2}\sum_i\sum_{j\neq i}\frac{e^2}{|\mathbf{r}_i - \mathbf{r}_j|} - \frac{\hbar^2}{2}\sum_l \frac{\nabla_l^2}{M_l} + \sum_{l,k}\frac{Z_l Z_k e^2}{|\mathbf{R}_k - \mathbf{R}_l|} \quad (4.2)$$

under the assumption that no external fields are present. The terms in order are the kinetic energy of the electrons, the electrostatic potential between electron i and nuclei l, the electrostatic potential between electrons i and j, the kinetic energy of nuclei l and finally the electrostatic potential between two nuclei l and k. The Schrödinger equation constitutes a problem of such dignity that it can only be solved analytically for the hydrogen atom, i.e., a system where $M = 1$ and $N = 1$, while all other systems require some form of approximation. The need for approximations becomes apparent when considering one of system that was frequently used in work presented in the thesis. This system contained 80 C atoms and 55 Ni atoms which means that $M = 135$ and $N = 2020$.

4.2 The Born-Oppenheimer approximation

One helpful approximation is based on the argument that since the electrons are much lighter than the nuclei, they will move significantly faster than the nuclei. This means that the electrons will experience the potential from the atomic nuclei as a stationary Coulomb potential and that every move of the nuclei will result in an instantaneous reconfiguration of the electrons. The effect of this approximation is that the Hamiltonian can be separated into two parts, one for the energy the electrons, moving in the field from the nuclei, and one for the nuclei in which the electronic energy enters as a potential energy term. This separation is referred to as the Born-Oppenheimer (BO) approximation and means that total energy of the system can be calculated separately for the Born-Oppenheimer Hamiltonians of the electrons and ions respectively.

The BO approximation was adopted in all calculations presented in the thesis and the ions were exclusively treated as classical particles, i.e. all quantum effects not included in the potential energy due to the electronic system were neglected. The space of coordinates of the atomic nuclei is referred to as the configuration space of the atomic system and all sets of coordinates in configuration space that have the same potential energy are said to lie on a multidimensional surface called the potential energy surface (PES). If the BO approximation is adopted, the PES may also be referred to as the BO surface.

As discussed, the PES depends, trivially, on the Coulomb repulsions between atomic nuclei and on the the electronic BO-Hamiltonian. The latter can be treated in different ways taking electronic quantum effects into account either directly or indirectly. Three different approaches have been used in the work presented in the thesis. In the following sections, these well be presented with increasing complexity.

4.3 Basis sets

In order to find numerical wave functions of the Schrödinger equation (or the Kohn Sham equations), a common method is to introduce a basis set and then construct the wave functions as a linear combination of the basis states constituting the set. In the work presented in the thesis, this concept is used for both the TB and the DFT calculations and it may be

appropriate to introduce this general concept before introducing the empirical PES, although basis sets were not explicitly used in those calculations.

The introduction of basis sets means that the wave functions can be written as

$$\psi_a(\mathbf{r}) = \sum_k c_k^a \xi_k(\mathbf{r}) \tag{4.3}$$

where ξ_k is a basis state and c_k^a is the wavefunction's coefficient for this state. In this basis the Schrödinger equation can be written as

$$\sum_k \Big[-\frac{1}{2}\nabla^2 + V(\mathbf{r}) \Big] c_k^a \xi_k(\mathbf{r}) = \epsilon_a \sum_k c_k^a \xi_k(\mathbf{r}) \tag{4.4}$$

.

In principle, the wave function should be expressed in a Hilbert space, meaning that the basis set should be infinite in order to represent all possible wave functions. In practical (computational) calculations it is highly impractical to work with infinite basis sets and it is therefore necessary to truncate the basis set.

One way to do this is to consider the physics/chemistry of an atomic system and realise that electrons are most likely to be localised around the atomic nuclei and that there is no need to be able to express the wave function further away from the nuclei. It could also be realised that most changes of the wave functions (large spatial derivatives) occurs close to the nuclei while the behaviour is more stable further away from the nucleus. This means that much effort is needed to represent the wave function close to the nuclei, less effort is needed further away and no effort at all is needed far away from the nuclei. This has lead to the approach where the basis sets are composed of functions localised at the atomic nucleus. These basis sets can be Slater type orbitals (STOs)[28], Gaussians[28] or numerical orbitals, like the Fireball basis set implemented in the DFT program Siesta. In this approach the wave functions are constructed as a linear combination of orbitals that are localised at atoms, hence forming a linear combination of atomic orbitals (LCAO). The LCAO approach is adapted in TB calculations while the DFT calculations were performed using a plane wave basis that will be introduced later.

The standard method to obtain the wave function coefficients and eigenvalues is by diagonalization, being an $\mathcal{O}(N^3)$ method for matrices of dimensionality N. This scaling means it is desirable to keep the basis set as small (compact) as possible to enhance the computational speed while it should be as complete as possible to capture the physics as accurate as possible. Another type of truncation of the basis sets is discussed in association with plane waves in section 4.6.3

4.4 Empirical potential energy surfaces

One of the simplest empirical potential energy surfaces is known as the Lennard-Jones potential[164] which is given by the expression

$$V(r) = 4\epsilon\Big[\Big(\frac{\sigma}{r}\Big)^{12} - \Big(\frac{\sigma}{r}\Big)^{6}\Big] \tag{4.5}$$

where r is the distance between two atoms, ϵ is the depth of the potential well and $2^{1/6}\sigma$ is the equilibrium interatomic distance. This is an example of a pair-potential, i.e. the

potential energy depends only on the distance between two atoms and the total potential energy of the atomic system is then given as the sum of the potential from all atomic pairs. This type of potentials can not describe the structural properties of an atomic system in a sufficient manner, i.e., it is not sufficiently accurate to describe e.g., carbon or a metal in the solid state, where the crystal structure is very prominent. The potential is however a very practical tool that may be used in the preparation of input structures to other calculations, e.g., DFT, since the distance between atoms can be optimised. Although the geometry of the optimised structure may be unphysical it is preferable to random atomic positioning. It is also a practical way to describe the interaction between atoms and, e.g., surfaces, in a phenomenological way.

In order to incorporate structural and chemical properties, the PES has to be expanded to a more complex functional forms which takes the atomic surrounding into consideration. For example, this can be done by incorporating bonding angles and coordination numbers of the atoms. Examples of such PESs for carbon systems are Rebo[85] and ReaxFF[86]. For metals, examples of PESs are the potentials by Gupta[165] and Ercolessi[166]. Force fields for C-metal interactions have been developed by Zhao*et al.*[167] and Shibuta *et al.*[152].

4.4.1 The empirical Fe-Fe force field

The PES used for the MD simulations of Fe clusters, presented in Paper I can be written as a sum of Born-Mayer (first line in Eqn. 4.6) repulsions and many body attraction energies, based on a second moment tight binding model(second line in Eqn. 4.6). The functional form of this potential is given by

$$\begin{aligned} E_{tot} &= \sum_{i \neq j} A \exp\Big[-p\Big(\frac{r_{ij}}{r_0} - 1\Big)\Big] \\ &- \Big[\sum_{i \neq j} \xi^2 \exp\Big[-2q\Big(\frac{r_{ij}}{r_0} - 1\Big)\Big]\Big]^{1/2} \end{aligned} \tag{4.6}$$

where r_{ij} is the distance between atoms i and j. The parameters are $A = 0.13315$eV, $\xi = 1.6179$eV, $p = 10.50$, $q = 2.60$ and $r_0 = 2.553$Å. The motivation for using this model is described by Gupta[165] and has been shown to reproduce correct trends for thermal properties of transition metals[168–171].

This model has also been shown to reproduce the qualitative trends of the size dependence of the melting temperatures of finite Fe clusters [134, 172] while quantitative predictions require more complex models.

4.4.2 The substrate interaction

The PES used for the description of the interaction between Fe atoms and the substrate is given by a Morse potential, fit to *ab initio* data for interaction between iron and aluminium oxide (Al_2O_3). The details of the *ab initio* calculations and the fitting of the potential parameters are found in Ref. [70].

The potential energy of one atom is given by

$$E(r) = A_{sf} D\{\exp[-2\alpha(r - r_0)] - 2\exp[-\alpha(r - r_0)]\} \tag{4.7}$$

where r is the distance between the Fe atom and the substrate, D is the depth of the potential well, r_0 is the equilibrium bond distance and A_{sf} is a scalefactor introduced to study changes

in the adhesion strength. The fitted parameters are $D = 0.153$eV, $\alpha = 1.268$Å^{-1} and $r_0 = 2.219$Å. For $A_{sf} = 1$ these parameter reproduce the Fe-Al_2O_3 adhesion strength. The total potential energy is given by the sum of individual atomic contributions.

This PES only implicitly accounts for the lattice structure of the substrate, i.e. within the model the substrate is treated as continuous and perfectly smooth. This allowes for a very convenient way of describing the substrate interaction in an average manner if the direct interaction between individual atoms may not be of direct importance.

4.5 The tight binding approximation

The energy calculations in the TBMC method, used in Papers II and IV, were performed with a fourth moment tight binding approximation. This method was developed by Amara *et al.* [173] and has been used with success in previous studies of C and Ni systems[157, 174]. The method combines empirical observations with quantum mechanics by the introduction of a number of parameters describing the bonding and repulsion between atoms.

In principle, the parameters of this model are used to set up the Hamiltonian matrix which can then be diagonalized in order to obtain the energy eigenvalues. The matrix diagonalization is however a time consuming process and instead Amara *et al.* used the moment method to obtain an approximation of the local densities of states and potential energies. This leads to energies which are local in nature, referred to as the local energies, and the sum of all local energies constitute the total energy of the system.

In this section, a few of the basic concepts of TB will be outlined as well as the spirit of the moments method. This is done to illustrate the level of approximation and the meaning of the local energies which were used as a tool of analysis in Paper II. The basic theory of standard TB, i.e., not the moments method, is found in textbooks on electronic structure calculations e.g., Refs. [27, 175], and in the original publication by Slater and Koster[176]. Details about the general tight binding method, including the moments method, can be found in Refs. [177, 178] while the details of the method and parameters used are found in Ref. [173, 179].

4.5.1 The basics of tight binding

In the TB method, the wave functions are expressed as a linear combination of (orthonormal) atomic orbitals (LCAO). Every basis state can be written as $|i, \lambda\rangle$ where i is the atom on which the state is centred and λ is the electronic state, e.g., s, p_x, p_y, p_z.

In this basis, the Hamiltonian matrix of the system can be simplified to contain only one- and two-centre Hamiltonian matrix elements, i.e., all potentials which are not localised on same atoms as the states are neglected. This means that the effect from the surrounding crystal on the electronic structure is neglected and the matrix elements are written as $\langle j, \nu | V_k | i, \lambda \rangle = 0$ if $j \neq k$ and $i \neq k$. This approach is very convenient since these matrix elements can be evaluated from precalculated Slater-Koster[176] parameters. The advantage of this is that the integrals (matrix elements) need not be performed explicitly, which is also a time consuming process, but are approximated from the parameters which are weighted due to the distance and angles between the atoms. The Hamiltonian is constructed from the above mentioned matrix elements.

The total potential energy of the atomic system is given by a sum of a band term and a repulsive term as

$$E = E_{\text{band}} + E_{\text{repulsive}}. \tag{4.8}$$

where the band term is calculated as the sum, up to the Fermi energy, of eigenvalues of the Hamiltonian while the repulsive term is given by a phenomenological expression. The latter is fitted in order to reproduce some property of the system, e.g., bonding distances or bulk modulus and the total repulsive energy is typically obtained as sum of repulsive pair potentials, as discussed in association with the Lennard-Jones potential. The repulsive term will not be discussed further here but the forms of it is found in Ref. [179] for the C-C interaction and in Ref. [173] for the C-Ni and Ni-Ni interactions.

4.5.2 The local energies

If the total density of states of the groundstate of an atomic system is known, the total energy is found by an integration over all energies up to the Fermi energy, i.e, by the expression

$$E_{band} = \int_{-\infty}^{E_F} ED(E)dE \tag{4.9}$$

where E_F is the Fermi energy and $D(E)$ is the density of states (DOS) at energy E, given as

$$D(E) = \sum_{\text{all}E_k} \delta(E - E_k). \tag{4.10}$$

where E_k is the energy of the electronic state $|\Psi_k\rangle$. Now, the contribution of each basis state can be obtained by summing over all electronic states, i.e.

$$d_{i,\lambda}(E) = \sum_{\text{all}E_k} \left|\langle i, \lambda|\Psi_k\rangle\right|^2 \delta(E - E_k) \tag{4.11}$$

This is the local density of states (LDOS) corresponding to state $|i, \lambda\rangle$. The total density of states can now be written as the sum of all local density of states as

$$D(E) = \sum_{\text{all}i,\lambda} d_{i,\lambda}(E). \tag{4.12}$$

This means that if the local densities of states are known, so is the the total density of states and hence the total energy. In the TB scheme used, the local densities of states are calculated using the fourth moment TB approximation.

Instead of calculating the absolute band energy, it is more convenient to calculate the energy of the system compared to the energy of a system of individual atoms, i.e., the energy associated with the chemical bonds (in some sources, e.g., Ref. [178] called bond energy but following the outline of Amara[173] it will still be referred to as band energy). Hence it is appropriate to introduce the on site energies $\epsilon_{i,\lambda}$, in the model approximated as the atomic energy levels (ϵ_s, ϵ_p, ϵ_d) for the individual states.

Summing over all states connected to lattice site i, the LDOS for atom i is given by

$$d_i(E) = \sum_{\lambda} d_{i,\lambda}(E). \tag{4.13}$$

and the on site energy ϵ_i is given by filling the lowest energy atomic orbitals.

The band part of the local energy of atom i is now given by

$$E_{\text{i}} = \int_{-\infty}^{\epsilon_F^i} (E - \epsilon_i) d_i(E) \text{d}E \tag{4.14}$$

where ϵ_F^i is depend of the occupancy of local states of atom i, i.e. a fictitious local Fermi energy.

As discussed by Amara *et al.*[173] these local energy bands are filled with a number of electrons fulfilling local and global neutrality conditions. In principle this means that every atom has been given the number of electrons it would have as a neutral atom, i.e., any effects of charge transfer are neglected.

The sum of repulsive energy and band energy of one atom is referred to as local energy of this atom and the local energies are discussed and used in the analysis in Paper II.

4.5.3 The moments method

As discussed in Sutton[178], the moments can be associated with the LDOS as the second moment is a measure of the width, the third moment of the skewness and the fourth moment of the presence of modes in the LDOS. Although the first four moments do not provide full information of the LDOS, the approximate characteristics of the LDOS can be derived.

The moments can be calculated as

$$\mu_i^n = \sum_{a_1,a_2,\ldots,a_n} H_{a_1a_2}H_{a_2a_3}\ldots H_{a_na_1} \textbf{ where } a_1 \neq a_2 \neq \ldots a_n \tag{4.15}$$

where a correspond to a basis state $|a\rangle = |i,\lambda\rangle$ and $H_{a_1a_2} = \langle a_1|H|a_2\rangle$. This means that the moments can be approximated by "hopping" along all closed paths of atoms and states having nonzero Hamiltonian matrix elements. As an example for a C dimer, the second moment of state $|1,p_x\rangle$, i.e., the p_x orbital of atom 1, can be calculated by hopping from the p_x state of atom 1 to the s, p_x, p_y and p_z states of atom 2 and then back to p_x orbital of atom 1. This means that the second moment of this state is given as the sum of four contributions. This suggests that the calculation of the fourth moment of all states in a material containing hundreds of atoms is a rather complex task, especially at higher temperatures where all crystal structures have been distorted.

Some more details about the connetion between the first moments and the LDOS are found in Ref. [177].

4.6 Density functional theory

In this section the basics of density functional theory (DFT) are outlined. Since the majority of the DFT calculations in the appended papers were performed with the Vienna *ab initio* simulation package (VASP) the description will focus on DFT as implemented in VASP and the concepts needed to understand the parameters used.

Hopefully a statement like

> The DFT calculations were performed using the Vienna *ab initio* simulation package (VASP)[180] using a plane-wave basis set in combination with ultrasoft pseudo potentials (US-PP). All DFT results are from spin polarised calculations performed using the PW91[181] exchange-correlation functional and a plane wave energy cutoff of 400 eV. The simulation box was large enough to allow for Γ-point sampling of k-space.

will be comprehensible after reading this section despite the highly simplified theoretical description. Since the discussion is mainly based on textbook arguments, no specific referencing will be made unless something "nonstandard" is stated. The general DFT theory can be found in Refs. [27, 28, 175, 182] while details about implementation in VASP is found in [180, 183].

4.6.1 The basics of density functional theory

The density functional theory is based on two theorems by Hohenberg and Kohn, relating the ground state electron density to the ground state energy. These theorems can be expressed in different ways but the forms in Ref. [182] appears especially accessible for a first introduction. According to the theorems, the ground state energy of an atomic system is a functional of the ground state electron density. This functional is unique and does not depend on any external properties, e.g., positions of atomic nuclei, in an explicit way. Moreover, the existence of the functional is guaranteed and the ground state electron density (with corresponding energy) is given by the density that minimise the total energy.

Although this has reduced the many body problem of the Schrödinger equation to an optimisation problem in three dimensions it is not particularly helpful in practical calculations if neither the electron density nor the energy functional are known. An important step towards a practical implementation of density functional theory is to replace the set of interacting particles with a set of non-interacting particles and then add the effects due to direct interaction. Following this route the total energy of the atomic system can be written as

$$E = \sum_a \epsilon_a - \frac{1}{2}\int \mathrm{d}^3\mathbf{r}_1 \mathrm{d}^3\mathbf{r}_2 \frac{n(\mathbf{r}_1)n(\mathbf{r}_2)}{|\mathbf{r}_1 - \mathbf{r}_2|} + E_{xc}[n] - \int \mathrm{d}^3\mathbf{r} V_{xc}[n(\mathbf{r})]n(\mathbf{r}) \tag{4.16}$$

where ϵ_a are the eigenvalues of the Schrödinger-like Kohn-Sham equation

$$\Big[-\frac{1}{2}\nabla^2 - \sum_n \frac{Z_n}{|\mathbf{r} - \mathbf{R}_n|} + \int \mathrm{d}^3\mathbf{r}' \frac{n(\mathbf{r}')}{|\mathbf{r} - \mathbf{r}'|} + V_{xc}[n(\mathbf{r})] \Big] \psi_a = \epsilon_a \psi_a \tag{4.17}$$

The of electron interaction are added by $E_{xc}[n]$ which is an exchange correlation energy given as a functional of the density and $V_{xc}[n]$ is the exchange correlation potential, given as the functional derivative of $E_{xc}[n]$. The electron density can be obtained from the the Kohn-Sham wave functions, ψ_a, as

$$n(\mathbf{r}) = \sum_{a=1}^{N} |\psi_a|^2 \tag{4.18}$$

where the sum runs over all occupied wave functions and where N is the total number of electrons. Unlike for the Schrödinger equation, the individual wavefunctions and eigenvalues of the Kohn-Sham equation have no physical meaning but are used as a tool to construct the electron density.

For practical reasons in the future discussion, the potential terms of Eqn. 4.17, can be concatenated into an effective potential

$$V_{eff}(\mathbf{r}) = -\sum_n \frac{Z_n}{|\mathbf{r} - \mathbf{R}_n|} + \int \mathrm{d}^3\mathbf{r}' \frac{n(\mathbf{r}')}{|\mathbf{r} - \mathbf{r}'|} + V_{xc}[n(\mathbf{r})] \tag{4.19}$$

As seen from the equations, the density is needed in order to obtain the wave functions which in turn yield the electron density. Typically, this is done in a self consistency loop where

an initial guess of the charge density is used to calculate the wave functions which in turn will yield a new charge density. This procedure is repeated until a situation is reached where the old charge density yield wave functions that will generate the same charge density again, i.e., a self consistent electrical field (SCF). In a practical calculation, the SCF is obtained when some predetermined criterion is fulfilled. In the calculations presented in this thesis the self consistency criterion is usually set to when the energy difference between two consecutive steps in SCF-loop is less than $\Delta E = E_{l+1} - E_l < 10^{-5}$ eV.

4.6.2 Exchange correlation functionals

Although the existence if an exchange correlation functional is guaranteed by the Hohenberg-Kohn theorems there is a problem of knowing it and to this day, the exact form of this functional remains elusive. In the equations above, E_{xc} is needed to calculate the total energy and here some properties and approximations are discussed. The physical meaning of this functional is that it introduces all many-body effects, called correlation effects, which are not handled in an averaged way by the Hartree potential. It does also contain the exchange effects due to the Pauli principle, forcing electrons with same spin to keep a proper distance.

According to the theory, the functional is universal and must not depend on the external field. This means that the same functional should be valid for all electronic systems, i.e., it should reproduce the correct groundstate energy for a solid as well as for a highly charged ion despite the fundamental difference of the systems.

There are numerous approximate exchange correlation functionals (*xc*-functionals) that are frequently used in practical DFT calculations. These comes in two main kinds, commonly referred to as the local density approximation (LDA) and generalised gradient approximation(GGA).

Considering the LDA, the exchange and correlation depend only on the local electron density, i.e., the neither electron density at other parts of configuration space nor the spatial change in electron density are taken in to account. This could be considered as an homogeneous electron gas and where the exchange can be expressed analytically and the correlation contribution can be obtained from calculations, e.g., Quantum Monte Carlo (QMC). In Refs. [175, 182] some of the limitations of the LDAs are discussed. Typically the performance of the LDA functionals is limited for finite systems, e.g., metal clusters and CNTs. A problem that could be of relevance to the work discussed in this thesis is the known overestimation of the dissociation energies of molecules.

An technical improvement of the LDA is the generalised gradient approximation (GGA) which, in additions to the local electron density, includes gradients in the charge density. Two common GGA functionals are PW91[181] and PBE[184], both of which have been used in the work presented in the thesis. In Ref. [175], it is discussed that the bond lengths and bond angles are better reproduced by the GGA *xc*-functionals than for the LDA *xc*-functionals and this may be of great importance for the studies of CNTs and provides a rationale for the use of GGA functionals. A more extensive review of comparisons of the LDA and GGA functionals is found in Ref. [182].

In addition to the LDA and GGA classes of *xc*-functionals there exist other classes of functionals e.g., the meta-GGA and hybrid functionals. These include higher order derivatives of the density change and combines the exact exchange from a HF calculation with approximative correlation. For some systems, these are said to reproduce the same accuracy as methods taking correlation in in a low order perturbative way, e.g. Møller-Plesset perturbation theory,

coupled cluster or configuration interaction. The computational cost is however significantly lower[175].

The behaviour and accuracy of different functionals need to be evaluated for each situation and it may be deceptive to think that functionals of higher complexity are always superior to functionals of lower complexity, e.g., it may be so that LDA functionals are preferable to GGA functionals.

Another rationale for using the PW91 and PBE functionals for this work is that they have been used with success in previous studies[144].

4.6.3 Plane waves as basis states

The possibility to express the wave functions as a linear combination of atomic orbitals was disscussed in section 4.3 and used in the TB method. Another common type of basis states are plane waves (PWs) which are used in the DFT program VASP. Some details of this kind of basis will be outlined since these details are necessary to understand the computational parameters.

For periodic solids, Bloch's theorem states that the eigen functions for the Kohn-Sham equation can be written as

$$\psi(\mathbf{r}) = e^{i\mathbf{kr}} u_{\mathbf{k}}(\mathbf{r}) \tag{4.20}$$

where $\mathbf{k}$ is a point in the Brillouin zone, $u_{\mathbf{k}}(\mathbf{r})$ is a function which has the same periodicity as the cell and $e^{i\mathbf{kr}}$ is a plane wave. The periodicity of u implies that

$$u_{\mathbf{k}}(\mathbf{r}) = u_{\mathbf{k}}(\mathbf{r} + \mathbf{a}) \tag{4.21}$$

for any $\mathbf{a}$ being a translation to the same position in another cell, i.e. a lattice vector.

Now, any periodic function can be written as a Fourier transform

$$u_{\mathbf{k}}(\mathbf{r}) = \int \mathrm{d}\mathbf{G} u_{\mathbf{k}}(\mathbf{G}) e^{i\mathbf{Gr}} \tag{4.22}$$

and imposing the condition in Eqn. 4.21 gives that

$$e^{i\mathbf{Ga}} = 1 \tag{4.23}$$

for any lattice translation $\mathbf{a}$. This means that the allowed reciprocal vectors, $\mathbf{G}$, are precisely restricted to the reciprocal lattice vectors and the wave function can now be written as

$$\psi_{\mathbf{k}}(\mathbf{r}) = \frac{e^{i\mathbf{kr}}}{\sqrt{\Omega}} \sum_{\mathbf{G}} C_{\mathbf{k}}(\mathbf{G}) e^{i\mathbf{Gr}} \tag{4.24}$$

where Ω is the volume of the primitive cell and $C_{\mathbf{k}}(\mathbf{G})$ are the Fourier coefficients corresponding to the allowed reciprocal vectors $\mathbf{G}$. Considering this as a basis consisting of plane waves (PWs), the basis functions are given by

$$\xi_{\mathbf{kG}}(\mathbf{r}) = \frac{1}{\sqrt{\Omega}} e^{i(\mathbf{G}+\mathbf{k})\mathbf{r}} \tag{4.25}$$

when including the phase factor $\mathbf{k}$ in the basis. With these basis functions, the Hamiltonian matrix elements can be given by

$$H_{\mathbf{GG}'} = \langle \xi_{\mathbf{kG}} | H | \xi_{\mathbf{kG}'} \rangle \tag{4.26}$$

In reciprocal space the Kohn-Sham equation can be written as

$$\sum_{\mathbf{G}'} H_{\mathbf{G}\mathbf{G}'} C_{\mathbf{k}}(\mathbf{G}') = \epsilon_{\mathbf{k}} C_{\mathbf{k}}(\mathbf{G}) \tag{4.27}$$

where

$$H_{\mathbf{G}\mathbf{G}'} = \frac{1}{2}|\mathbf{G}+\mathbf{k}|^2 \delta_{\mathbf{G}\mathbf{G}'} + V_{eff}(\mathbf{G}-\mathbf{G}') \tag{4.28}$$

This exercise has led to two important concepts necessary to understand the settings for VASP. First, the PW basis is assumed to include all reciprocal lattice vectors $\mathbf{G}$, meaning that the basis is a complete (infinite) basis set in reciprocal space. This basis needs to be truncated in order to be practical for computations. It can be noted that $|\mathbf{G}+\mathbf{k}|^2$ corresponds to the kinetic energy of the plane waves. For the groundstate of an atomic system, there must exist a maximum energy of the electronic system, and it should be a good approximation to restrict the basis to have only have only PWs corresponding to an energy less than E_{cut}, i.e.,

$$|\mathbf{G}+\mathbf{k}|^2 < E_{cut}. \tag{4.29}$$

In the calculations presented in this thesis the PW energy cutoff is typically set to $E_{cut} = 400$ eV.

The second important concept introduced by Eqn. 4.28 is that $\mathbf{k}$ may take any value, as long as it lies within the first Brillouin zone. This means that for every value of $\mathbf{k}$, there is a separate KS equation with separate eigenvectors and eigenvalues. To calculate the total energy it is necessary to consider all possible $\mathbf{k}$-points, i.e. to integrate over all $\mathbf{k}$-points in the Brillouin zone. The calculation of the energy eigenvalues in certain directions in the Brillouin zone gives the energy bands in that direction*.

Since the length of the unit vectors of the Brillouin zone are inversely proportional to the unit vectors of the super cell, it is clear that if the real space super cell is large ($\mathbf{a_i} \to \infty$) the volume of the Brillouin zone becomes small. In the extreme case is when the supercell is infinite in size and the reciprocal cell is infinitesimal, only one $\mathbf{k}$-point can be sampled. For large cells this means that although there are many $\mathbf{k}$-points, it is only necessary to sample one to obtain the total energy. Typically, this point is chosen at $\mathbf{k} = 0$ which is called the Γ-point. In the calculations presented in this thesis, having 55 Ni atoms and 80 C atom were placed in a simulation box with side lengths of at least 15 Å which allowed for Γ-point sampling of $\mathbf{k}$-space. This box size is also large enough to separate each system a sufficient vacuum not to interact with its own periodic replica (the periodic replicas will be discussed further in association with the boundary conditions in section 5.4).

When performing a DFT calculation with PWs as the basis set it may also be interesting to note that, for the largest G corresponding to the PW energy cutoff E_{cut}, the number of PWs along every lattice vector are given by

$$n_i = \frac{G_{cut}}{|\mathbf{b}_i|} = \frac{G_{cut}|\mathbf{a}_i|}{2\pi} \tag{4.30}$$

This shows that the size of the basis set increases with increasing box size eventhough the PW energy cutoff is held constant. This means that, unlike for LCAO-basis sets, there is a computational cost associated with increasing box sizes and hence, the box must only be

*This is true for the Schrödinger equation but not for the KS equation.

large enough but preferably not larger. This is an effect of the fact that the PWs offers the possibility to represent electrons thoughout the super cell. If the vacuum region of the super cell is large, this means that a considerable computational effort may be needed offer the possibility to represent electrons where there are no electrons.

An advantage of the PW basis set compared to a LCAO basis is that the basis sets are independent of the positions of the atoms as well as the number of atoms. In the work presented in this thesis, this is important since many adhesion energies are calculated. If that were to be done within an LCAO approach, one would have to consider the possible basis set superposition errors (BSSEs), which is not needed here.

4.6.4 Pseudopotentials

Since the PW cutoff is associated with the Fourier expansion of real space, there is a correspondence between the PW energy cutoff and the possible resolution of the wave functions in real space. The resolution is given by

$$\Delta x G_{cut} = 2\pi \tag{4.31}$$

meaning that the larger the PW energy cut off is, the better the resolution is. If it is desirable to have a high resolution of the wave functions, e.g. to resolve the rapid spatial oscillations close to the atomic nuclei, it is necessary to increase the PW energy cutoff with an increased computational cost as the consequence. Also the Coulomb potentials from the atomic nuclei needs to be resolved properly when solving the KS equation.

One widely used method to avoid these unreasonably high PW energy cutoffs is the introduction of a pseudo potential. The philosophy of pseudo potentials is based on the idea that that the core electrons, which are tightly bound to the nuclei, do not contribute significantly to the chemical bonding between atoms. This means that the potential from these electrons, together with the potential from the nuclei, can be concatenated to form an effective potential, called a pseudo potential. After the introduction of the pseudo potential the valence electrons, which are explicitly treated in the PW basis, will not experience any rapid potential changes in space but will instead experience the pseudo potential.

To reduce the number of PWs needed to describe the atomic system, it is desirable that the PP is a slowly varying function, called a soft PP. One common PP construction scheme that fulfil this requirement, along with other requirements like norm conservation, is called the ultra soft pseudo potentials (US-PPs). The US-PPs are considered the best choice for PW calculations[175] and were used in the VASP calculations presented in this thesis.

The US-PPs must be constructed from an electronic configuration, e.g. an atom. For this system, it is necessary to choose which electrons that are to be included in the US-PP and which electrons that are to be treated as the valence electrons, i.e., treated explicitly in the calculations. The performance of a US-PP may depend on the situation for which it was constructed, e.g. a PP constructed for an atom may not perform as well for a solid and *vice versa.*. This means that the transferability of the PP may need to be considered. To VASP a few different PPs, with slightly different performance, are available for some elements and for the calculations presented in the thesis, the suggested PPs were used according to the instructions. Also, the construction of the US-PPs will affect the hardness of the US-PP, i.e., information about the PP is needed to determine the PW energy cutoff needed for the calculation. For VASP, this means that one should not use a lower energy cutoff than the highest recommended energy (if several atomic species are present). For C and Ni systems,

this minimum PW energy should be approximately 290 eV although a cutoff of 400 eV has been used for most calculations presented in the thesis. The somewhat obscure PW energy cutoff of 289.15eV in Papers II and IV was however motivated by recommendation in the US-PP.

When performing DFT calculations using US-PPs it may also be important to note that the *xc*-functional is used during the construction of the US-PPs and that the same *xc*-functional must be used for subsequent calculations, i.e., every *xc*-functional require a special US-PP. For VASP, US-PPs are available for two *xc*-functionals, one LDA and the PW91 GGA functional. This constitutes a practical rationale for the choice of *xc*-functional.

A problem with US-PPs concerns magnetic systems[182]. This means that it is reasonable to avoid magnetic systems and provides a practical rationale for the use of Ni as compared to e.g. Fe, in the calculations presented in the thesis.

4.6.5 Tests of the VASP parameters

To investigate which parameters, e.g. PW energy cutoff, box-size and k-point sampling to be used in the calculations, a few tests were performed for the systems under study. In Refs. [54, 144, 185] systems with 55 Ni atoms and short CNT stubs were studied by Γ-point sampling of k-space, PW energy cutoffs less than or equal to 400 eV and in box sizes $15 \times 15 \times 30$ Å^3. As the calculations with these parameters were successful, the tests presented were initiated with slight alterations of the abovementioned parameters.

The tests were performed for two different systems where the first system had 60 Ni atoms and the second had 60 Ni, 48 C atoms and 6 H atom. These systems were among the largest systems used in the studies presented in the thesis. The tests were performed with VASP and the energies presented are for atomic configurations that have been optimised with the conjugate gradient algorithm. All calculations were performed by Γ-point sampling of k-space and with the PW91 *xc*-functional. The calculated energies are given as eV per atom.

The results presented in Figs. 4.1 and 4.2 show that a box size of $15 \times 15 \times 30$ Å^3 and a PW energy cutoff of 400 eV should be enough to converge the results to approximately 1 meV per atom. This should be sufficiently accurate for the calculations presented later in the thesis as the conclusions presented are based on comparisons of significantly larger energy differences.

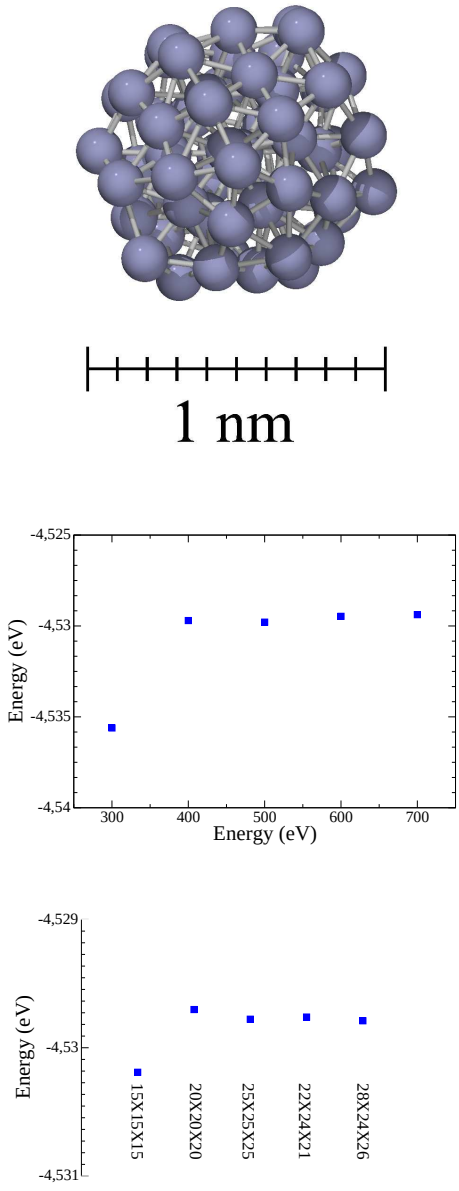

Figure 4.1: The diameter of an optimised Ni_{60} cluster (top panel) is approximately 1 nm. The energy per atom of an optimised atomic structure has calculated for different PW energy cutoffs (middle panel) and box sizes and geometries (bottom panel). I t is clear that a box size $15 \times 15 \times 15$ Å^3 and an energy cutoff of 400 eV will relax the structure within 1 meV per atom. When evaluating the the dependency of the PW energy cutoff the box size was set to $20 \times 20 \times 20$ Å^3 while the energy cutoff was 400 eV when evaluating the effect of the box size.

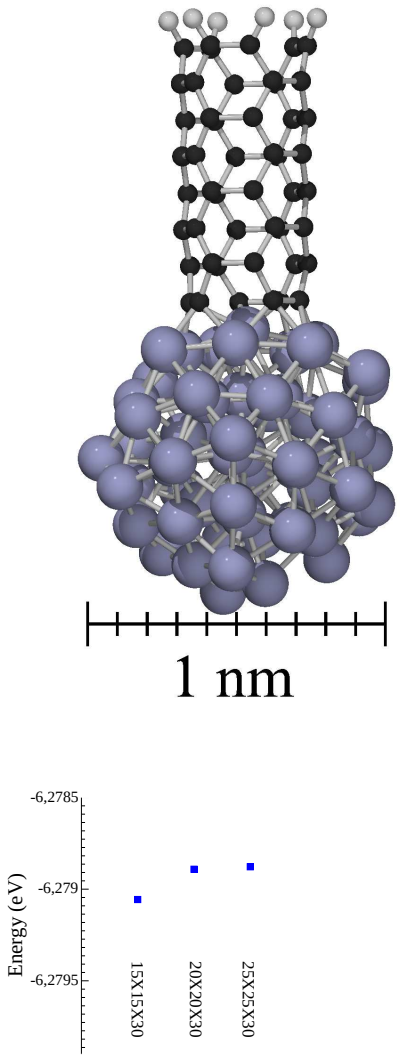

Figure 4.2: The typical width of a system with CNT, with 4 carbon rings, attached to a Ni_{60} cluster is approximately 1 nm while the typical height of the system is approximately 2 nm. This is seen in the top panel while the energies per atom are given for different box sizes and geometries in the bottom panel. It is clear that a box size $15 \times 15 \times 30$ Å^3 and is sufficient to converge the total energy within 1 meV per atom.

CHAPTER 5

Relaxations, Molecular Dynamics and Monte-Carlo

The equations governing time the evolution and equilibrium properties of an atomic system are, at least in principle, known to a sufficiently accurate level. Similar to the Schrödinger equation, these equations can be written on a few lines on a paper but exact solutions can found only for very simple systems. To extract useful information from these equations, computational techniques can be applied to make numerical approximations. These computational procedures are rarely straight forward solutions of the equations but are rather an exploitation of certain properties of the equations. This is comparable to the case of the Schrödinger equation for which three different routes were discussed. Here, two completely different approaches for finite temperature simulations, called molecular dynamics (MD) and Monte-Carlo (MC) simulations, will be presented along with a general discussion about relaxations and boundary conditions. The MD and MC simulations used for the work presented in this thesis were based on standard implementation if these techniques and good presentations can be found in Refs. [164, 186–190]. Thanks to the good descriptions on those books, there will be no explicit referencing of material that could be obtained form any of the books but only to statements that may be slightly nonstandard.

5.1 Classical molecular dynamics

In the description of MD simulations the atoms are considered to be classical particles which can be described the classical equations of motion. The forces acting on the atoms are needed to perform the time evolution and these forces are assumed to be available from one the the calculations described in section 4.4.

MD do not provide a general solution to the equations of motion but rather a solution that is an approximation valid under a very short time, $\mathrm{d}t$, and the sequence of such solutions constitute the long time solution. Ideally, for an isolated system every time step should be time reversible and the long time evolution should conserve the total energy of the system.

5.1.1 The time integration algorithm

Ideally, a molecular dynamics simulation should be identical to the actual evolution of the atomic system.This is almost never (if ever) the case due to approximations made during simulation. One approximation lies in the fact that the Hamiltonian available for computation is very simplified compared to the "real" system Hamiltonian, i.e., a physical limitation rather than a computational. A second approximation is the discretization of the time integration of the equations of motion. This means that even if the true Hamiltonian was available the simulated system trajectory is only an approximation of the true trajectory. This effect could be decreased by decreasing the time step which in the limit $\mathrm{d}t \rightarrow 0$ would give the correct time evolution. From a computational point of view this is highly unpractical since a desirable property of the time integration algorithm is that it is computationally inexpensive. In practice most of the computational time is spent on the force calculations implying that the time integration should use a minimum number of force calculations, i.e. the algorithm should allow for large time steps. In addition, it is of physical importance that the algorithm is time reversible and that it conserves the total energy of the simulated system. A successful time integration algorithm should take these, sometimes contradicting, properties into account.

It is important to note that a consequence of the discrete time integration is that the simulated particle trajectory will deviate from the true trajectory that would be obtained by exact time integration. The consequence of this is that no conclusions should be drawn from one single trajectory but instead from ensemble averages of the system and the time evolution of several different trajectories with independent starting conditions.

One widely used time integration algorithm was suggested by Verlet and can be implemented as

$$\mathbf{r}(t+\delta t) = 2\mathbf{r}(t) - \mathbf{r}(t-\delta t) + \mathbf{a}(t)\delta t^2. \tag{5.1}$$

Even though the velocities are not directly needed in the implementation of the algorithm, they can be useful for calculating average properties such as the kinetic energy and temperature. The velocities can be calculated as

$$\mathbf{v}(t) = \frac{\mathbf{r}(t+\delta t) - \mathbf{r}(t-\delta t)}{2\delta t}. \tag{5.2}$$

This algorithm is symmetric in time and the energy conservation is good even for relatively long time steps.

One disadvantage with this algorithm is that the velocities are not really used in the the time integration. This may mean a problem since scaling of the velocities can be used as a method of controlling the temperature during simulation, as will be discussed in section 5.1.3. The velocities can be introduced into the algorithm by a modified form of the Verlet algorithm, called the Verlet leap-frog algorithm. This is implemented as

$$\mathbf{r}(t+\delta t) = \mathbf{r}(t) + \delta t\mathbf{v}(t+\frac{\delta t}{2}) \tag{5.3}$$

$$\mathbf{v}(t+\frac{\delta t}{2}) = \mathbf{v}(t-\frac{\delta t}{2}) + \delta t\mathbf{a}(t) \tag{5.4}$$

As seen in the equation, the calculated positions and velocities are shifted by one half time step relative to each other. In order to calculate the total energy at time t, the velocities at this time need to be calculated as the average

$$\mathbf{v}(t) = \frac{\mathbf{v}(t+\frac{\delta t}{2}) + \mathbf{v}(t-\frac{\delta t}{2})}{2}. \tag{5.5}$$

The Verlet leap-frog algorithm was used for the time integration in the molecular dynamics simulations presented in Paper I.

In the book by Sadus[188] there is a discussion about the difference in performance of the different time integration algorithms. It is mentioned that the trajectories obtained from different forms of Verlet algorithms are likely to be equivalent. It is also mentioned that the Verlet class of integrators are likely to be preferred to other algorithms, e.g. the Gear class, since the accuracy of the integration is less sensitive to the length of timestep. The Verlet leap-frog should hence be a satisfactory choice of integrator.

5.1.2 Temperature measurements

To measure a macroscopic observable from a MD simulation, it is necessary to express the observable in the properties known within the simulation, i.e. atomic positions, velocities and energy.

For many simulations the ability to measure and control the temperature is of great importance. . The temperature of an unconstrained atomic system relates to the average kinetic energy as

$$2\langle E_{kin}\rangle = 3Nk_BT \tag{5.6}$$

where k_B is Boltzmann's constant, N is the total number particles and T is the temperature. The term $3N$ originates from the total number of degrees of freedom of the system and must be reduced if constraints are introduced. This relation can be used to determine the instantaneous temperature at time t as

$$T(t) = \frac{2}{3Nk_B}\sum_i \frac{m\mathbf{v}_i^2(t)}{2} \tag{5.7}$$

where the sum of i runs over all particle velocities. By calculating the kinetic energies throughout the simulation, the temperature can be calculated as the average of the instantaneous temperatures.

5.1.3 Temperature control - the Berendsen thermostat

The knowledge of the instantaneous temperature is also necessary when the temperature is to be controlled, e.g., by the Berendsen thermostat[191]. Temperature control by this thermostat is obtained by the application of a small perturbation to the velocities. The perturbation provide either an increase or decrease of the kinetic energy in order increase or decrease the temperature of the system. This perturbation is small so that the desired temperature is obtained first after large number of MD steps. Practically this is implemented by a scaling of the updated velocities at each timestep by a factor

$$\lambda = \Big[1 + \frac{\delta t}{\tau}\Big(\frac{T_0}{T} - 1\Big)\Big]^{1/2} \tag{5.8}$$

where T is the instantaneous temperature at this timestep, T_0 is the desired temperature and τ is the decay time for the temperature to reach T_0. Setting $\tau = \delta t$ means that temperature is scaled towards the desired temperature in only one time step, i.e. a rather large perturbation.

There are a few different thermostats available and results from comparisons between different thermostats are discussed in Refs. [187, 189]. Although the Berendsen thermostat may not be the best choice for all types of simulations the variations are small and it has the advantage of being very easy to implement.

5.1.4 The Lindemann index

The melting temperature of an atomic system can be determined by the monitoring of several properties, such as the caloric curves, the atomic mean square displacements and bond length fluctuations.

The latter can be analysed via the Lindemann index given by

$$\begin{aligned} \delta_i &= \frac{1}{N-1}\sum_{j\neq i}\frac{\sqrt{\langle r_{ij}^2\rangle - \langle r_{ij}\rangle^2}}{\langle r_{ij}\rangle} \\ \delta &= \frac{1}{N}\sum_i \delta_i \end{aligned} \tag{5.9}$$

where N is the total number of atoms, r_{ij} is the distance between atoms i and j, δ_i is the local (atomic) Lindemann index of atom i and δ is the global Lindemann index of the system. While the global Lindemann index gives a measure of the clusters thermodynamic state the local Lindemann index of atom i gives a measure of the mobility of this particular atom. This local property can be used to analyse the state of a certain group of atoms, e.g. the surface atoms of a cluster. This is discussed in some detail and some examples are given in Paper I and the discussion thereof.

5.2 Monte Carlo

The simulations in Paper II and IV were performed using the Monte-Carlo simulation which along with MD is the most common method for atomistic simulations at finite temperature. While MD is restricted to simulations of atomic systems, MC rests upon a very general idea and can be used in many different fields. The common property of all MC algorithms is that they make extensive use of random numbers.

In this section, only the application of the Metropolis Monte Carlo algorithm to molecular systems will be addressed. The discussion will be further limited to systems in the canonical ensemble, i.e. systems for which the number of particles (N), temperature (T) and volume (V) are held constant. This is actually the same ensemble as discussed in association with the MD simulations above although that was not explicitly discussed. Since spirit the MC simulations may not be as transparent as the MD simulations, some important steps of the derivation of this algorithm will be sketched since this makes the procedure more comprehensible. The details of these derivations, as well as similar derivations for other ensembles, can be found in any simulation textbook, e.g., Refs. [186, 187]. As will be evident later, the MC simulation require no force calculation and may be more appropriate when only the total energy of the atomic system is available from the PES, e.g., the fourth moment TB approach described in section 4.4.

As a short description of the MC algorithm, the random numbers are used to produce a sequence of possible states of the system. In the discussion below a state formally refers to an atomic configuration in configuration space, i.e., an atomic configuration. This is followed by an evaluation of the probability of the state and the importance of the state is weighted by its probability, i.e., a probable state will have a have a large contribution to the measured property while an improbable state will have less impact.

5.2.1 Canonical ensemble Monte Carlo

The expectation value (ensemble average) of a property $A(\mathbf{r}^N, \mathbf{p}^N)$, depending on the positions and momenta of N particles, can be written as

$$\langle A(\mathbf{r}^N, \mathbf{p}^N)\rangle = \frac{1}{Q}\int\int d\mathbf{r}^N d\mathbf{p}^N A(\mathbf{r}^N, \mathbf{p}^N)\rho(\mathbf{r}^N, \mathbf{p}^N) \tag{5.10}$$

where $\mathbf{r}^N$ is the positions of all particles, $\mathbf{p}^N$ is the momenta of all particles, $\rho(\mathbf{r}^N, \mathbf{p}^N)$ is the distribution function in phase space and Q is the partition function.

If the property A is the Hamiltonian of the atomic system the terms containing the momentum can be solved analytically which means that the expectation value of the potential energy can be written as

$$\langle E\rangle = K\frac{\int_R d\mathbf{r}^N V(\mathbf{r}^N)\exp\left(\frac{-V(\mathbf{r}^N)}{k_B T}\right)}{\int_R d\mathbf{r}^N \exp\left(\frac{-V(\mathbf{r}^N)}{k_B T}\right)} \tag{5.11}$$

where the constant K contains the analytically derived ideal gas properties of the system and $V(\mathbf{r})$ is the potential energy term of the Hamiltonian.

This is an integration in $3N$ dimensions which, for large N, is not very feasible to ordinary integration techniques. For example, the smallest systems that were studied in Paper II contained 135 atoms in a box of size 15Å×15Å×30Å, corresponding to a configuration space in $3 \times 135 = 405$ dimensions. If this integration was to be performed on a grid with grid spacing 0.1Å (which is a rather sparse grid) it is necessary to allow every variable to take $150\times150\times300 = 6.75\times10^6$ different values for every fixed value of the other variables. In effect this means that $(6.75 \times 10^6)^{405}$ energy calculations are needed which would be completely unrealistic and motivates a search for other more efficient methods.

An alternative procedure for the integration may be to implement a simple MC algorithm, i.e., to construct a (large) number, N_{trial} of random configurations (representing the entire phase space) and evaluate the expectation value as

$$\langle E\rangle = K\frac{\sum_{i=1}^{N_{trial}} V(\mathbf{r}_i^N)\exp\left(\frac{-V(\mathbf{r}_i^N)}{k_B T}\right)}{\sum_{i=1}^{N_{trial}} \exp\left(\frac{-V(\mathbf{r}_i^N)}{k_B T}\right)}. \tag{5.12}$$

In the limit $N_{trial} \to \infty$ this should sample the entire space and hence give a correct calculation of the expectation value. As is, this should not mean a great improvement over performing the integration on the abovementioned grid. This is partially due to the unfortunate fact that most configurations in configuration space have a high energy (due to atomic overlap) and hence a low probability. The consequence of this is that most of the simulation time would be spent on sampling configurations which do not contribute significantly to the expectation value. Another drawback of this waste of time would be that the calculated average property would be based on few samples, i.e., the statistics would be very poor.

5.2.2 Metropolis Monte Carlo algorithm

An improvement would be to construct only configurations which give significant contributions to the expectation value, i.e., obtaining a decrease in the waste of time and an increase in

the quality of the statistics. This is however difficult since it is not known *a priori* which configurations that give significant contributions. A solution to this problem is the Metropolis Monte Carlo algorithm.

The discrete normalised probability to find the system in state (configuration) i is given by

$$P(\mathbf{r}_i^N) = \frac{\exp\left(\frac{-H(\mathbf{r}_i^N)}{k_B T}\right)}{\sum_j \exp\left(\frac{-H(\mathbf{r}_j^N)}{k_B T}\right)} \tag{5.13}$$

For systems with many states, the transition probability $\pi(\mathbf{r}_i^N \rightarrow \mathbf{r}_j^N)$ can be introduced in order to represent the probability of a transition from state (configuration) i to state j.

In equilibrium the probability distribution is stable and does not change in time. This means that the probability of being in state i and leaving to some other state should be equal to the probability of not being in state i but end there after a transition. If this condition is not fulfilled the probability distribution would change and hence it can not be an equilibrium distribution. This can be expressed by the results of Eqn. 5.13 and the transition probability to all other states.

In the Metropolis MC algorithm this probability balance is resolved with the stronger, detailed balance condition imposing the equality of on each pair of states individually. This can be expressed as

$$P(\mathbf{r}_i^N)\pi(\mathbf{r}_i^N \rightarrow \mathbf{r}_j^N) = P(\mathbf{r}_j^N)\pi(\mathbf{r}_j^N \rightarrow \mathbf{r}_i^N) \tag{5.14}$$

stating that the probability of being in state i and leave to state j is equal to the probability of being in state j and leave to state i. If the creation of a new configurations is done in a symmetric way without preferences, i.e. it is equally probable to attempt a trial move from state i to j as a trial move from j to i, the transition probability is equal to the probability of suggesting the trial move, $\alpha(\mathbf{r}_i^N \rightarrow \mathbf{r}_j^N)$, times the probability of acceptance of the trial move, $\pi(\mathbf{r}_i^N \rightarrow \mathbf{r}_j^N) = acc(\mathbf{r}_i^N \rightarrow \mathbf{r}_j^N)\alpha(\mathbf{r}_i^N \rightarrow \mathbf{r}_j^N)$ This means that equation 5.14 can be rewritten as

$$P(\mathbf{r}_i^N)acc(\mathbf{r}_i^N \rightarrow \mathbf{r}_j^N) = P(\mathbf{r}_j^N)acc(\mathbf{r}_j^N \rightarrow \mathbf{r}_i^N) \tag{5.15}$$

which leads

$$\frac{acc(\mathbf{r}_i^N \rightarrow \mathbf{r}_j^N)}{acc(\mathbf{r}_j^N \rightarrow \mathbf{r}_i^N)} = \frac{P(\mathbf{r}_j^N)}{P(\mathbf{r}_i^N)} = \exp\Big(-\frac{E(\mathbf{r}_j^N) - E(\mathbf{r}_i^N)}{k_B T}\Big) \tag{5.16}$$

A common, but not the only, choice of acceptance probabilities that satisfy this condition is that

$$acc(\mathbf{r}_i^N \rightarrow \mathbf{r}_j^N) = \quad 1 \quad \text{if } P(\mathbf{r}_j^N) \geq P(\mathbf{r}_i^N) \tag{5.17}$$

$$acc(\mathbf{r}_i^N \rightarrow \mathbf{r}_j^N) = \quad P(\mathbf{r}_j^N)/P(\mathbf{r}_i^N) \quad \text{if } P(\mathbf{r}_j^N) < P(\mathbf{r}_i^N) \tag{5.18}$$

In the practical calculation, this means that a new configuration is accepted if the energy of the new configuration is lower than the energy of the old configuration. If the energy of the new configuration is higher than the old, it is accepted with a probability of $P(\mathbf{r}_j^N)/P(\mathbf{r}_i^N)$. In practice, this is achieved by comparing this ratio to a random number generated in the interval 0 to 1. If the random number is less than this ratio, the new configuration is accepted, othervise it is rejected.

The difference between the Monte Carlo described in association with Eqn. 5.12 and the Metropolis Monte Carlo is that for the first the configurations are created with equal

probability but their impact is weighted. For the latter, the creation of configurations is weighted but the impact of each configuration is equally important.

In principle, the Metropolis algorithm should sample the entire phase space, irrespectively of the starting configuration while this may not be achieved during a finite simulation time. To ensure that the result does not depend on the starting configuration, many simulations with different starting configurations should be performed. This means that similar to the previously discussed case of MD simulations no definite conclusions should be drawn from one single configurational plot or calculated energy. Instead, analysis of a number of configurational plots and energies can give an indication of the probability of these structures or energies.

5.3 Structure optimisations

For the DFT calculations, the computational cost is too high to allow for any converged dynamical simulations although a few shorter MD simulations were performed to capture temperature effects. Instead a few structure optimisations, or relaxations, were performed in order to find the local (or global) minimum energy geometry of a structure with certain properties. For the studies presented in the thesis, this is done in order to make comparisons between qualitatively different structures that are relevant for the study. As an example from Paper III, the two qualitatively different structures can have the same number of C and Ni atoms but either have 20 C atoms dissolved into the Ni cluster or as part of a CNT. The energy comparison between these structures can provide information about which of the structures that is the most stable and hence the most probable. This require that the input structures to the calculation are well prepared since the calculations are very sensitive to the spatial positions of the atoms and small (0.1 Å) changes in the atomic positions may mean large differences in the calculated energies. This means that the result of the calculation would be completely dependent on the input configuration with the consequence that no conclusions could be drawn. At least partially, this dependence can be reduced by a structure optimisation which aims at finding the nearest optimal configuration. In principle, this procedure does still require that the initial configuration is very similar to the situation of interest since the structure optimisations do not allow for large changes of the atomic structure. These small geometrical changes does also mean that most of the quality of the structure is still present after optimisations although minor qualitative changes may occur.

Formally, the finding of the optimal geometry of an atomic configuration means that the nearest stationary point of the PES is to be found. The relaxations associated with the DFT calculations presented in the thesis were performed with the conjugate gradient (CG) algorithm (except for the few GPAW calculations where the quasi-Newton algorithm was used). In principle this exploits the fact that a function changes the most along its gradient and that a minimum is likely be found in the direction along it's negative gradient. The minimisation is done iteratively where a step length is chosen then traced in the direction of the negative gradient. This procedure is then aborted when some criterion of convergence is fulfilled. Typically, the CG relaxations were aborted when the change in total energy change between subsequent relaxation steps was less then 10^{-4} eV. This was usually obtained within a few hundred relaxation steps although for some systems, e.g., the systems containing $Ni_{55}C_{20}$-clusters, the relaxations were particularly long, requiring up to 1000 relaxation steps.

The results obtained from a relaxation with the CG, or any other 0K optimisation algo-

rithm, are very sensitive to the starting configuration and step length. Hence, it is important not to draw definite conclusions from one single relaxation but instead from larger series of calculations pointing towards the same trends. In the calculations in papers II - V, this problem was addressed by different approaches. These included the relaxation of several different structures with the same qualitative properties, MD simulations of the starting structure before relaxation and simulated annealing with the TBMC method prior to relaxation. An optimisation recipe that appeared rather effective, but also very expensive, was to create a structure, relax it slightly with VASP or TBMC, perform MD simulation with VASP for a few ps and then relax properly, i.e., using VASP with high accuracy. This procedure was used for the Paper III but it was not possible to use it for the vast amount of configurations in Paper V. Despite the relaxations and careful sample preparation any conclusions based on energy differences of less than approximately 1 eV were avoided in the analysis of the results as energy differences of this order are typical for optimisations form different starting configurations.

5.4 Boundary conditions

When performing calculations on infinite systems, e.g., bulk metal or CNTs (which can be considered to be infinite in one direction), it is undesirable to have any surfaces against vacuum. This can be avoided by imposing periodic boundary conditions which in effect means that the calculations are performed for a simulation box of finite size which is part of an infinite system. The finite box is then replicated as periodic images throughout space. Hence, the central simulation box has no surfaces and the system under study can be considered as periodic and infinite in size. For example, an atom close to the top of the central simulation box will interact with atoms near the bottom of the periodic replica located above the central simulation box. For the case of attractive interaction between the atoms this may mean that one of the atoms leave the central box and enters the periodic replica which in effect mean that it will be inserted into the central simulation box on the opposite interface, i.e., at the bottom if it was leaving at the top.

All calculations presented in the thesis have been performed for finite systems and imposion of the periodic boundary conditions may appear redundant. Although this may be true, the PW-basis set introduce periodic boundary conditions to the DFT calculations whether is it desirable or not and hence it is necessary to consider this.

The PBCs mean an important advantage in the calculations of infinite systems but for finite systems they may also introduce difficulties in the calculations. For example, the atoms do not only interact with the atoms in the central simulation box but also with the atoms in the periodic images. In principle, this means that every atom has to interact with all atoms in infinitely many periodic images. Consequently, an atom will interact with infinitely many versions of it's own replica in the periodic images. This difficulty might be avoided by introducing what is known as the minimum image convention[187]. For an atom, indexed i, this is implemented after the following scheme. A new box is introduced, with centre in the position of atom i. This new box has the same size and geometry as the original simulation box. Now, atom i is only allowed to interact with atoms lying within the new box. Hence, this atom can interact with all other atoms, but only with one version of them, lying either in the simulation box or in a periodic image but not both. Especially, this atom is not allowed to interact with one of its own replicas. This requires that the interaction between atoms is short

ranged so that setting this cut-off distance does not constitute a too large approximation.

For finite systems, it is also necessary to isolate the atomic system with a sufficient vacuum distance to the periodic replicas, i.e., a system centred in the middle of the simulation box may not interact with any atoms in the periodic replicas. Under the assumption that the box size large enough to allow for Γ-point sampling, this means that calculations can be performed for several box sizes with results that converge for a certain box size.

For the results presented in the thesis, the periodic boundary conditions were imposed on the TBMC and VASP calculations while the MD simulations of Fe clusters were performed in an infinite simulation box. As the box size did not affect the time consumption of the TB calculations, the boxes sizes used were very large and far beyond the cut off of the TB model. For the DFT calculations, the box sizes were more crucial since the increase in box size lead to an increased size of the basis set and hence increased calculation time. The boxes should then be chosen such that the both the calculation time and accuracy were optimised. The tests presented in section 4.6.5 showed that the boxes used were sufficiently large to avoid this type of interaction as well, i.e., in addition to single k-point sampling.

CHAPTER 6

Summary of the appended papers

In this chapter a brief summary of the appended publications will be presented. Extensive information about computational parameters, structure preparations, computational results and analysis thereof is found in the publications while this section serve as an overview and complement. Some of the most interesting results will be highlighted and some additional information will be provided. This additional material may include results that were not included in the final publication but it may also be more detailed explanations of our ideas and arguments.

6.1 Paper I - Melting temperatures of supported clusters

As mentioned in section 3.1, the melting temperatures and behaviour of free metal clusters and metal clusters supported on flat substrates have been investigated in previous studies. It was concluded that than nano clusters have a significantly lower melting temperature than the bulk melting temperature and that clusters on substrates have higher melting temperatures than free clusters of the same size, although still lower than the bulk melting temperature. This odd melting behaviour of small clusters was investigated further for Fe clusters attached on substrates with different shape and adhesion strength. The studies were motivated by the fact that CNTs are often grown from catalyst particles that are mounted on substrates. The substrates are not likely to be perfectly flat but may instead contain pores, ridges, protrusions etc. which may affect the melting temperature and mechanism of the clusters. A few different substrate shapes, illustrated in Fig. 6.1, were included in the study.

All studies presented in this chapter were performed using MD simulations with empirical force fields discussed in sections 4.4.1 and 4.4.2. This method has been used in previous studies[66, 70] and a more extensive review of the this work is found in Ref. [192].

6.1.1 Results

The first study included in Paper I had the objective to understand how the cluster-substrate adhesion strength affect the melting temperature of the clusters. This was done for a Fe_{250}

cluster when the adhesion strength was varied from 0 (free cluster) to 5.5 times the fitted Fe-Al_2O_3 adhesion strength. The caloric curves for the different adhesion strengths are given in Fig. 6.2 and it is clear that the melting temperature increases with increased adhesion strength. This can be explained by the deformation of the cluster which is induced by the substrate and according to the discussion by Ding *et al.*[66], the supported cluster is better described by a cluster with a larger, effective, diameter and hence having higher melting temperature. The stronger the adhesion becomes, the larger the effective radius becomes with the effect that the melting temperature increases. The concept of the effective radius is illustrated in Fig. 6.3 where a cross section of a Fe_{250} cluster is seen for scalings of 1, 2, 3 and 4 times the fitted Fe-Al_2O_3 adhesion strength. The effective radius of the cluster is seen to increase from 10.7Å to approximately 14.6Å.

The first shaped surfaces studied were the deep cylindrical pores that are seen in panels (b) and (c) in Fig. 6.1. These pore shapes were chosen to study the melting behaviour when the clusters fit entirely within the pore. It was expected that the melting temperatures of the clusters in these pores would be higher than for clusters on the flat substrates since the number of atoms that are stabilised by the substrate is significantly higher than for the flat substrate. This showed not to be the case and instead, for the fitted Fe-Al_2O_3 adhesion, the melting temperature of the cluster in the pore was very similar to that of a cluster on a flat substrate. For a Fe_{250} cluster this is seen in Fig. 6.4 where the melting temperature is plotted against the Fe-substrate adhesion strength. When the adhesion is scaled towards stronger adhesions, the melting temperature of the cluster in the deep pore is seen to be significantly lower than for the cluster on the flat substrate. This can be explained by arguments similar to those used above to explain the increase in melting temperature of clusters on a flat surface with increased adhesion strength. When the clusters on the flat substrate becomes more flattened, i.e., experience a larger effective radius, with increasing adhesion strengths the the clusters in the deep pore can not smear over the surface in order to form a cluster with larger effective radius. Instead the radius is defined by the size of the pore which means that atoms close to the pore walls may be stabilised by the stronger adhesion while the atoms in the centre of the cluster are not affected by this and do not experience a reduced mobility with the result that the melting temperature is not that strongly affected by the adhesion strength.

The next substrate shape studied was the shallow, parabolic pore seen in Fig 6.1(d). In Fig. 6.5 the caloric curves for a Fe_{250} cluster which is either free, mounted on a flat substrate or mounted on the parabolic pore can be compared. It is clear that the melting temperature of a cluster on top of the shallow pore, is lower than the melting temperature of a cluster mounted on a perfectly flat substrate.

This unexpected behaviour could be understood by analysis of the atomic Lindemann indices which provide a measure of the mobility of atoms in particular regions of the cluster. The atomic Lindemann indices, plotted against z-position (i.e. height over the flat part of the substrate located in the xy-plane) are seen in left panel of Fig. 6.6 at a temperature just below the melting point of the cluster. At this temperature atoms below the flat part of surface, i.e. inside the pore, are more mobile than atoms on the top part of the cluster (z-position above ≈ 7.5Å). The right panel of Fig .6.6 show the atomic Lindemann indices plotted against the distance to centre of mass of the cluster. Here, atoms further away from the centre of mass of the cluster are more mobile than atoms in the bulk of the cluster. The conclusion drawn from these observations is that melting of clusters on shallow pores starts on the surface of the bottom part (half) of the cluster. This is illustrated in Fig. 6.7 where the Fe_{250} cluster on the pore is seen at temperatures that are just below (980 K) and just above (1000 K) the

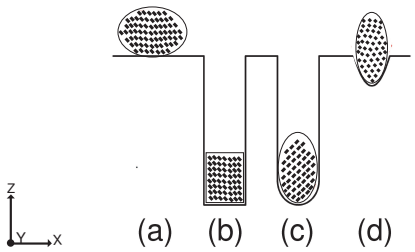

Figure 6.1: Four different substrate shapes included in the study in Paper I.

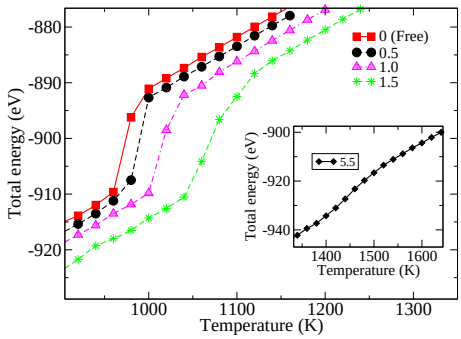

Figure 6.2: Caloric curves for a Fe_{250} cluster on a flat substrate. The caloric curves are given for different cluster-surface adhesion strengths given in the legend as scalings of the fitted Fe-Al_2O_3 adhesion strength. In this case a scale factor $A_{sf} = 0$ means no cluster-substrate adhesion, i.e. a free cluster. The inset shows the caloric curve for an very strong cluster-surface adhesion.

melting point. Atoms with an atomic Lindemann index $\delta_i > 0.1$ are bright while atoms with an atomic Lindemann index $\delta_i < 0.1$ are darker. At the lower temperature (left panel) the atoms with the higher Lindemann index are situated inside the pore and on on a ring, just above the pore. In Fig. 6.7 three regions with different curvature can be identified. Atoms in each of these regions experience a different effective radius, i.e., they should experience the melting behaviour of clusters of this size. Atoms in regions with high mobility (a) and (b) in Fig. 6.7 have a high curvature, i.e. a small effective radius while the region (c), having a lower atomic mobility, is associated with a lower curvature. This indicates that not only the cluster size is of importance for the melting temperature but also the clusters curvature.

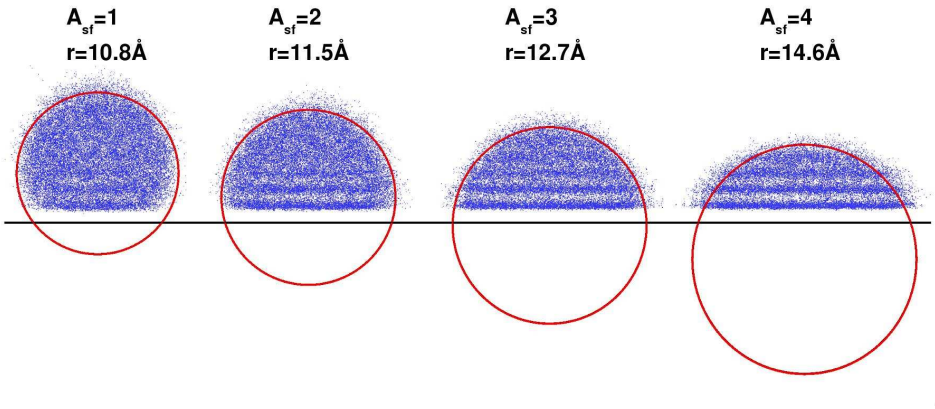

Figure 6.3: Cross sections of Fe_{250} clusters mounted on substrates with adhesion strengths $A_{sf} = 1$, 2, 3 and 4 times the fitted Fe-Al_2O_3 adhesion strength. The cross sections show atoms lying within a sheet of thickness 1 Å perpendicular to the substrate and have been sampled over 100 ps at 2000K. The effective radius, r, is seen to increase with increasing adhesion strength while the curvature of the cluster surface decrease. The increase in melting temperature with increasing adhesion strength is indicated by the presence of a crystal structure, seen by the horizontal fringes for the stronger adhesion strengths, despite the high temperature.

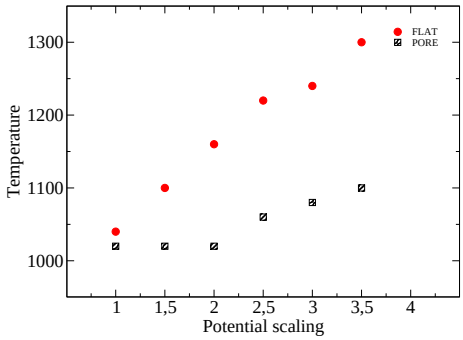

Figure 6.4: The melting temperatues for a Fe_{250} plotted against the scaling of the cluster-substrate adhesion strength, i.e. different values of A_{sf}. Curves are for a cluster on a flat substrate and a cluster in a deep cylindrical pore.

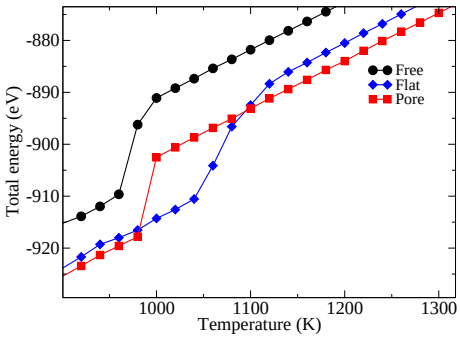

Figure 6.5: Caloric curves for a Fe_{250} cluster. Caloric curves are for a free cluster, a cluster mounted on a flat substrate and a cluster mounted on a parabolic pore.

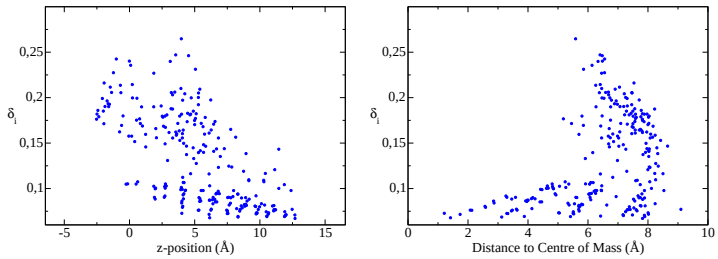

Figure 6.6: The atomic Lindemann indices for at Fe_{250} cluster mounted on a shallow, parabolic pore. Lindemann indices are plotted against height over the flat part of the substrate (left) and against the distance to centre of mass (right).

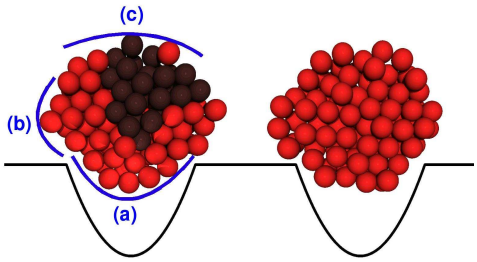

Figure 6.7: Typical atomic configurations below (left) and above (right) melting point of a Fe_{250} cluster mounted on a parabolic pore. Atoms with average atomic Lindemann index below 0.1 are dark red while atoms with average atomic Lindemann index above 0.1 are bright red. Three regions with different surface curvature have been indicated as (a), (b) and (c). The bright red atoms of regions (a) and (b) indicate that atoms are more mobile compared to the region (c) with lower curvature.

6.2 Paper II - CNTs on Ni clusters

The possibility to continue growth of existing CNTs[84] was mentioned in the introduction. The CNTs obtained after the continued growth have the same chirality distribution as the initial distribution although the 1:1 correspondence for each CNT has not been established, i.e., it is not known if each CNT will continue growth with the same chirality or if it is only the overall distribution that remains the same. It was also seen that the initial (seed) CNTs had to be handled with care for the continued growth to be successful. This was attributed to the necessity of having a nice, uncompromised CNT end upon starting the continued growth. A crucial step here may be the docking procedure where new catalyst particles are attached to the open CNT ends.

Detailed understanding of the continued growth process may offer a way of controlled CNT growth, e.g., by the continued growth of certain chiralities while other other chiralities are not continued. The docking of metallic nanoparticles onto existing CNT ends may also be of importance for the construction of CNT based nanoelectronics where the metal is used as a contact material between CNTs and another material.

This constitutes the background for the study presented in Paper II where the docking of Ni nano particles to open CNT ends was investigated in a combined DFT and TBMC study. Geometry optimisations at 0 K were performed using VASP while the TBMC method offered the opportunity to study the same systems at finite temperatures, typically 1000K. The docking of Ni nano clusters to SWNT ends were studied for three different situations. These are referred to as gentle docking, forced docking and evaporation. For the gentle docking the CNTs were positioned above the cluster surface while for the forced docking the CNTs were inserted into the clusters. For the evaporation the Ni atoms were randomly distributed on the SWNT surface.

6.2.1 Results

For the gentle docking the SWNTs were seen to attach to the cluster surfaces, i.e., the SWNTs had no roots below the cluster surface. Moreover, the clusters were seen to adapt to the CNT shape and not *vice versa* meaning that the geometry of the SWNT ends were not significantly altered when introducing a cluster. These results are illustrated in Fig. 6.8 where the initial (left) and typical final (right) configurations obtained after TBMC simulation at 1000 K are shown for a Ni_{55} cluster that had been gently docked to $(5,5)$, $(6,5)$, $(9,2)$ and $(10,0)$ SWNT ends. Another observation was that Ni atoms, that were initially located inside the SWNT, retract from the interior of the SWNT. For example, the $(10,0)$ SWNT (bottom of Fig. 6.8) initially has 4 Ni atoms above the lowest C ring and after the simulation, all of these atoms are located below the lowest C ring. This is illustrated in Fig. 6.9 where the average height above the lowest C ring of these atoms is plotted against the number of attempted MC displacements. On average, the atoms move from positions ≈ 0.5 Å above the lowest C ring to a position ≈ 0.5 Å below the ring. For all chiralities included in the study, the SWNT ends were seen to keep both the chirality and shape, indicating that gentle docking of Ni clusters onto CNT ends may fulfil the requirements for continued growth, i.e. preserving the CNT lips. The trends reported here are based on observations of TBMC simulations but DFT relaxations show the same trends, as presented in Paper II.

For clusters docked with the forced docking procedure some C atoms, initially positioned below the cluster surface, were seen to dissolve into the cluster. This is illustrated in Fig.

6.10, showing a Ni_{55} cluster attached to $(5,5)$, $(6,5)$, $(9,2)$ and $(10,0)$ SWNT ends by the forced docking procedure. In the figure, the dissolved C atoms have been indicated as bright blue atoms. The dissolution makes the SWNT shorter and similarly to the gentle docking, the SWNT lips attach to the (carbide) cluster surface. The final configurations with a cluster on the SWNT end were also seen to be stable, i.e., once the cluster was attached to the SWNT end it remained there and no further carbon dissolved into the cluster. The dissolution of C atoms was not seen to introduce any new defects on the CNT end other than removal of hexagons, i.e., the CNT chirality was clearly visible even after forced docking. Under the condition that the dissolved C atoms do not significantly alter the growth properties the forced docking would also allow for continued growth of CNTs. The possible effect of the dissolved C atoms will not be discussed further in this section but will be addressed again in Paper III.

For the case of evaporation or extremely forced docking, seen in top left panel of Fig. 6.11 the Ni atoms initially positioned on the outside of a $(9,0)$ SWNT were seen to rapidly retract to the SWNT end. Also Ni atoms positioned inside the SWNT retract to the end although this is slower process as the atoms already at the end serve as a road block. The simulations of these systems were performed at temperatures between 1000K and 2000K where the difference

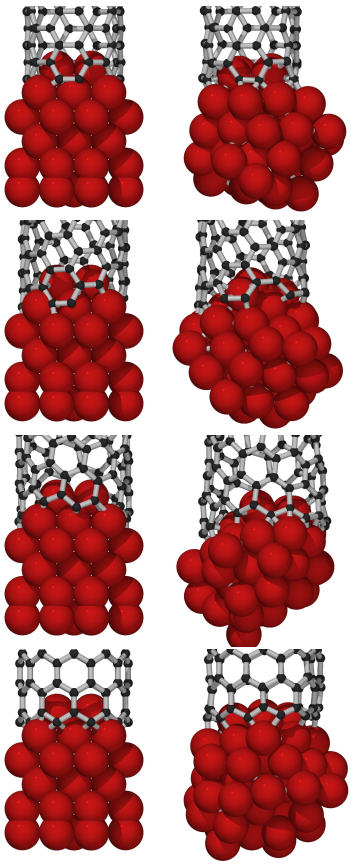

Figure 6.8: Initial (left) and final (right) configurations for Ni_{55}-SWNT systems. The CNT chiralities from top to bottom are (5,5), (6,5), (9,2) and (10,0) nanotubes. The initial Ni_{55} clusters, cut from the bulk *fcc* structure, were positioned slightly inside the SWNTs. The final structures were obtained from TB MC simulations at 1000 K.

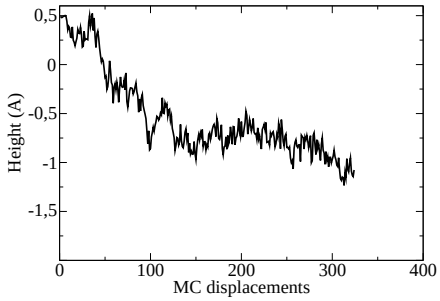

Figure 6.9: Relative height, compared to the lowest C ring of a $(10, 0)$ SWNT, of the 4 Ni atoms initially ≈ 0.5 Å above the lowest C ring. The x-axis is the number of MC displacements, $N \times 200$ where N is the number of atoms allowed to move, i.e., 300 on the x-axis corresponds to an average of 60000 MC displacements per atom.

between the low and high temperature was that the equilibration at 2000K was significantly faster than at 1000K. At the higher temperature, there was also a small ability for small nickel clusters to leave the main structure and disappear as an independent unit into the simulation box. The retraction to the end was seen irrespectively of whether the CNT structure was held rigid or not but the process was significantly faster for the rigid structure and hence, the CNT was held rigid for subsequent calculations. However, as the situation above resemble forced docking a few C atoms were dissolved into the metal when allowing the CNT structure to move.

TBMC simulations in the temperature span of 1000K to 2000K were also performed for a more sparse Ni distribution on the a $(9, 0)$ CNT end where the initial(left) and a typical final (right) configuration are shown in Fig. 6.12. During the simulation, the Ni atoms formed droplets on the SWNT surface which, for sufficiently long simulation times, combined to form a cluster at the SWNT end.

Simulations of both dense and sparse Ni distributions showed that clustering on the nanotube end was energetically favourable compared to clustering elsewhere or Ni wetting of the CNT. The total energy histograms of the initial and final configurations for these systems are shown as the bottom panels of Figs. 6.11 and 6.12 where the energy gained by the formation of the larger clusters is in the order of 20 eV for both systems. This indicates that that evaporation of Ni atoms over the SWNT surface can be effectively used in order to create a Ni cluster situated at the SWNT end. However, the process may be sensitive to the metal concentration and for high metal concentration some C may dissolve into the cluster particle.

The retraction of Ni atoms from the CNT end can be analysed by a closer inspection of the local energies available within the TB model. Here, the local energies are presented as histograms sampled during the first (for initial distributions) and last (for final distributions) segments of the simulations. During the sampling the atomic configurations were not allowed to change significantly before sampling, i.e., the histograms should represent the true initial and final situations respectively.

The Ni atoms were categorised into bulk, surface and interface atoms while C atoms were categorised into bulk (CNT) and interface*. Interface Ni atoms are defined as Ni atoms with,

*The categorisation in Papers II and V are not entirely consistent although they should be qualitatively

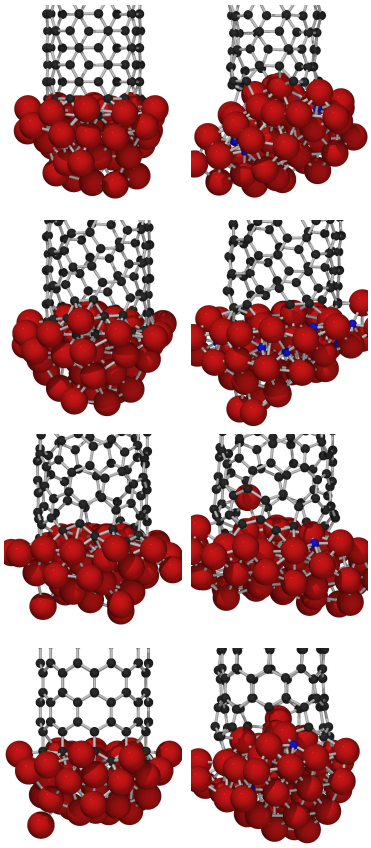

Figure 6.10: Initial (left panels) and final (right panels) configurations of Ni_{55}-SWNT systems, for (5,5), (6,5), (9,2) and (10,0) nanotubes. The Ni_{55} was created by random positioning of Ni atoms around the SWNT end, representing forced docking. Carbon atoms dissolved in the cluster are bright blue. Only the carbon atoms near the SWNT-metal interface are shown for the sake of clarity.

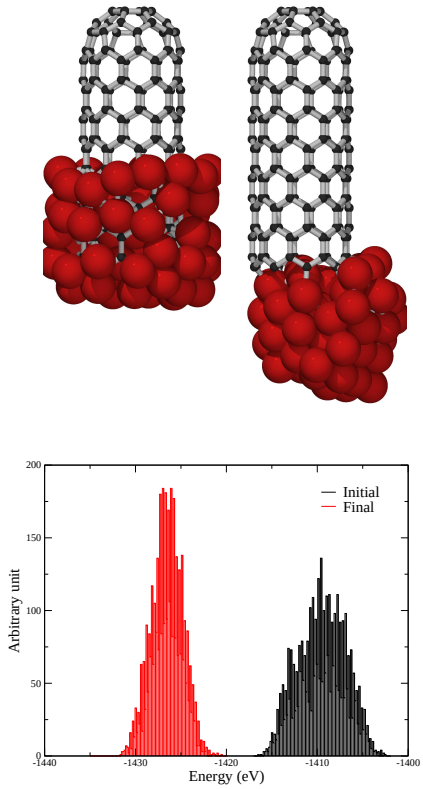

Figure 6.11: Capped (9,0) SWNT with nickel atoms randomly distributed over the inside and outside of the lower part of the nanotube wall (top left) and the 1500 K equilibrated structures obtained when the SWNT is held rigid (top right). The Ni atoms retract to the SWNT end and if the SWNT is allowed to relax some C atoms may be dissolved into the formed Ni cluster (not seen in figure). The total energy histograms for the initial and final configuration obtained for the rigid SWNT. The system is seen to gain approximately 20 eV by retraction to the SWNT end.

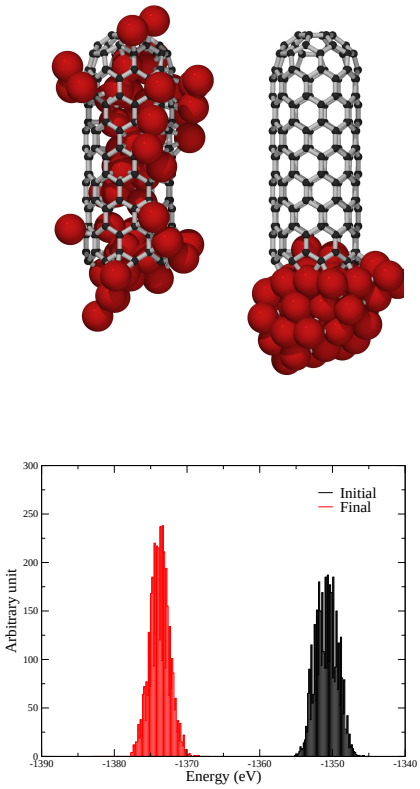

Figure 6.12: Capped $(9, 0)$ SWNT with nickel atoms sparsely distributed, by random on the inside and outside of the nanotube wall (left) and the 1500 K equilibrated structure (right). The total energy histograms (bottom) for the initial and final configuration shows that the system gains slightly more than 20 eV by the formation of a Ni cluster at the SWNT end.

at least one C neighbour within the distance $d_{CNi} < 2.3$Å. Bulk Ni atoms were defined as Ni with at least 6 Ni neighbours within distance $d_{NiNi} < 2.5$Å while surface Ni had less than 6 Ni neighbours. Neither bulk nor surface Ni had any C neighbours.

The retraction to end can be understood by considering Fig. 6.13, showing the local energy distributions for bulk, surface and interface Ni atoms for a $(10, 0)$ SWNT gently docked to a Ni_{55} cluster. The interface atoms inside the SWNT are explicitly shown in the bottom panel. The energy distributions for Ni atoms are centred around -4.0 eV for bulk Ni, -3.6 eV for interface Ni and -3.4 eV for surface Ni while the energies for Ni atoms situated in the interior of the SWNT are distributed around -3.6 eV. This means that Ni atoms will retract from the SWNT if this leads to an increase in the number of bulk Ni atoms, i.e. lowering the potential energy of the Ni cluster. A further consequence of this is that small Ni clusters, with few bulk atoms but many surface atoms, might favour interface positions as opposed to surface positions, i.e., diffuse into the CNT. This is in agreement with results from other studies, suggesting that CNTs may absorb nanoparticles below a critical size[193].

The C dissolution into the Ni clusters could be analysed by a similar approach as discussed above. This does however put very high demands on the accuracy of potential energy surface.

comparable.

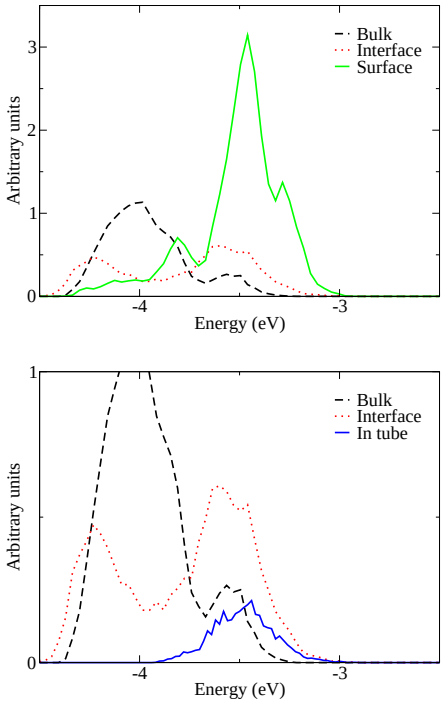

Figure 6.13: Local energy distributions of Ni atoms for the initial configuration of a $(10, 0)$ SWNT gently docked to a Ni_{55} cluster. The energy distributions of bulk, interface and surface atoms are seen in the top panel. The energy distributions of bulk, interface and Ni atoms inside the CNT (intube Ni) are seen in the bottom panel.

Since the limitations of the TB potential energy surface are not completely known this will not be discussed further in the thesis. Instead, the C dissolution will be discussed in association with the DFT study presented in Paper III.

6.3 Paper III - CNTs on Ni-carbide clusters

In Paper II, the effect of different docking procedures of metal clusters to open CNT ends were studied. As the forced docking procedure may cause dissolution of C in metal particles it is relevant to know what is the likely long time behaviour of these carbide systems, i.e., will they remain stable or are they likely to change in time. Studies of metal carbides attached to CNTs may also provide useful information about the properties of the CNT and catalyst during CNT growth and continued growth. For two reasons only DFT calculations were included in this study although the TBMC method was used in previous studies. The first reason was that the TBMC method could not describe chirality effects in a sufficiently accurate way. The other reason is that the study of systems with CNTs, dissolved C atoms, Ni and Ni-carbide raises very high demands on the transferability of the PES. This means that although the TBMC method may reproduce the qualitative trends more complicated effects, e.g., the C concentration in carbide clusters, must be treated in a better way. Merely the use of DFT does not a guarantee a high transferability as both the pseudo potentials (or PAW potentials) and the *xc*-functional are approximations. While the majority of the DFT calculations were performed using VASP with US-PPs and the PW91 *xc*-functional, some additional control calculations were performed with the DFT program GPAW, using a the PBE *xc*-functional and a DFT implementation based on PAW-potentials. As these calculations were extremely expensive, only two different structures were used for the control calculations and with the parameters chosen, the GPAW calculations had a lower accuracy than the VASP calculations, i.e., they would correspond to VASP calculations with a PW energy cutoff of less than 400 eV.

The calculations were performed for $(3,3)$, $(5,5)$, $(9,1)$ and $(10,0)$ SWNTs that were either attached to pure Ni_{55} clusters or $Ni_{55}C_{20}$ carbide clusters. As both systems have the same number of Ni and C atoms the total energies are directly comparable. The same holds for the systems with $(5,5)$, $(9,1)$ and $(10,0)$ SWNTs for which the total energies can be directly compared to determine the relative stability of these systems.

The complexity of these systems means that the results of the calculations are very sensitive to the atomic starting configurations used. To reduce this effect, several qualitatively identical systems, e.g., a CNT of a certain chirality attached to an amorphous Ni_{55} cluster, were created for every type of system. The systems were also subjected to MD simulation prior to relaxation in order to reduce the effect further. Although there may still be an effect of the starting configuration, as illustrated in Fig. 6.14, this should not affect the qualitative results presented in Paper III.

6.3.1 Results

In short, the calculations have shown that a CNT attached to a pure Ni cluster is energetically favoured compared to the same CNT attached to a Ni carbide. This can be seen in Fig. 6.15 and is also seen by a comparison of the rows for the same CNT-metal system in top and bottom tables of Fig 6.16. From the tables of Fig. 6.16, it is also clear that the adhesion energies between CNTs and clusters are higher for carbide clusters compared to pure metal clusters, i.e., the attachment of carbide clusters is weaker than the attachment of pure clusters. However, the difference adhesion energy between the CNT and the pure and carbide clusters is small compared to the total adhesion energy, i.e., the difference in adhesion is only a few eV while the total adhesion energy is in the order of 15 - 25 eV. This indicates that if the

adhesion energy is strong enough for the CNT to remain attached to the pure Ni particle it will most likely remain attached to the Ni carbide as well. This means that the Ni-carbide clusters will remain stable on the CNT ends in the sense that they are firmly attached and will not easily detach.

A comparison of the total energies of systems with a CNT attached to pure Ni and Ni-carbides shows the energy differences in the order of 7 - 10 eV in favour of the system with pure metal. This energy difference indicates that given the choice the CNTs are most likely to be attached to pure metal cluster. Consequently, a CNT formed on, or mechanically attached to, a Ni(-carbide) cluster will serve as a sink and drain any eventual C atoms from the Ni particle and thus end up attached to a pure Ni cluster.

Both the total energies and the adhesion energies between CNTs and clusters were dependent on the C concentration in the cluster and both energies were seen to increase gradually with increasing C concentration. For the total energies this can be seen in Fig. 6.17, showing a $(9, 1)$ CNT attached to Ni(-carbide) clusters with 0, 6, 14 and 20 dissolved C atoms. For this CNT the total energy of the carbide with 20 C atoms is approximately 9 eV higher than for the corresponding system with a pure Ni cluster. A similar trend is observed for individual (carbide) cluster and CNT systems as well. From these results it could be deduced that the greater stability of systems with pure Ni, as compared to systems with Ni-carbide, is joint property of the greater stability of the Ni cluster and the CNT when the C atoms are bound in the CNT, i.e., a higher stability of the local atomic environment, and the weaker adhesion between CNTs and Ni carbides. Remembering the local energies discussed in Paper II it was seen that C atoms were most stable when part of a sp^2 network while the stability of Ni atoms were comparable when being in the bulk or neighbouring dissolved C atoms. Similar arguments may explain these results as well although no such energies are available in a DFT calculation. This means that the driving force for the draining of carbon atoms from the cluster into the CNT may also be a joint effect of higher atomic stability and a stronger adhesion. Hence, it may also be argued that if C atoms are added to the carbide cluster at a rate that is similar to the rate of C inclusion into the CNT, the driving force is only due to the increased stability of the atoms as the adhesion energy remains constant.

Another interesting result in Paper III was that, in correspondence with the results in Paper II, the CNT end retain it's shape and chirality when attached to a metal carbide, i.e., the CNT is attached to the cluster surface and appears to have no roots below the cluster surface. Together with the results of Paper II, this indicates that the docking procedure may not be crucial for the continued growth of CNTs as the Ni-carbide may be drained of C atoms, i.e., forming a pure Ni cluster. A similar argument suggest the docking procedure may not be crucial for the creation of electric contacts between CNTs and metal as the metal can be purified if a metal carbide is undesirable. This may however require an annealing of the created junctions as the temperatures relevant for electronics may be to low to achieve significant C diffusion in the metal particles while the temperatures relevant to continued CNT growth may allow this to spontaneously occur.

So far, the arguments were based on DFT calculations at 0K which may be a limitation as CNTs are typically handled at higher temperatures. In order to verify that these results did not change as temperature effects (vibrations) were introduced, finite temperature MD simulations of a $(9, 1)$ attached to a Ni_{55} and $Ni_{55}C_{20}$ were performed. These simulations showed that the trends with lower energies of the pure metal systems compared to the carbide systems holds even at higher temperature. The adhesion energies were strong enough to keep the clusters firmly attached to the CNTs but the trend that the adhesion between pure Ni

and CNTs is stronger than the adhesion between Ni-carbide and CNTs could only be seen as an indication because of the large energy fluctuations. It is however possible that this could be seen more clearly in longer simulations which would allow for better statistics than what could be achieved for these DFT calculations.

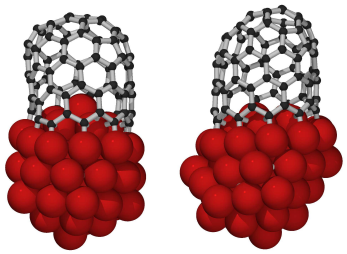

Figure 6.14: Relaxed structures of a $(9, 1)$ CNT attached to an icosahedral (left) Ni_55 cluster and an amorphous dito (right). The energy difference of approximately 3 eV illustrates that there is an effect of the geometry of the Ni cluster.

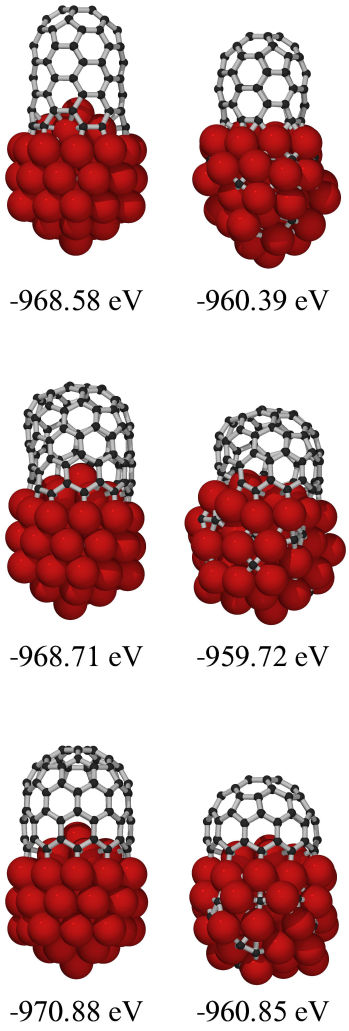

Figure 6.15: Typical relaxed structures of CNTs attached to pure Ni clusters (left column) and to Ni carbides (right column). The chiralities of the CNTs are $(5,5)$ (top), $(9,1)$ and $(10,0)$ and all clusters contain 55 Ni atoms. All systems contain an equal number of C and Ni atoms respectively to make the total energies directly comparable. To form the carbide clusters, 20 C atoms have been dissolved into the $Ni_5 5$ cluster, i.e. forming a $Ni_{55}C_{20}$ carbide.

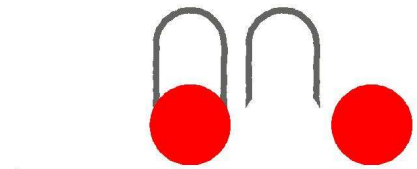

Chirality	CNT-Ni_x	CNT	Ni_x	Adhesion
(3,3)	-387,44	-326,98	-50,06	-10,4
(5,5)	-968,58	-701,75	-250,61	-16,22
(9,1)	-968,71	-695,45	-250,61	-22,65
(10,0)	-970,88	-695,08	-250,61	-25,2

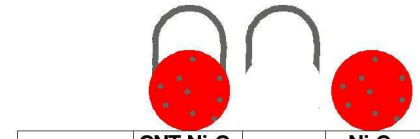

Chirality	CNT-Ni_xC_y	CNT	Ni_xC_y	Adhesion
(3,3)	-385,66	-274,53	-100,71	-10,38
(5,5)	-960,39	-520,01	-426,48	-13,9
(9,1)	-959,72	-513,26	-426,48	-19,98
(10,0)	-960,85	-513,07	-426,48	-21,3

Figure 6.16: Total energies and adhesion energies of $(3, 3)$, $(5, 5)$, $(9, 1)$ and $(10, 0)$ CNTs attached to pure Ni clusters (top) and Ni-carbide clusters (bottom). The adhesion energies between CNTs and clusters are seen to be slightly higher for the carbide clusters compared to the pure metal clusters.

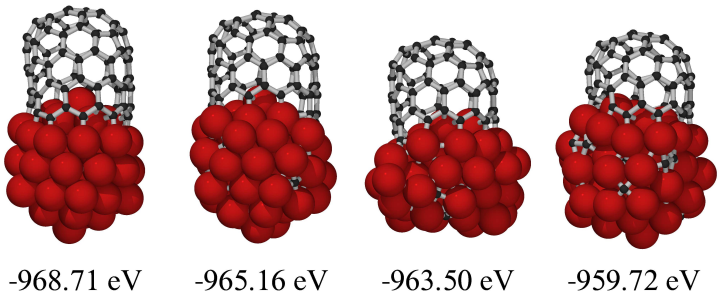

Figure 6.17: Relaxed structures and energies for a $(9, 1)$ CNT attached to Ni(-carbide) clusters. The carbon content in the cluster is 0, 6, 14 and 20 C atoms while the total number of C atoms is held constant, i.e., all systems have 80 C atoms. The total energy increase with increasing carbon content and it is argued that this energy increase is partially due to the geometrical distortion of the structure and partially due to the decrease in energy due to C dissolution.

6.4 Paper IV- Properties of C atoms and CNTs on Ni clusters

The work presented in Paper IV extends the work presented in Paper II and the work presented in another study conducted within the group[194]. In the latter it was seen that there may be a maximum cluster size for growing CNTs of a certain chirality and that if the cluster size is larger diameter, the CNT may also increase in diameter. Hence, it may continue it's growth as a CNT with different chirality.

In this study the opposite question was addressed, i.e., the possible existence and reason for a minimum cluster size needed for successful CNT growth. According to experiments[57, 60] CNTs are typically grown from clusters of with diameters of $1.1-1.6$ times the CNT diameter.

Following the results of Paper II, the focus of this study was on Ni clusters that are gently docked onto either open CNT ends or fullerenes. The gentle docking meant that the C structures were not deformed in the production stage and that the initial potential energies were low, i.e., the C structures were not deformed during subsequent relaxation or simulation. Hence, the C structures could truly be considered as ideal CNTs and fullerenes. The studies were performed with a combination of 0K DFT calculations and TBMC calculations at finite temperatures relevant to CNT growth, typically 1000K. The exact computational details are found in Paper IV.

The study focussed on $(5,5)$ and $(10,0)$ SWNTs that were attached to Ni clusters of different size and the stability of these systems were compared to systems where fullerenes were formed by closure of the two CNTs respectively. Some typical example structures are seen in Fig. 6.18 where a $(10,0)$ and a C_{80} fullerene have been attached to Ni_{10}, Ni_{25} and Ni_{55} clusters. This comparison of energies made it possible to elucidate whether it is energetically favourable for a CNT-Ni system to retain it's shape or to encapsulate to form a fullerene instead, i.e., whether it is likely that the CNT end remains open.

In Paper IV and Fig. 6.19, the DFT energies are given for the atomic system relative the energy of a system containing the Ni cluster and n C atoms in a graphene sheet, i.e.,

$$E = \mathrm{E}_{nC-Ni_{cluster}} - \mathrm{E}_{Ni_{cluster}} - n\,\mathrm{E}_{C_{graphene}} \tag{6.1}$$

This had the advantage over comparisons of total energies that systems with different number of atoms are directly comparable. A negative relative energy indicates that the system is more stable than the free Ni cluster and C atoms in graphene while a positive energy indicate the opposite. In the comparison between different systems, a system with a lower relative energy is more stable than a system with a higher relative energy. The relative energy takes into account both the adhesion between Ni and C systems and effects of deformation and curvature of the C structure. To avoid confusion, the relative energies are introduced here since the energies in Fig. 6.19 are given as relative energies but they serve no deeper purpose in the analysis presented. The TBMC calculations were only used to compare the stability of systems with an equal number of atoms and hence, the total energies of different systems could be directly compared and there was no need to introduce the relative energy.

6.4.1 Results

When comparing the energies of $(5,5)$ and $(10,0)$ CNTs with the energies of fullerenes attached to Ni_{10} clusters, it was seen that the fullerene systems were favoured by approximately 1.5 to 4 eV over the corresponding systems with CNTs. This means that a cluster with 10 Ni atoms is not sufficiently large to stabilise CNTs. Hence, if such a small cluster was to

be docked onto a CNT end it would eventually result in the closure of the CNT. A similar trend was observed when Ni_{25} clusters were attached to the same CNTs and fullerenes while the attachment of Ni_{55} clusters lead to the opposite trend, i.e., the system with a CNT and a cluster was energetically favourable. These results are illustrated in Fig. 6.18 where the approximate energy differences are given for the three different cluster sizes and CNTs. In the figure the existence of energy barriers for the CNT closure have been indicated. The height of these barriers have not been investigated in this work although the existence of the barriers is seen. Two indications of the existence barriers, based on DFT calculations, are that CNTs do not spontaneously close during relaxation nor do they close during MD simulation at high temperature, e.g., the simulations performed in Paper III. During the MD simulation, a slight diameter decrease of the lowest CNT ring could however be observed for some CNTs and this may a first step towards closure. The CNTs were not seen to close during the long TBMC simulations at 1000 K, which may constitute another indication that an energy barrier has to be overcome in order to achieve CNT closure. It is however likely that closure may be observed for longer simulations than what could be practically achieved during the time of the study.

When performing similar calculations for a few more clusters sizes, it was seen that cluster sizes of approximately 40 Ni atoms are required in order to keep both the $(10, 0)$ and $(5, 5)$ CNT ends open. The results of these calculations are seen in Fig. 6.19 where the relative energies are given as functions of the cluster size.

These results were obtained at 0K but in order to understand CNT growth it is important to study the same systems at finite temperature when the thermal vibrations may alter the binding between C structures and metal. The temperature effects were included by using the TBMC method at 1000K for systems with 10, 25 and 55 Ni atoms using the same atomic structures used for the DFT calculations. The total energy histograms for $(5, 5)$, $(10, 0)$ and fullerenes attached to the Ni clusters are given in Fig. 6.20. As seen in Fig. 6.20, the same trends as for the DFT calculations were obtained with the TBMC method, i.e., only the Ni_{55} cluster was sufficiently large to keep the CNTs from closure. In the energy histograms in Fig. 6.20 there is an overlap between the peaks for CNT and fullerene systems, i.e., the reported trends are visible as an average behaviour but may not be true for every possible atomic configuration. For example there are atomic configurations, that are likely to occur at 1000 K, for which it is more stable to have a Ni_{55} cluster attached to a fullerene compared to a CNT. This is however not true for most of the likely configurations. This overlap does also indicate that if the energy barrier of going from a CNT to a fullerene is small, the barrier may be overcome at these temperatures. Depending on the the situation, this may cause CNT closure with the possible abortion of the CNT growth. The calculation of energy barriers is however a highly complicated question that was not addressed in the study.

As discussed above, the smallest clusters that are able to keep the $(5, 5)$ and $(10, 0)$ CNTs open appears to be in size of approximately 30 - 45 atoms which corresponds to a diameter between 8.4 and 9.4 Å. These diameters are slightly larger than the diameters of the CNTs which are 6.8 Å for the $(5, 5)$ and 7.8 Å for the $(10, 0)$. This indicates that the radius of the smallest clusters able to keep CNTs open should lie in the size interval of 1.1 to 1.3 times the CNT diameter. This is close to the results found experimentally[57, 60] where CNTs were seen to grow from clusters in the size range of $1.1 - 1.6$ times the CNT diameter.

As two final speculations and possible continuations of the project one can imagine that the CNT-metal adhesion will affect the minimum cluster size needed for successful CNT growth since more energy is needed to compensate for the decreased number of C-C bonds of the CNT

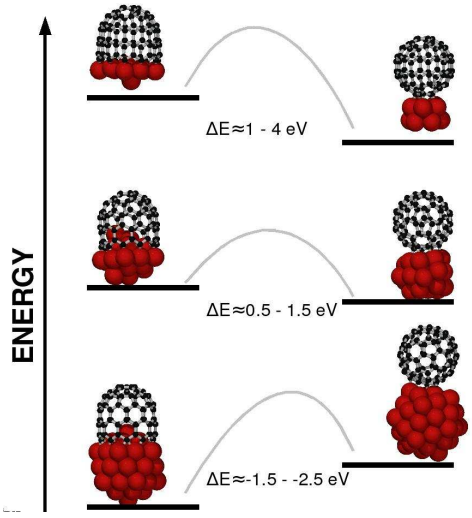

Figure 6.18: Typical minimum energy configurations and the energy differences between systems with CNTs and fullerenes attached to Ni clusters with 10 (top), 25 (middle) and 55 (bottom) atoms. The systems with a fullerene attached to a Ni cluster are more stable for the smaller clusters while the systems with a CNT attached to the cluster are more stable for the larger clusters. The energy barriers visible in the figure serve as a reminder that CNT closure is associated with a barrier although the height of the barrier was not investigated in the study. The approximate energies given are for both zig-zag and armchair CNTs.

compared to the fullerene. This means that a metal with weak CNT-metal adhesion, e.g., Au[54], may require a larger cluster to grow CNTs compared to a metal with strong CNT-metal adhesion, e.g., Ni. Another similar idea is that there may be a difference in minimum cluster size for zig-zag and armchair CNTs since the adhesion between the CNTs and metal clusters is different. These two ideas that remains to be investigated in later studies.

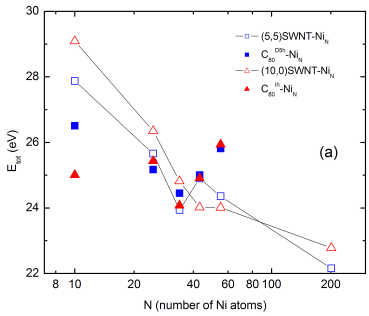

Figure 6.19: The relative stability for $(10, 0)$ and $(5, 5)$ CNTs and fullerenes attached to clusters of sizes 10, 25, 34, 43 and 55 Ni atoms. The systems with fullerenes are more stable for smaller clusters while the systems with CNTs are more stable for the larger clusters. The shift in stability appears in the size interval 30 to 40 Ni atoms. The figure is adapted from Ref. [185].

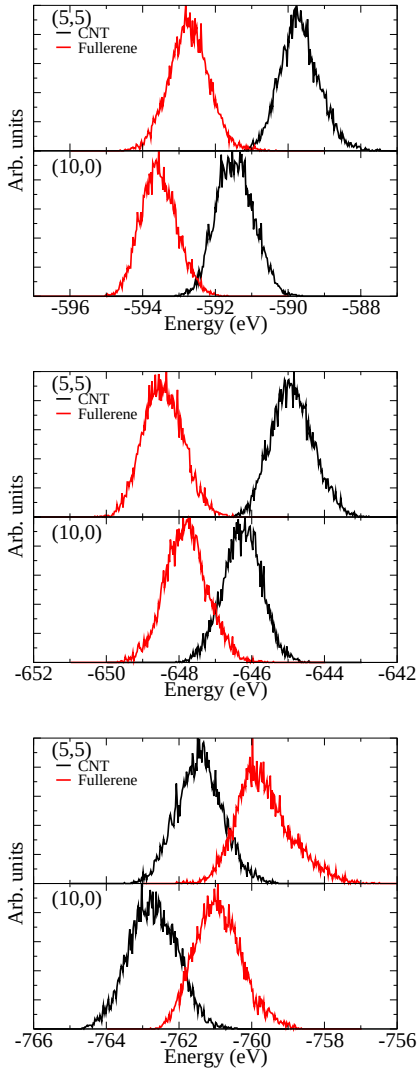

Figure 6.20: Total energy histograms obtained at 1000K with the TBMC method for CNTs and fullerenes attached to clusters of sizes 10, 25 and 55 Ni atoms. From the histograms it is clear that only the Ni_{55} is likely to be able to keep the CNT end from closure.

6.5 Paper V - The effect of Ostwald ripening of Ni clusters attached to CNTs

The strength of CNTs make them an appropriate material for use as reinforcement in compounds. e.g., polymer materials. The strength of the composite is increased by reinforcement with long, directionally aligned CNTS[195] as compared to short and randomly aligned CNTs. These results may become very important in future applications required that it is possible to produce substantial amounts of long CNTs that can be directionally aligned when dispersing them in the polymer melt. Today, one problem is that the CNT growth stops spontaneously after a certain growth time and hence, induce a limitation on length of the CNTs. Water assisted CVD growth[77, 78] (super growth) has proved to be an efficient method to increase the growth time and that it allows for growth of dense mm long CNT forests. However, the maximum length of the CNTs is still limited and the growth can not be maintained for arbitrarily long time

Recent reports provide an, at least partial, explanation of the success of super growth as the presence of water in the growth chamber may also inhibit the process of Ostwald ripening of the catalyst particles[74]. It was discussed that the catalyst deactivation may be due to a combination of Ostwald ripening and diffusion of the catalyst particles into the substrate material[75, 76]. One step to enhance the CNT growth time, and hence yield, may be to understand the parameters of the Ostwald ripening of the catalyst particles. This may also be a way to achieve chirality separation if there is a difference in the Ostwald ripening rate of catalysts attached to CNTs of different diameters and chirality.

This issue was addressed by a combination of DFT calculations, presented in Paper V, and numerical modelling, presented in Paper VI. The DFT calculations were performed using VASP for the $(3,3)$, $(4,4)$, $(5,0)$, $(6,0)$ and $(8,0)$ CNTs attached to Ni clusters containing between 15 and 60 Ni atoms. Some examples of initial structures are seen in Fig. 6.21.

In addition to the systems described above, the discussion about the atomic energies in Paper V involves $(5,5)$ and $(10,0)$ CNTs attached to icosahedral Ni_{55} clusters. These starting configurations were obtained from the relaxed structures discussed in Paper III. The results of Paper II, stating that the cluster will form a droplet at an uncompromised CNT end were considered in the construction of starting configurations.

6.5.1 Results

Ostwald ripening is driven by the energy gained by increasing the number of bulk atoms and reducing the number of surface atoms, i.e, by taking surface atoms from small clusters and adding them to larger clusters and thereby increasing the bulk. Since Ostwald ripening is driven by energy differences in an ensemble of clusters, the smallest smallest number of particles that can constitute an ensemble, and hence experience Ostwald ripening, is two. For that reason, the energy comparisons in Paper V were done for these small ensembles containing only two clusters. In the following discussion these small ensembles will be referred to as sets while the constituents of the set will be referred to as structures, e.g. a set may contain two clusters each of which is referred to as a structure.

To verify that these nano sized systems would, according to the DFT calculations, experience Ostwald ripening a few control calculations were performed for free clusters, i.e. clusters that were not attached to any CNTs. These results showed that one larger cluster was significantly more stable than a two smaller clusters containing the same number of atoms and

hence, Ostwald ripening will occur at the proper conditions.

When performing similar calculations on the sets with Ni clusters attached to CNTs, it was seen that that Ostwald ripening may occur for these systems as well. The Ostwald ripening process may however be more complicated as the effects from CNTs are included as well. An illustration of this is seen in Fig. 6.22 where the total energies of sets containing two $(5, 0)$ CNTs attached to a total of 30, 40 or 50 Ni atoms are given. The Ni atoms were either distributed equally, i.e., both CNTs had a cluster of the same size, or on only one of the CNTs leaving the other CNT with an open, unpassivated end. For the sets with 30 Ni atoms, it is energetically more stable when both CNTs have a cluster compared to only one having the larger cluster. For the sets with 40 Ni atoms the stability is approximately the same for both sets while for the sets with 50 Ni atoms the set with one large cluster is favoured over the set with two smaller clusters. This indicates that Ostwald ripening may not occur for all cluster sizes and that there may be a minimum cluster size needed to compensate for leaving dangling C bonds at the CNT end. Similar studies for other CNT chiralities showed that the minimum cluster size needed increased with increasing CNT-cluster adhesion strength. This means that zig-zag CNTs require larger Ni systems than armchair CNTs and that CNTs with larger diameters (more C bonds at the end) require larger clusters than thinner CNTs.

The difference in the description of Ostwald ripening between free clusters and clusters attached to CNTs can partly be associated with the two different "sources of energy", i.e., the higher stability of cluster atoms in the bulk compared to atoms at the surface and the C-metal binding energy at the CNT lips. This suggests that there should be an energy balance between the energy that can be gained by an increase in the bulk of the cluster and the energy that can be lost by decreasing the number of C-metal bonds.

To study the stability of individual atoms, the concept of atomic energies was introduced. These energies were calculated as the energy cost of removal of a particular atom, i.e., the atomic energy of atom i is defined as

$$E_i^{\text{atomic}} = E_N - E_{N-i} \tag{6.2}$$

where E_N is the total energy of the full system with N atoms and E_{N-i} is the total energy of the same system but with atom i excluded (the system with atom i removed is not relaxed as this would ideally would give the same energy for all i). The analysis of these atomic energies is analogous with the analysis if the local energies of the TB method, as discussed in Paper II, although the physical meaning of the two concepts are fundamentally different.

Analysis of the atomic energies at the junction between the CNT and the cluster showed that the CNT result in a local stabilisation of the Ni surface atoms near the CNT. An example of this is seen in Fig. 6.23 where the stability of Ni atoms in the bulk, on the surface and on the CNT interface have been indicated for a $(3, 3)$ CNT attached to Ni_{25} and Ni_{50} clusters. For the larger cluster, Ni atoms on the CNT interface have a stability that is comparable to the bulk stability while the surface atoms have a lower stability. For the smaller cluster, the interfacial atoms are less stable than the bulk although still more stable than surface atoms. On the other hand, if the cluster is small the fraction of atoms that are stabilised either in the bulk or by the interface may be larger than for a slightly larger cluster. This means that a small cluster may be favoured compared to a slightly larger cluster although a much larger cluster is favoured over the small cluster.

The observations of the atomic energies lead to the idea that the Ostwald ripening behaviour of the clusters could better be described by a critical factor, taking both the cluster

size and the local stabilisation into account. It could also be argued that the critical factor may induce an extreme point in the cluster stability. The details of the extreme point are most likely to be determined by the CNT diameter, CNT-metal adhesion and size distribution of the clusters in the ensemble. This means that the Ostwald ripening may not only lead to atomic diffusion from the smaller clusters to the larger but also that atoms may diffuse from both smaller and larger sizes to a particular size near the extreme point of the stability.

This is illustrated in Fig. 6.24, where the stability of a set with two $(6,0)$ CNTs with 20 Ni atoms each is compared to a set where the the Ni atoms are distributed 15 atoms on one CNT and 25 atoms on the other CNT. The system with equal distribution is favoured by approximately 0.9 eV, indicating that a system with two smaller clusters of approximately the same size will lead to a ripening towards the more stable, intermediate size. In Fig. 6.25, the same situation is seen for a $(4,4)$ CNT and 80 Ni atoms distributed equally or 30 on one CNT and 50 on the other CNT. Once again the set with equal cluster size was the most stable although the stable cluster size is larger than for the $(6,0)$ CNT. It can be noted that the energy differences in these calculations are relatively small and may contain an effect of the optimisation process. Although this is true the trends should be trustworthy since the same trend is observed for all systems included in the study. This support the idea that the cluster stability may have an extreme point and it does also indicate that the extreme point depends on the CNT diameter. This is reasonable considering two clusters of the same size but attached to CNTs of different diameter. Then the fraction of cluster atoms that are stabilised by the CNT must be larger for the CNT with larger diameter. For CNTs, this is particularly important since it may mean that CNTs of a certain diameter may keep their clusters for a significantly longer time than other CNTs although the initial cluster size distributions were similar.

As the potential diameter dependence on the Ostwald ripening has been established it is also interesting to investigate whether there is a preference among the chiralities in a distribution. This can be expected from analysis of the atomic energies, as seen in Fig. 11 in Paper V, showing that the atomic stabilisation at the interface is stronger for a $(10,0)$ CNT compared to a $(5,5)$ CNT. It is then reasonable to expect that zig-zag CNTs, having stronger CNT-cluster adhesion, have a stronger stabilising effect than armchair CNTs.

This was verified by considering sets with one $(6,0)$ and one $(3,3)$ CNT and a total of 50 Ni atoms. A comparison of the total energies when the Ni atoms were distributed equally, only on the $(3,3)$ CNT or only on the $(6,0)$ CNT indicate that it is more stable to have all Ni atoms on the $(6,0)$ CNT compared to the other situations. This means that in an ensemble with different CNT chiralities, the zig-zag CNTs are less affected by the Ostwald ripening and hence more prone to keep the clusters attached. The same behaviour was observed for a set with a $(4,4)$ and $(8,0)$ and a total of 60 Ni atoms as seen in Fig. 6.26

The above discussion indicates that the critical factor governing the Ostwald ripening should depend on both the CNT diameter and chirality. Since the arguments were partly based on observations of the atomic energies it is reasonable to state that the critical factor can be constructed from local properties of the clusters in an ensemble. This will be discussed further in Paper VI where a simple model for the stabilisation is constructed.

Some of the calculations presented above have assumed that the Ostwald ripening of the smaller clusters will result in CNTs with open ends, i.e., having a number of dangling C bonds at the end. This is may not be case in an experimental situation where substrate, feedstock and residue molecules may passivate the open CNT ends. The effect of passivation was evaluated by a few calculations where H_2 molecules were allowed to dissociate and attach

to the end. This meant a radical change to the trends reported above. When passivation was taken into account, the zig-zag CNTs were more stable when forming a large cluster on one CNT while the other CNT end was passivated as compared to having two small clusters on each CNT and the H as H_2 molecules in the medium. In effect, this means that the minimum cluster size needed for Ostwald ripening to occur may be decreased by continuous passivation of the CNT end. The same trend was seen for the armchair CNTs although the effect was less pronounced. This preserves the effect of the chirality on the Ostwald ripening although the details vary with the external conditions. Another possible scenario can be associated to the results in Paper IV, i.e., the CNTs may close when the cluster becomes to small. This may as well lead to abortion of the CNT growth before all metal atoms have diffused from the CNT end.

In this study no effects of the substrate were taken in to account since calculations of CNT-cluster systems mounted on substrates is not feasible with DFT calculations. It is reasonable to believe that the substrate would affect all metal clusters in the same way and hence it would not change the effects induced by the CNTs. This will be discussed in association with Paper VI.

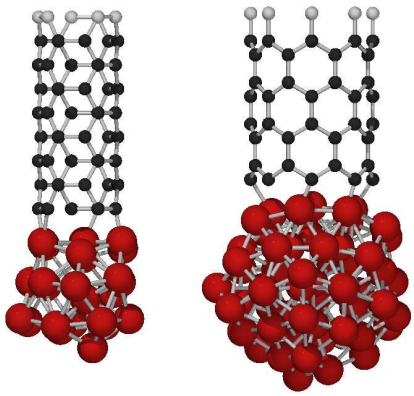

Figure 6.21: Two typical input structures to the DFT calculations. The structures are for a $(3,3)$ CNT attached to a Ni_{25} cluster (left) and for a $(8,0)$ CNT attached to a Ni_{60} cluster (right).

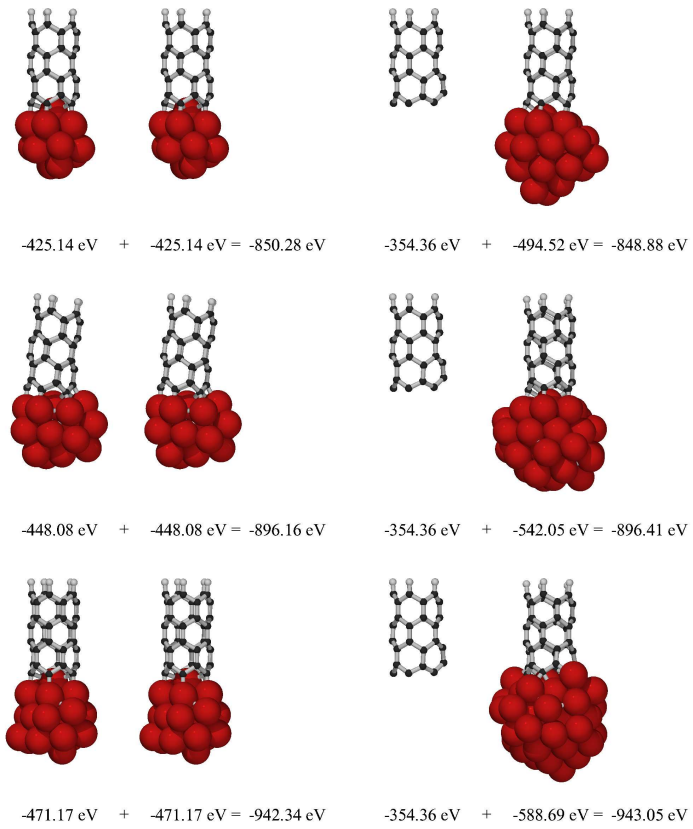

Figure 6.22: The optimised geometries and total energies of two $(5, 0)$ CNTs attached to 30 (top), 40 (middle) and 50(bottom) Ni atoms. The atoms are either distributed equally (left) or only on one CNT (right). If the cluster size is less than approximately 40 Ni atoms it is energetically favourable to keep one small cluster on each CNT while if the number of atoms becomes larger, it is energetically favourable to have one larger cluster and one open CNT end. Although the energy differences here are relatively small the conclusions are supported by the similar trends observed for other systems as well.

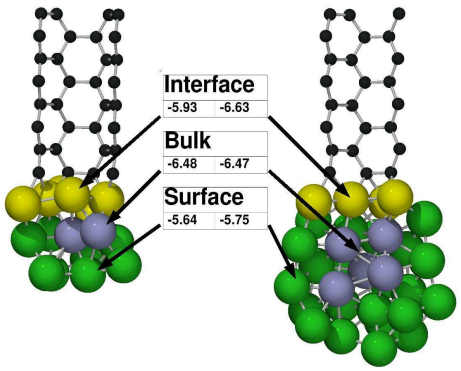

Figure 6.23: The atomic energies for bulk (blue), surface (green) and interfacial (yellow) Ni atoms for system with $(3, 3)$ CNTs attached to Ni_{25} (left) and Ni_{50} (right) clusters. The energies given are the average for each atomic category.

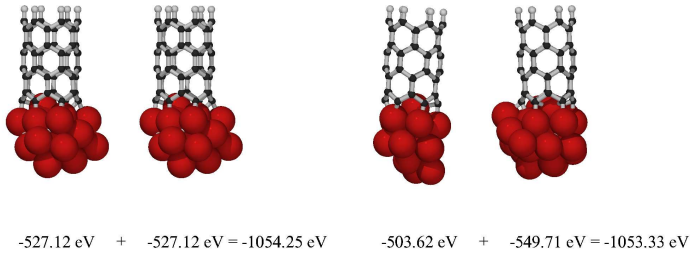

Figure 6.24: The optimised geometries and total energies of two $(6, 0)$ CNTs and 40 Ni atoms, distributed either equally on both CNTs (left) or 15 atoms on one CNT and 25 atoms on the other (right). The situation with equal Ni distributions is seen to be the most stable situation.

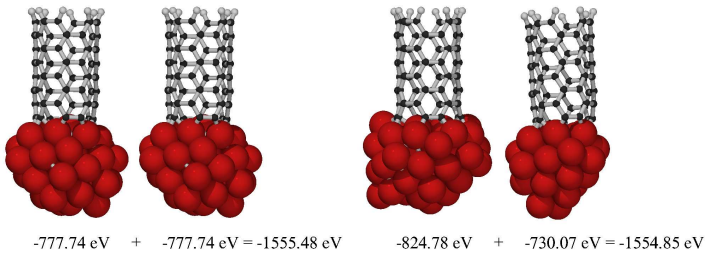

Figure 6.25: The optimised geometries and total energies of two $(4, 4)$ CNTs and 80 Ni atoms, distributed either equally on both CNTs (left) or 30 on one CNT and 50 on the other CNT (right). The situation with equal Ni distributions is seen to be the most stable situation. The larger diameter CNT appears to increase the stable clusters size as seen from a comparison with Fig. 6.24.

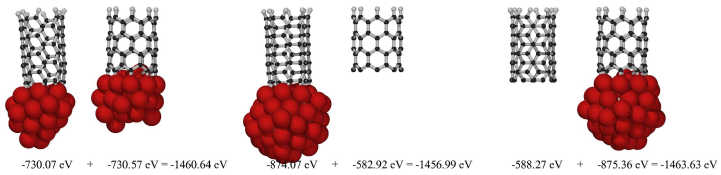

Figure 6.26: The optimised geometries and total energies of $(8, 0)$ and $(4, 4)$ CNTs and a total of 60 Ni atoms. The Ni atoms are either distributed equally (left), only on the $(4, 4)$ CNT (middle) and only on the $(8, 0)$ CNT (right). It is energetically favourable to have all Ni atoms on a cluster on the $(8, 0)$ CNT compared to the other distributions while a it is more stable to have the Ni atoms distributed equally as compared to having all Ni atoms on the $(4, 4)$ CNT.

6.6 Paper VI - Modelling of Ostwald ripening of clusters attached to CNTs

The DFT calculations of Ostwald ripening of the metal catalysts in Paper V were followed by numerical modelling of atomic diffusion in an ensemble of Ni clusters attached to CNTs. The modelling aimed at extending the DFT results of Paper V in order to study the time evolution of CNT-cluster ensembles. The spirit of the modelling was very similar to what has been described by DeSmet *et al.*[196] with the difference that the Ostwald ripening of free clusters is governed by the critical size only and not the critical factor. Hence, the effects of CNTs had to be introduced and the modelling slightly modified to include this in a consistent way. Another difference is that the modelling is (numerically) very intricate for small systems, i.e., the systems of relevance to CNT growth. This is due to the expression

$$C(r) = \exp\left(\frac{\alpha}{r}\right) \approx 1 + \frac{\alpha}{r} \tag{6.3}$$

describing the concentration of a substance at the surface of a spherical drop in a medium. If $\alpha \ll r$ the exponential function can be approximated by the first two terms of the Taylor expansion and this is the common practice in simulations of Ostwald ripening, e.g., the results of Ref. [196]. As discussed in Paper VI this approximation is not valid for the cluster sizes relevant to CNT growth, i.e. clusters in the order of a few nm. Consequently a more complicated procedure where the exponential is taken care of explicitly is necessary. The derivations of the equations governing the Ostwald ripening and the numerical "trick" used in the modelling are extensively discussed in Paper VI and will not be discussed further. Instead the focus will be on some particular considerations taken in the study and on a few of the most interesting results.

The model for inclusion of CNT effects on the clusters was based on some observations from previous DFT calculations. The first observation, discussed in Paper V, was that the effect of the CNT can be considered as local, i.e., the stabilisation of Ni atoms at the CNT interface do not affect Ni atoms further away from the CNT lips in a significant way. The second observation, also discussed in Paper V, was that an increased adhesion strength between the CNT and metal lead to an increased stability. The third observation, presented in Paper II, was that a cluster will form a drop at the CNT end and that the the cluster adapts to the shape of the CNT and not *vice versa*. Larger clusters at CNT ends were not seen to take any particular geometries but were more or less spherical. The fourth observation was that when the cluster becomes very small, it is energetically favourable to form a metal ring at the CNT end than a cluster. This will be discussed in some detail below and some DFT data will be presented.

For clusters with a radius larger than the CNT radius only the part of the cluster that is located directly under the CNT will be stabilised. This was modelled by the stabilisation of a spherical cap with the same radius as the CNT, as illustrated in Fig. 6.27(a). This means that at most half of the surface area can be stabilised while the rest of the cluster has an ordinary cluster surface. As the cluster decreases in size a part of the cluster may be inserted into the CNT. This was discussed in Paper II and Ref. [193]. This means that an increased fraction of the clusters surface atoms are stabilised. This is illustrated in Fig. 6.27(b) for a cluster partially inserted into the CNT. If the clusters are much smaller than the CNT radius the clusters will no longer have a spherical shape but instead become deformed in order to minimise the number of dangling C bonds at the CNT end. This is illustrated in Fig. 6.27(c) where all cluster atoms are stabilised. If the cluster is too small to form a cluster-like shape

at the CNT end without leaving any dangling C bonds the cluster is instead assumed to form a ring with the same diameter as the CNT. In that case, all Ni atoms are stabilised by the CNT.

The assumption that the Ni atoms form rings at the CNT ends is based on DFT calculations and the results of some of these calculations are presented in Figs. 6.28,6.29 and 6.30. These figures show the optimised structures and total energies for $(8,0)$, $(10,0)$ and $(13,0)$ CNTs attached to Ni systems with the same number of atoms as the number of C atoms at the CNT end, i.e., 8, 10 and 13 Ni atoms for the CNTs, respectively. The Ni systems are either formed as small clusters, planar flakes or rings. As the CNT diameter increase, the small Ni clusters can no longer saturate all dangling C bonds at the CNT end with the result that the formation of a ring becomes energetically favourable, i.e., it is favourable to form Ni-C bonds compared to the extra Ni-Ni bonds which would be present in the clusters but not in the rings. For the $(8,0)$ and $(10,0)$ CNTs, 8 and 10 Ni atoms appears to be sufficiently large to form clusters that are stable at the end while for the $(13,0)$ CNT, 13 Ni atoms is not sufficient, i.e., it is more stable to form a ring than a cluster. In the numerical model, all small Ni systems are stabilised as rings even though it may be favourable to have a small clusters instead for the smaller CNTs, e.g., $(8,0)$.

The cluster stabilisations, called σ, in Paper VI were given relative the stability of surface atoms of free clusters, i.e., $\sigma = 1$ correspond to a free cluster while $\sigma < 1$ correspond to a stabilised cluster. As the clusters may be partially stabilised different parts of the clusters may have different stabilisations, i.e., different σ-factors. In that case, the total stabilisation is is given as the sum of the partial stabilisations. Here, the total σ-factor is written as $\sigma = a_1\sigma_1 + a_2\sigma_2$ where $\sigma_1 = 1$ is for the free part, a_1, of the cluster and σ_2 is for the stabilised part a_2. In Paper VI, the armchair CNTs stabilise cluster atoms in their vicinity by 10% while zig-zag CNTs have a stabilising effect of 20%, corresponding to $\sigma_2 = 0.9$ for the region stabilised by an armchair CNT and $\sigma_2 = 0.8$ for the region stabilised by a zig-zag CNT. These stabilisation factors were not chosen with other considerations than to reproduce trends in stability and are not likely to reproduce the exact difference between armchair and zig-zag. The difference between the stabilisations is rather small with the consequence that a larger difference between armchair and zig-zag may lead to a more pronounced chirality effect of the Ostwald ripening. To illustrate this a few calculations were performed for a very strong stabilisation $\sigma_2 = 0.2$.

The model should be directly applicable for CNTs grown with the root growth mechanism, i.e., where metal atoms can diffuse on a substrate, eventhough no substrates were explicitly present in the model. This can be motivated by considering that clusters mounted on a substrate can be described by the introduction of an effective cluster radius[66]. As discussed in association with Paper I, the effective clusters have a lower curvature and can be considered to be larger than a free cluster with the same number of atoms. In the description, a part of the larger cluster is completely imaginary and can not experience any diffusion. This means that only a part of the surface area of the cluster can exchange atoms by diffusion. If this affect all clusters in the same way, i.e. all clusters have the same fraction of the surface area available for diffusion, the effect of the substrate will only correspond to an increase in the radius of all clusters. In order to verify that the same faction of the cluster surface area is available for all cluster sizes, a few MD-simulations were performed with the same method and parameters that were used in the study in Paper I. These simulations were performed at 2000K for clusters containing 50 to 900 atoms and for two scalings of the fitted Fe-Al_2O_3 adhesion. Three examples of cross sections of clusters and the corresponding effective clusters

are seen in Fig. 6.31. For the clusters in Fig. 6.31 only the part of the effective cluster that is located above the substrate is available for atomic exchange by diffusion. From simulations of several cluster sizes it can be seen that the surface fraction available for diffusion is the same for all cluster sizes. The data from these calculations are given in Fig. 6.32. For the clusters in Fig. 6.31, approximately 85% of the effective surface area of the clusters is available for diffusion. In order to obtain more quantitative results it may be necessary to modify the model, e.g., by using the effective cluster size instead of the real cluster size and by introducing complete stabilisation of the 15% of the cluster that are below the substrate. This was not analysed further since it was not considered likely to affect the qualitative results.

In the discussion below, the simulation time will be given in the dimensionless property called flow time. This takes time into account but it does also contain the diffusion coefficient. This means that it is a measure of both time and particle flow, i.e., the same flow time can be reached by having a low atomic flow during a long time or by having a large atomic flow during a short time. As the flow time is a measure of the total atomic flow, the flow time scales are very different for small and large clusters, i.e., ensembles of large clusters can stand a large flow without significant change while an ensemble with small clusters would change significantly during the same flow time. This explains the different time scales in the presented data.

6.6.1 Results

According to the theory for Ostwald ripening[196–198] the particle size distribution will reach a stable distribution, called the LSW distribution after a sufficiently long equilibration time. In order to test both the model and the numerical implementation thereof, simulations of free clusters were performed with the aim of reaching the LSW distribution. These simulations were started from Gaussian cluster size (radius) distributions containing 10000 clusters centred around 8 nm with a standard deviation of 0.1 nm. In Fig. 6.33, the size distributions of the clusters are given as functions of both the radius, r, and the relative average radius, i.e. $r/ < r >$. The LSW distribution was obtained after a flow time of approximately 4.5×10^6 (in the legend referred to as 4.5M) and the size distribution remained stable for at least flow time of another 20×10^6. Formally, the LSW distribution should remain completely stable but since the model is based on the time evolution of a finite ,and constantly decreasing, number of clusters the LSW distribution will only remain stable for a finite simulation time.

During a simulation time of approximately 25×10^6, the average cluster radius increase from approximately 8 nm to approximately 25 nm and the total number of clusters in the calculation decreased from 10000 clusters to approximately 500 clusters. The decrease in the number of clusters does also mean that the quality of the statistics decrease in time which is seen by the increased amount of noise in the curve in Fig. 6.33.

The success in reaching the LSW distribution indicates that the implementation of the method is reliable and that it may be applied to the modelling of other systems. This lead to the continuation of the study to calculations of smaller clusters attached to CNTs. Since CNTs are typically grown from clusters of similar or slightly larger diameters than the CNTs[57, 59, 60] the initial cluster size distributions had an average size equal to the CNT diameter. The initial size distributions were Gaussian and the standard deviations were small compared to the average cluster size. The number of clusters were 20000 for all calculations except for the calculations aiming at the reproduction of the LSW distribution which contained 10000 clusters (relevant only for the calculations discussed above).

If several CNT diameters or chiralities were present in the same calculation the initial cluster size distribution was created by a random process where the a cluster size was chosen from the Gaussian distribution and then attached to a CNT with a randomly chosen property, e.g., chirality. The probability of choosing the different properties was however equal for all clusters, e.g., it was equally probable to choose a zig-zag or an armchair CNT. In effect, this means that the simulation may not contain exactly the same number of zig-zag and armchair CNTs. The differences are however very small and in an ensemble of 20000 clusters the difference in number of clusters with different properties was usually less than 100 clusters. For example, the calculations with two different CNT radii (presented below) contained 20000 clusters whereof 10038 were attached to CNTs with radii 0.6 and 9962 to CNTs with radii 0.7.

The first study containing CNTs was conducted in order to compare the behaviour of cluster ensembles attached to CNTs with the identical distributions of free clusters. The size distributions of free clusters and clusters attached to the CNTs of radius $r_{CNT} = 0.5$ nm with stabilisation factor $\sigma_2 = 0.8$ after flowtimes 0 (initial), 5 and approximately 9.7 are given in Fig. 6.34. Of the initial 20000 clusters less than 500 clusters had disappeared when the size distributions in Fig. 6.34 were sampled. As expected the size distribution of the free clusters broaden in time while the size distribution of clusters attached to CNTs is more stable during the same flow time. The size distribution for the clusters attached to CNTs also exhibits a clear concentration of cluster sizes slightly above the radius of the CNT. This is in agreement with the DFT results presented in Paper V, stating clusters are stabilised by the CNTs and that they may be stable for long times at a size that is determined by the CNT radius and adhesion.

In order to understand how the Ostwald ripening of metal clusters is affected by the dimensions of the CNTs similar calculations were performed for a cluster ensemble, initially containing 20000 clusters attached to approximately equal amounts of CNTs of radius 0.6 nm and radius 0.7 nm. The size distributions of these cluster ensembles are seen in Fig. 6.35 for free clusters ($\sigma_2 = 1.0$) and for clusters with the CNT stabilisations $\sigma_2 = 0.8$ and $\sigma_2 = 0.2$. The difference between the free clusters and the clusters attached to CNTs with stabilisation $\sigma_2 = 0.8$ is merely in the timescale of the Ostwald ripening, i.e., the ripening rate is higher for the free clusters than for the stabilised clusters. When applying a stronger stabilisation ($\sigma_2 = 0.2$) the effect is more pronounced and during a simulation time of 75 no clusters had disappeared although a significant amount of the smaller free clusters had dissapeared after a flow time of 30. These results support the idea that the CNT may act as limiting factor of the Ostwald ripening and that the time scale of the Ostwald ripening is affected by the quantitative properties of the stabilisation. The latter is further supported by the results in Fig. 6.36 where an approximately equal number of clusters have been attached to CNTs with a radius of 0.5 nm but with different chirality. For these systems the clusters attached to the armchair ($\sigma_2 = 0.9$) like CNTs will decrease in size but increase in size disperion while the clusters attached to zig-zag like CNTS ($\sigma_2 = 0.8$) are more likely to increase in size.

The last set of calculations were performed for an ensemble of clusters that were attached to approximately equal amounts of CNTs of radius 0.5, 0.6 and 0.7 nm The clusters size distributions contained in total 20000 clusters and were initiated at a size that was equal to the radius of the CNT size and the standard deviation of the distribution was 0.01 nm. The calculations were performed for free clusters and for clusters attached to CNTs with two different stabilisations $\sigma_2 = 0.8$ (zig-zag like) and $\sigma_2 = 0.2$

The results of this simulation are seen in Fig. 6.37 where the CNT stabilisation is once

again seen as a limiting factor on the Ostwald ripening rate. The very strong stabilisation ($\sigma_2 = 0.2$) is also seen to lead to a narrowing of the size distributions although Ostwald ripening appears to occur, seen by the change in the average size of the initial distributions. The percentual size change is less for the larger clusters than for the smaller, i.e., clusters decreased from 0.5 nm to approximately 0.44 nm while the larger clusters increased from 0.7 nm to approximately 0.73 nm. This corresponds to a decrease in size of 12% for the smaller cluster but only an increase of 4% for the larger clusters. This difference in the precentual change could be understood from the relation

$$R_c \propto n^{1/3} \tag{6.4}$$

relating the cluster size, R_c, to the number of atoms, n of the cluster. The change in the radius as an effect of a change in the number of atoms is then given by

$$\frac{\mathrm{d}R_c}{\mathrm{d}n} \propto n^{-2/3} \tag{6.5}$$

which decreases with increasing number of atoms, i.e. the removal of a few atoms from a small cluster means a big decrease in the radius while the addition of the same number of atoms to a larger cluster means a small increase in the radius. The effect of this is that if the CNT and cluster size dispersions are large, the smaller clusters are strongly affected by Ostwald ripening while the larger clusters are hardly affected at all, i.e., the smaller CNTs are are affected by Ostwald ripening on a shorter time scale than the larger CNTs.

Another consequence may be that the if the larger clusters are in the stable size region they may remain in this region for long time eventhough the smaller clusters have completely vanished, i.e., clusters attached to large CNTs may survive the Ostwald ripening for (infinitely) long times.

Yet another implication may be that if CNTs are successfully grown from clusters with sizes 1.1 to 1.6 times the CNT diameter[60] a cluster with a too large diameter may also act limiting on the CNT growth, i.e., not only too small clusters may inhibit the CNT growth. Since the larger clusters are affected the least by the Ostwald ripening, it is reasonable that these clusters will remain in the size window 1.1 to 1.6 times the CNT diameter for longer times than the smaller clusters. Although these clusters may not be stable for infinitely long times they may still be stable for significantly longer times than the smaller clusters.

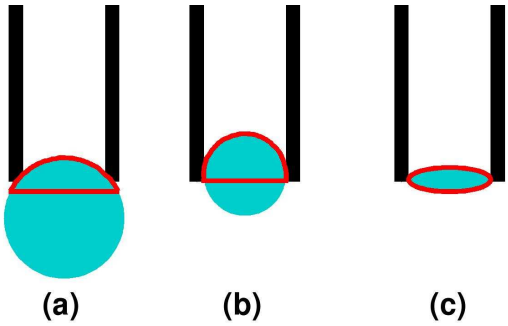

Figure 6.27: The regions of the clusters that are stabilised by the CNT are seen by the enclosed curves. The figures correspond to situations where the cluster radius is significantly larger than (a), similar to (b) and smaller than (c) the CNT radius.

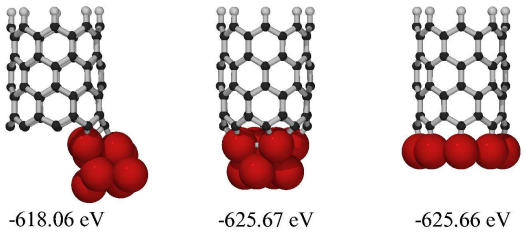

Figure 6.28: A $(8,0)$ CNT attached to 8 Ni atoms in the shape of a small cluster at the side of the CNT(left), in the centre of the CNT (middle) or as a ring (right). The total energies of centred cluster and the ring are comparable while the energy of the cluster on the side is significantly higher.

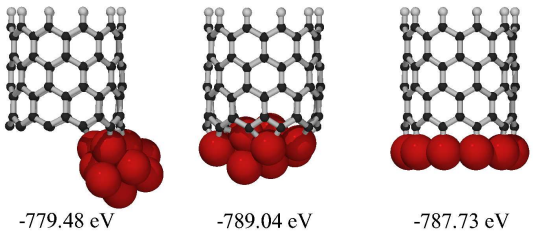

Figure 6.29: A $(10,0)$ CNT attached to 10 Ni atoms, either in the shape of a small cluster at one size of the CNT (left), in the middle of the CNT (middle) or as a ring (right). The small cluster in the middle is approximately 2 eV lower in energy than the ring.

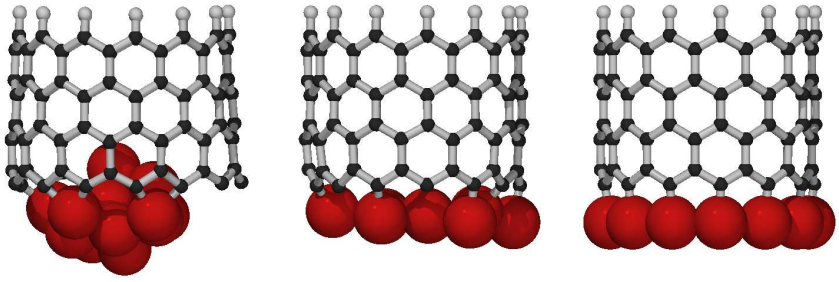

Figure 6.30: A $(13, 0)$ CNT attached to 13 Ni atoms, either in the shape of a small cluster (left), a planar "star" shaped flake (middle) or a ring (right). The ring is approximately 6 eV lower in energy than the other structures. It is reasonable that the reason for this is that the ring leaves no dangling C bonds at the CNT end.

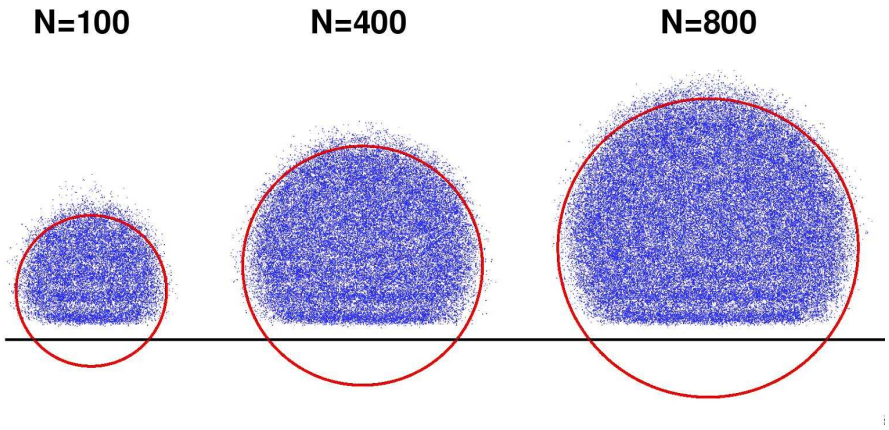

Figure 6.31: Cross sections of metal clusters on a flat substrate with the parameterised Fe-Al_2O_3 adhesion strength. The cluster sizes are 100 (left), 400 (middle) and 800 atoms (right). For all cluster sizes, approximately 85% of the effective cluster surface is above the substrate. The cross sections have been sampled over a 100 ps long MD simulation at 2000K. All sampled atoms were positioned in a sheet of thickness 1Å perpendicular to the substrate.

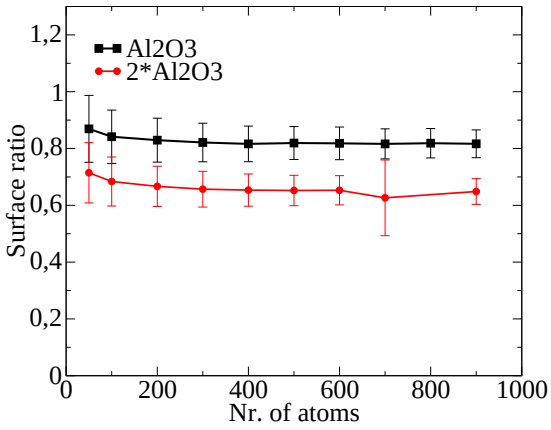

Figure 6.32: The surface fraction of the effective clusters situated above the substrate surface, i.e. the surface that is available for diffusion, is given as a function of the number of atoms in the cluster. The fractions are given for the parameterised Fe-Al_2O_3 adhesion and for a scaling of twice this adhesion strength. The data is sampled at 2000 K which means that available surface fraction varies in time with the standard deviation given in the plot. The surface fraction above the substrate surface is seen to be independent of the cluster size and, as expected, the stronger adhesion leads to a smaller surface fraction available for diffusion.

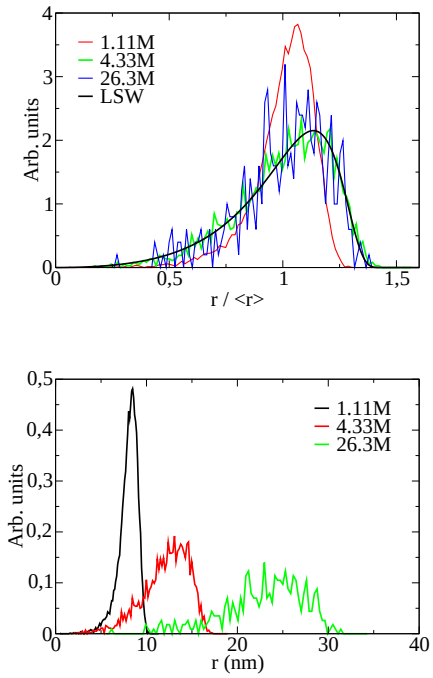

Figure 6.33: The size distributions for free clusters for tree different times of the simulations are given as functions of the relative average radius (top) and total radius (bottom). After a simulation time of approximately 4.5×10^6 (4.5M) the stationary LSW distribution was reached. A this time the average radius was approximately 11 nm.

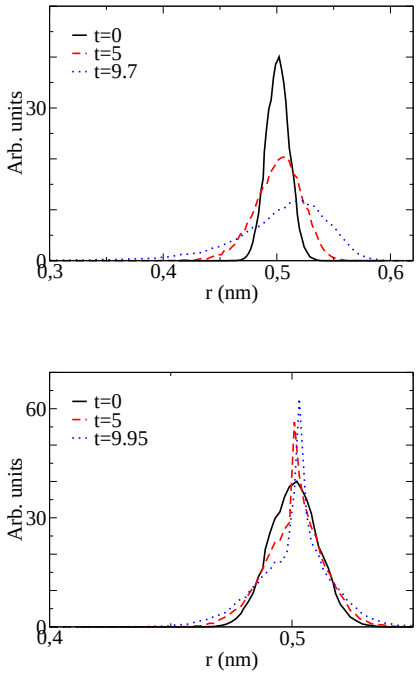

Figure 6.34: Time evolution of distributions of free (top panel) and CNT-attached (bottom panel) clusters starting from Gaussian distributions centred around 0.5 nm with a standard-deviation of 0.01 nm. The distributions are given after flow times 0 (initial), 5 and approximately 9.7.

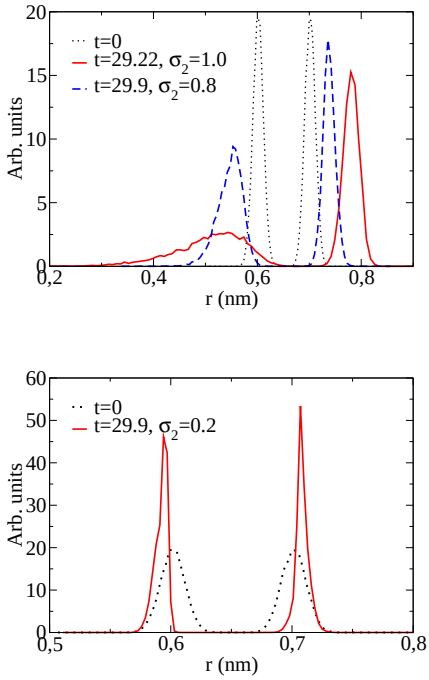

Figure 6.35: Size distributions for clusters initially centred around 0.6 nm and 0.7 nm are given after different flow times indicated by t in the legends. The clusters were either free ($\sigma_2 = 1.0$) or stabilised by CNTs with stabilisations $\sigma_2 = 0.8$ and $\sigma_2 = 0.2$ and the same radius as the average size of the initial cluster distribution, i.e., 0.6 nm and 0.7 nm for the cluster distributions, respectively. In the top panel, the initial ($t = 0$) cluster size distribution (dotted) and distributions after a flowtime of approximately 29 are given for free clusters (solid) and the size distribution of CNT stabilised clusters with $\sigma_2 = 0.8$ (dashed). The middle panel show the initial cluster size distribution (dotted) and the size distribution of CNT stabilised clusters with $\sigma_2 = 0.2$ after a flowtime of 29. The relative abundance (bottom), defined as $N_{0.6}/N_{0.7}$ is given for the free clusters (dotted), for CNT stabilisations $\sigma_2 = 0.8$ (dashed) and $\sigma_2 = 0.2$ (solid).

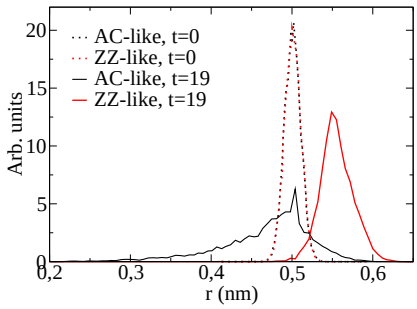

Figure 6.36: The size distributions of clusters attached to armchair like ($\sigma_2 = 0.9$) and zig-zag like ($\sigma_2 = 0.8$) CNTs with radius 0.5 nm (top). The initial distributions were Gaussian centred around 0.5 nm with a standarddeviation of 0.01 nm (dotted lines) and the number of clusters of attached to each type of CNT were approximately equal. After a flowtime of 19 the size dispersion of both cluster types have increased and the clusters attached to zig-zag like CNTs increase in size on the expense of the clusters attached to arechair like CNTs.

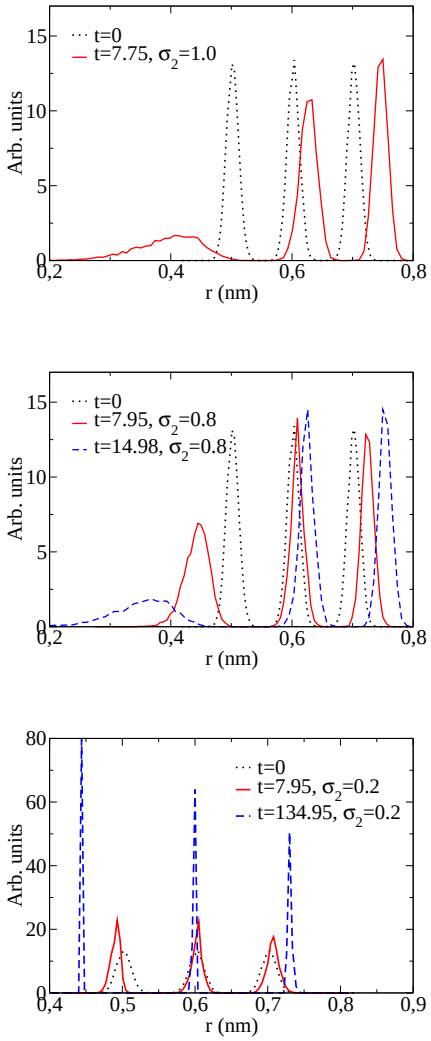

Figure 6.37: Size distributions for clusters, initially centred around 0.5 nm, 0.6 nm and 0.7 nm, given after different flow times. The clusters were either free ($\sigma_2 = 1.0$) (top) or stabilised by CNTs with stabilisation factors $\sigma_2 = 0.8$ (middle) and $\sigma_2 = 0.2$ (bottom). The flowtimes at which the distributions were sampled are given in the legends where flowtime $t = 0$ correspond to the initial distribution.

CHAPTER 7

Conclusions and Outlook

The work presented in the thesis has focussed on a number of parameters that are of importance in the search for methods of controlled growth of CNTs. The size of the systems under study has spanned from single particles to infinite CNT forests, i.e., from the single metal clusters present prior to CNT growth to the large CNT ensembles present after growth

Although the temperature during CNT growth is significantly lower than the bulk melting temperature of the metal used as catalyst these metal clusters may be liquid. This is attributed to the known size dependence of the melting temperature but also on effects induced by external parameters. For clusters mounted on a substrate both the adhesion strength between the substrate and cluster and the surface structure of the substrate were seen to affect the melting temperature. For CNT growth this means that the same catalyst metal may be either liquid or solid depending on which substrate it is mounted. This can provide a partial explanation for the observed effect of the substrate on CNT growth.

In the studies of the attachment of CNTs to metal clusters it was found that CNTs are attached above the cluster surfaces and that clusters adapt to the shape of the CNT and not *vice versa*. The effect of this is that the cluster may be geometrically deformed while the CNT will retain both shape and chirality at the end. This trend was observed irrespectively of whether the cluster was a pure metal or a metal carbide. The metal carbide systems were however less stable than the corresponding systems with pure metals although the the adhesion strength between CNTs and carbide clusters was comparable to the adhesion strength between CNTs and pure metal. This means that if the adhesion is strong enough for pure metal clusters to remain attached to the CNT it is likely that also carbide clusters remain attached to the CNTs. The lower stability of the carbide systems may however imply that the CNT drain the clusters from excess carbon atoms.

Upon variation of the the size of the metal clusters attached to the CNTs it was found that a minimum cluster size is needed to prevent the CNT ends from closing. This is a possible explanation for the observed trend that CNTs grow from cluster particles with diameters that are similar to or slightly larger than the diameters of the CNTs. From these results it could be concluded that both pure metals and metal carbides may be docked onto open CNT ends in order to achieve continued growth of CNTs as well as for the creation junctions between

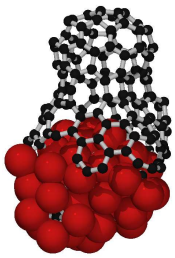

Figure 7.1: A C structure grown during a TBMC simulation at 1500 K. The simulation was started from a structure with a $(9, 1)$ CNT cap attached to a Ni_{55} cluster. The initial atomic structure is shown in association with Paper III.

CNTs and electrode materials. The exact behaviour of these systems may however depend on the size of the clusters, the carbon content and the temperature as the mere possibility of docking is not a guarantee for the successful achievement of neither continued growth nor operational contacts.

The learnings from these studies were transferred to studies of large ensembles of CNT-cluster systems. This was done in order to understand if the Ostwald ripening of the catalysts may provide any information of relevance for the controlled CNT growth. The systems under study mimicked the experimental distributions of CNTs with different diameters and chiralities attached to clusters of different size. Both the adhesion strength and the CNT diameters were seen to affect the properties of the Ostwald ripening of the clusters. It was predicted that clusters attached to CNTs of large diameters and strong CNT-cluster adhesion are most likely to survive Ostwald ripening. This means that these CNTs should have a longer growth time than other CNTs although introduction of radicals in the growth chamber may impose radical changes to the trends.

Finally, a simple phenomenological model for simulations of the Ostwald ripening in cluster ensembles was constructed. The model reproduced the stationary LSW distribution describing Ostwald ripening as well as the qualitative trends of the DFT calculations for nano clusters attached to CNTs. The model did also allow for predictions of the long time behaviour of the CNT-cluster distributions after Ostwald ripening.

Although these studies have provided information that take the CNT community a few steps further towards the controlled CNT growth much work is likely to remain before this becomes reality. The next study to be performed within the project will address the stability of C atoms on the surface of metal clusters. Hopefully this study can provide information about both the formation of the CNT cap and the mechanisms during CNT growth. This study is most likely to be conducted with DFT and TBMC calculations in a combination that will allow for high accuracy, flexibility, finite temperature and hopefully simulated CNT growth. The structure in Fig. 7.1, showing a CNT that has continued growth from an existing seed CNT, indicate that the latter may become reality in the "near" future. Preliminary results indicate that C atoms are more stable when forming strings on the cluster surface compared to attaching to the cluster surface as monomers. Hence, the early formation of strings and polygon structures on the cluster surface appears to be more likely than random positioning of C atoms on the surface. Another indication is that C atoms in the middle of the strings may detach from the surface which may be important for the rejection of the cluster from the CNT end. It may also limit the maximum allowed length of the chains before soot is formed

instead of CNTs.

Acknowledgements

The work I have presented in the thesis would not be without the support from a number of people.

First of all I would like thank my supervisor Prof. Kim Bolton for accepting me as a student and for all his encouragement and support along the way.

I am also grateful for the help from Dr. Wuming Zhu and Dr. Haiming Duan who contributed with discussions and practical help with the early calculations. Also Dr. Hakim Amara and Dr. Christophe Bichara deserve a special thanks for sharing both their tight-bindig code and their knowledge about the code and science in general.

The staff at the School of Engineering, University of Borås and at the Department of Physics, University of Gothenburg are acknowledged for their contributions in areas, spanning from nice conversations, help with course work and teaching to practical help with technical and administrative tasks.

I am thankful for all the support from my family. Especially my wife Matilda who has been very patient and supportive during the hard times of this work. Vera is acknowledged for reminding me that time spent on sleeping is wasted.

I am grateful for the financial support obtained from the Swedish Research Council and the University of Gothenburg Nanoparticle Platform and for the computer time allocated at the C^{3}SE, NSC and UPPMAX computing facilities.

Bibliography

[1] Encyclopaedia Britannica. Carbon - encyclopaedia britannica online, 2010. Web. 4 May 2010.

[2] Encyclopaedia Britannica. Steel - encyclopaedia britannica online, 2010. Web. 4 May 2010.

[3] E. H. L. Falcao and F. Wudl. *J. Chem. Technol. Biotechnol.*, 82:524, 2007.

[4] H. W. Kroto, J. R. Heath, S. C. O'Brien, R. F. Curl, and R. E. Smalley. *Nature*, 318:162, 1985.

[5] S. Iijima. *Nature*, 354:56, 1991.

[6] K. S. Novoselov, A. K. Geim, S. V. Morozov, D. Jiang, Y. Zhang, S. V. Dubonos, I. V. Grigorieva, and A. A. Firsov. Electric Field Effect in Atomically Thin Carbon Films. *Science*, 306(5696):666–669, 2004.

[7] C. T. White, D. H. Robertson, and J. W. Mintmire. Helical and rotational symmetries of nanoscale graphitic tubules. *Phys. Rev. B*, 47(9):5485–5488, Mar 1993.

[8] T. Hayashi, Y. A. Kim, T. Matoba, M. Esaka, K. Nishimura, T. Tsukada, M. Endo, and M. S. Dresselhaus. *Nano Letters*, 3:887–889, 2003.

[9] R. Jasti, J. Bhattacharjee, J. B. Neaton, and C. R. Bertozzi. *J. Am. Chem. Soc.*, 130:17646–17647, 2008.

[10] X. Wang, Q. Li, J. Xie, Z. Jin, J. Wand, Y. Li, K. Jiand, and S. Fan. *Nano Letters*, 9:3137–3141, 2009.

[11] M. M. J. Treacy, T. W. Ebbesen, and J. M. Gibson. *Nature*, 381:678, 1996.

[12] S. Bellucci. *Physica Status Solidi (c)*, 2:34, 2004.

[13] Min-Feng Yu, Oleg Lourie, Mark J. Dyer, Katerina Moloni, Thomas F. Kelly, and Rodney S. Ruoff. Strength and Breaking Mechanism of Multiwalled Carbon Nanotubes Under Tensile Load. *Science*, 287(5453):637–640, 2000.

[14] S. Chwastiak, J.B. Barr, and R. Didchenko. High strength carbon fibers from mesophase pitch. *Carbon*, 17(1):49 – 53, 1979.

[15] F. Li, H. M. Cheng, S. Bai, G. Su, and M. S. Dresselhaus. Tensile strength of single-walled carbon nanotubes directly measured from their macroscopic ropes. *Applied Physics Letters*, 77(20):3161–3163, 2000.

[16] Y. Yao, C. Liu, and S. Fan. *Nanotechnology*, 17:4374–4378, 2006.

[17] Evans Cycles. Web. 13 September 2010.

[18] CheapTubes Inc. Web. 5 May 2010.

[19] A. E. Porter, M. Gass, K. Muller, J. N. Skepper, P. A. Midgley, and M. Welland. *Nature Nanotechnology*, 2:713–717, 2007.

[20] C. A. Poland, R. Duffin, I. Kinlich, A. Maynard, W. A. H. Wallace, A. Seaton, V. Stone, S. Brown adn W. MacNee, and K. Donaldson. *Nature Nanotechnology*, 3:423–428, 2008.

[21] M. S. Dresselhaus, G. Dresselhaus, and P. Avouris. *Carbon Nanotubes: Synthesis, Structure, Properties and Applications*. Springer, Berlin, 2001.

[22] S. Reich, C. Thomsen, and J. Maultzch. *Carbon Nanotubes: Basic Concepts and Physical Properties*. Wiley-VCH, Weinheim, 2004.

[23] Noriaki Hamada, Shin-ichi Sawada, and Atsushi Oshiyama. New one-dimensional conductors: Graphitic microtubules. *Phys. Rev. Lett.*, 68(10):1579–1581, Mar 1992.

[24] R. Saito, M. Fujita, G. Dresselhaus, and M. S Dresselhaus. Electronic structure of chiral graphene tubules. *Applied Physics Letters*, 60(18):2204–2206, 1992.

[25] M. P. Anantram and F. Leonard. *Rep. Prog. Phys.*, 69:507, 2006.

[26] P. Avouris, Z. Chen, and Vasili Perebeinos. *Nature Nanotechnology*, 2:605, 2007.

[27] R. M. Martin. *Electronic Structure, Basic theory and practical methods*. Cambridge University Press, 2004.

[28] J. M. Thijssen. *Computational Physics*. Cambridge University Press, 2007.

[29] S. Reich, J. Maultzsch, C. Thomsen, and P. Ordejón. Tight-binding description of graphene. *Phys. Rev. B*, 66(3):035412, Jul 2002.

[30] I. Cabria, J. W. Mintmire, and C. T. White. Metallic and semiconducting narrow carbon nanotubes. *Phys. Rev. B*, 67(12):121406, Mar 2003.

[31] S. Reich, C. Thomsen, and P. Ordejón. Electronic band structure of isolated and bundled carbon nanotubes. *Phys. Rev. B*, 65(15):155411, Mar 2002.

[32] S. Hong and S. Myung. *Nature Nanotechnology*, 2:207–208, 2007.

[33] K. Bladh, L. K. L. Falk, and F. Rohmund. *Appl. Phys. A*, 70:317, 2000.

[34] J. Kong, H. T. Soh, A. M. Cassell, C. F. Quate, and H. Dai. *Nature*, 395:878, 1998.

[35] C. Ducati, I. Alexandrou, M. Chhowalla, G. A. J. Amaratunga, and J. Robertson. *Journal of Applied Physics*, 92:3299, 2002.

[36] A. R. Harutyunyan, B. K. Pradhan, U. J. Kim, G. Chen, and P. C. Eklund. *Nano Letters*, 2:525, 2002.

[37] D. B. Geohegan, A. A. Puretzky, I. N. Ivanov, S. Jesse, G. Eres, and J. Y. Howe. *Applied Physics Letters*, 83:1851, 2003.

[38] M. Kumar and Y. Ando. *Journal of Nanoscience and Nanotechnology*, 10:3739–3750, 2010.

[39] F. Ding, K. Bolton, and A. Rosén. *J. Phys. Chem. B*, 108:17369–17377, 2004.

[40] Jian-Tao Wang, Changfeng Chen, Kaoru Ohno, Enge Wang, Xiao Long Chen, Ding-Sheng Wang, Hiroshi Mizuseki, and Yoshiyuki Kawazoe. Atomistic nucleation and growth mechanism for single-wall carbon nanotu bes on catalytic nanoparticle surfaces. *Nanotechnology*, 21(11):115602, 2010.

[41] J. Kong, A. M. Cassell, and H. Dai. *Chemical Physics Letters*, 292:567, 1998.

[42] J. Li, C. Papadopoulos, J. M. Xu, and M. Moskovits. Highly-ordered carbon nanotube arrays for electronics applications. *Applied Physics Letters*, 75(3):367–369, 1999.

[43] J.S. Lee, G.H. Gu, H. Kim, K.S. Jeong, J. Bae, and J.S. Suh. Growth of carbon nanotubes on anodic aluminum oxide templates: Fabrication of a tube-in-tube and linearly joined tube. *Chemistry of Materials*, 13(7):2387–2391, 2001.

[44] Y. Yun, V. Shanov, Y. Tu, S. Subramaniam, and M.J. Schulz. Growth mechanism of long aligned multiwall carbon nanotube arrays by water-assisted chemical vapor deposition. *Journal of Physical Chemistry B*, 110(47):23920–23925, 2006.

[45] F. Ding, A. Rosen, E. E. B. Campbell, L. K. L. Falk, , and K. Bolton. *J. Phys. Chem. B*, 110:7666–7670, 2006.

[46] S K Pal, S Talapatra, S Kar, L Ci, R Vajtai, T Borca-Tasciuc, L S Schadler, and P M Ajayan. Time and temperature dependence of multi-walled carbon nanotube growth on inconel 600. *Nanotechnology*, 19(4):045610, 2008.

[47] M Meyyappan, Lance Delzeit, Alan Cassell, and David Hash. Carbon nanotube growth by pecvd: a review. *Plasma Sources Science and Technology*, 12(2):205, 2003.

[48] Limin Huang, Xiaodong Cui, Brian White, , and Stephen P. O'Brien. *Journal of Physical Chemistry B*, 108:16451–16456, 2004.

[49] O. A. Nerushev, S. Dittmar, R.-E. Morjan, F. Rohmund, and E. E. B. Campbell. Particle size dependence and model for iron-catalyzed growth of carbon nanotubes by thermal chemical vapor deposition. *Journal of Applied Physics*, 93(7):4185–4190, 2003.

[50] Morjan R.E., O.A. Nerushev, M. Sveningsson, F. Rohmund, L.K.L. Falk, and E.E.B. Campbell. *Applied Physics A*, 78:253–261, 2004.

[51] D. Takagi, Y. Homma, H. Hibino, S. Suzuki, and Y. Kobayashi. *Nano Letters*, 6:2642, 2006.

[52] W. Zhou, Z. Han, J. Wang, Y. Zhang, Z. Jin, X. Sun, Y. Zhang, C. Yan, and Y. Li. *Nano Letters*, 6:2987, 2006.

[53] D. Takagi, H. Hibino, S. Suzuki, Y. Kobayashi, and Y. Homma. *Nano Letters*, 7:2272, 2007.

[54] F. Ding, P. Larsson, J.A. Larsson, R. Ahuja, H. Duan, A. Rosen, and K. Bolton. The importance of strong carbon-metal adhesion for catalytic nucleation of single-walled carbon nanotubes. *Nano Letters*, 8(2):463–468, 2008.

[55] H. Dai, A. G. Rinzler, P. Nikolaev, D. T. Colbert A. Thess, and R. E. Smalley. *Chemical Physics Letters*, 260:471, 1996.

[56] Y. Li, W. Kim, Y. Zhang, M. Rolandi, D. Wang, and H. Dai. Growth of single-walled carbon nanotubes from discrete catalytic nanoparticles of various sizes. *Journal of Physical Chemistry B*, 105(46):11424–11431, 2001.

[57] C.L. Cheung, A. Kurtz, H. Park, and C.M. Lieber. Diameter-controlled synthesis of carbon nanotubes. *Journal of Physical Chemistry B*, 106(10):2429–2433, 2002.

[58] D. Ciuparu, Y. Chen, S. Lim, G.L. Haller, and L. Pfefferle. Uniform-diameter single-walled carbon nanotubes catalytically grown in cobalt-incorporated mcm-41. *Journal of Physical Chemistry B*, 108(2):503–507, 2004.

[59] A. G. Nasibulin, A. Moisala, D. P. Brown, H. Jiang, and E. I. Kauppinen. *Chemical Physics Letters*, 402:227, 2005,.

[60] A. G. Nasibulin, P. V. Pikhitsa, H. Jiang, and E. I. Kauppinen. *Carbon*, 43:2251, 2005.

[61] S. Hofmann, G. Csányi, A. C. Ferrari, M. C. Payne, and J. Robertson. *Physical Review Letters*, 95:036101, 2005.

[62] M. Chhowalla, K. B. K. Teo, C. Ducati, N. L. Rupesinghe, G. A. J. Amaratunga, A. C. Ferrari, D. Roy, and J. Robertsin anbd W. I. Milne. *J. Appl. Phys.*, 90:5308 – 5317, 2001.

[63] S. Hoffman, G. Csányi, A. C. Ferrari, M. C. Payne, and J. Robertson. *Phys. Rev. Lett.*, 95:036101, 2005.

[64] A. R. Harutyunyan, T. Tokune, and E. Mora. *Applied Physics Letters*, 87:051919, 2005.

[65] S.-C. Lee, N. M. Hwang, B. D. Yu, and D.-Y. Kim. *Journal of Crystal Growth*, 223:311, 2001.

[66] F. Ding, A. Rosén, S. Curtarolo, and K. Bolton. *Applied Physics Letters*, 88:133110, 2006.

[67] C.-L. Kuo and P. Clancy. *J. Phys. Chem. B*, 109:13743, 2005.

[68] A. Antonelli, S. N. Khanna, and P. Jena. *Physical Review B*, 48:8263, 1993.

[69] Y. Shibuta and S. Maruyama. *Chemical Physics Letters*, 437:218, 2007.

[70] A. Jiang, N. Awasthi, A. N. Kolmogorov, W. Setyawan, A. Börjesson, K. Bolton, A. R. Harutyunyan, and S. Curtarolo. *Phys. Rev. B*, 75:205426, 2007.

[71] C. Mottet and J. Goniakowski. *Surface Science*, 566:443, 2004.

[72] S. Bhaviripudi, E. Mile, S. A. Steiner III, A. T. Zare, M. S. Dresselhaus, A. M. Belcher, and J. Kong. *J. Am. Chem. Soc.*, 129:1516, 2007.

[73] S. M. Bachilo, L. Balzano, J. E. Herrera, F. Pompeo, D. E. Resasco, and R. B. Weisman. *J. Am. Chem. Soc.*, 125:11186, 2003.

[74] P. B. Amama, C. L. Pint, L. McJilton, S. M. Kim, E. A. Stach, P. T. Murray, R. H. Hauge, and B. Maruyama. *Nano Letters*, 9:44 – 49, 2009.

[75] S. M. Kim, C. L. Pint, P. B. Amama, D. N. Zakharov, R. H. Hauge, B. Maruyama, and E. A. Stach. *Phys. Chem. Lett.*, 1:918 – 922, 2010.

[76] P. B. Amama, C. L. Pint, S. M. Kim, L. McJilton, K. G. Eyink, E. A. Stach, R. H. Hauge, and B. Maruyama. *ACS Nano*, 4:895 – 904, 2010.

[77] Kenji Hata, Don N. Futaba, Kohei Mizuno, Tatsunori Namai, Motoo Yumura, and Sumio Iijima. Water-Assisted Highly Efficient Synthesis of Impurity-Free Single-Walled Carbon Nanotubes. *Science*, 306(5700):1362–1364, 2004.

[78] N. Yoshihara, H. Ago, and M. Tsuji. *J. Phys. Chem. C*, 111:11577 – 11582, 2007.

[79] G. Lolli, L. Zhang, L. Balzano, N. Sakulchaicharoen, Y. Tan, and D. E. Resasco. *J. Phys. Chem. B*, 110:2108, 2006.

[80] R. Krupke, F. Hennrich, H. V. Lohneysen, and M. M. Kappes. *Science*, 301:344, 2003.

[81] M. Zheng, A. Jagota, E. D. Semke, B. A. Diner, R. S. Mclean, S. R. Lustig, R. E. Richardson, and N. G. Tassi. *Nature Materials*, 2:338, 2003.

[82] Z. Chen, X. Du, M.-H. Du, C. D. Rancken, H.-P. Cheng, and A. G. Rinzler. *Nano Letters*, 3:1245, 2003.

[83] X. Li, X. Tu, S. Zaric, K. Welsher, W. S. Seo, W. Zhao, and H. Dai. *J. Am. Chem. Soc.*, 129:15770, 2007.

[84] Y. H. Wang, M. J. Kim, H. Shan, C. Kittrell, H. Fan, L. Ericson, W.-F. Hwang, S. Arepalli, R. H. Hauge, and R. E. Smalley. *Nano Letters*, 5:997, 2005.

[85] Donald W Brenner, Olga A Shenderova, Judith A Harrison, Steven J Stuart, Boris Ni, and Susan B Sinnott. A second-generation reactive empirical bond order (rebo) potential energy expression for hydrocarbons. *Journal of Physics: Condensed Matter*, 14(4):783–802, 2002.

[86] A.C.T. van Duin, S. Dasgupta, F. Lorant, and W.A. Goddard. Reaxff: A reactive force field for hydrocarbons. *Journal of Physical Chemistry A*, 105(41):9396–9409, 2001.

[87] P. P. Boyle. *Journal of Financial Economics*, 4:323, 1977.

[88] G. Perec. *Livet, en bruksanvisning.* Delfinserien, 2000.

[89] Kazuyoshi Tanaka, Kenji Okahara, Mayumi Okada, and Tokio Yamabe. Electronic properties of bucky-tube model. *Chemical Physics Letters*, 191(5):469 – 472, 1992.

[90] J. W. Mintmire, B. I. Dunlap, and C. T. White. Are fullerene tubules metallic? *Phys. Rev. Lett.*, 68(5):631–634, Feb 1992.

[91] J.-C. Charlier and J.-P. Michenaud. Energetics of multilayered carbon tubules. *Phys. Rev. Lett.*, 70(12):1858–1861, Mar 1993.

[92] J.-C. Charlier, X. Gonze, and J.-P. Michenaud. First-principles study of carbon nanotube solid-state packings. *EPL (Europhysics Letters)*, 29(1):43, 1995.

[93] D. H. Robertson, D. W. Brenner, and J. W. Mintmire. Energetics of nanoscale graphitic tubules. *Phys. Rev. B*, 45(21):12592–12595, Jun 1992.

[94] Sumio Iijima, Charles Brabec, Amitesh Maiti, and Jerzy Bernholc. Structural flexibility of carbon nanotubes. *The Journal of Chemical Physics*, 104(5):2089–2092, 1996.

[95] B. I. Yakobson, C. J. Brabec, and J. Bernholc. Nanomechanics of carbon tubes: Instabilities beyond linear response. *Phys. Rev. Lett.*, 76(14):2511–2514, Apr 1996.

[96] Guoxin Cao and Xi Chen. Buckling of single-walled carbon nanotubes upon bending: Molecular dynamics simulations and finite element method. *Phys. Rev. B*, 73(15):155435, Apr 2006.

[97] Marco Buongiorno Nardelli, B. I. Yakobson, and J. Bernholc. Mechanism of strain release in carbon nanotubes. *Phys. Rev. B*, 57(8):R4277–R4280, Feb 1998.

[98] K. M. Liew, X. Q. He, and C. H. Wong. On the study of elastic and plastic properties of multi-walled carbon nanotubes under axial tension using molecular dynamics simulation. *Acta Materialia*, 52(9):2521 – 2527, 2004.

[99] Yu. I. Prylutskyy, S. S. Durov, O. V. Ogloblya, E. V. Buzaneva, and P. Scharff. Molecular dynamics simulation of mechanical, vibrational and electronic properties of carbon nanotubes. *Computational Materials Science*, 17(2-4):352 – 355, 2000.

[100] Guanghua Gao, Tahir Çagin, and William A Goddard III. Energetics, structure, mechanical and vibrational properties of single-walled carbon nanotubes. *Nanotechnology*, 9(3):184, 1998.

[101] I. Jang, S. B. Sinnot, D. Danailov, and P. Keblinski. *Nano Letters*, 4:109–114, 2004.

[102] Madhu Menon and Deepak Srivastava. Carbon nanotube "t junctions": Nanoscale metal-semiconductor-metal contact devices. *Phys. Rev. Lett.*, 79(22):4453–4456, Dec 1997.

[103] L. Chico, Vincent H. Crespi, Lorin X. Benedict, Steven G. Louie, and Marvin L. Cohen. Pure carbon nanoscale devices: Nanotube heterojunctions. *Phys. Rev. Lett.*, 76(6):971–974, Feb 1996.

[104] J.-C. Charlier. *Acc. Chem. Res.*, 35:1063–1069, 2002.

[105] San-Huang Ke, Harold U. Baranger, and Weitao Yang. Contact transparency of nanotube-molecule-nanotube junctions. *Phys. Rev. Lett.*, 99(14):146802, Oct 2007.

[106] V. Vitale, A. Curioni, and W. Andreoni. *J. AM. CHEM. SOC.*, 130:5848, 2008.

[107] Antonis N. Andriotis and Madhu Menon. Structural and conducting properties of metal carbon-nanotube contacts: Extended molecule approximation. *Phys. Rev. B*, 76(4):045412, Jul 2007.

[108] Y. Matsuda, W.-Q. Deng, , and W. A. Goddard III. *J. Phys. Chem. C*, 111:11113–11116, 2007.

[109] Jeong Won Kang and Ho Jung Hwang. Nanoscale carbon nanotube motor schematics and simulations for micro-electro-mechanical machines. *Nanotechnology*, 15(11):1633, 2004.

[110] Deepak Srivastava. A phenomenological model of the rotation dynamics of carbon nanotube gears with laser electric fields. *Nanotechnology*, 8(4):186, 1997.

[111] Al Globus, Charles W Bauschlicher Jr, Jie Han, Richard L Jaffe, Creon Levit, and Deepak Srivastava. Machine phase fullerene nanotechnology. *Nanotechnology*, 9(3):192, 1998.

[112] Carbon nanotubes: properties and application. *Materials Science and Engineering: R: Reports*, 43(3):61 – 102, 2004.

[113] P. Pawlow. *Z. Phys. Chem.*, 65:545, 1909.

[114] Ph. Buffat and J-P. Borel. *Physical Review A*, 13:2287, 1976.

[115] T. Castro, R. Reifenberger, E. Choi, and R. P. Andres. *Physical Review B*, 42:8548, 1990.

[116] E. Z. Luo, Q. Cai, W. F. Chung, and M. S. Altman. *Applied Surface Science*, 92:331, 1996.

[117] S. L. Lai, J. Y. Guo, V. Petrova, G. Ramanath, and L. H. Allen. *Physical Review Letters*, 77:99, 1996.

[118] M. Schmidt, R. Kusche, W. Kronmuller, B. von Issendorff, and H. Haberland. *Physical Review Letters*, 79:99, 1997.

[119] H. Haberland, T. Hippler, J. Donges, O. Kostko, M. Schmidt, and B. von Issendorff. *Physical Review Letters*, 94:035701, 2005.

[120] F. Ercolessi, W. Andreoni, and E. Tosatti. *Physical Review Letters*, 66:911, 1991.

[121] F. Calvo and F. Spiegelmann. *Journal of Chemical Physics*, 112:2888, 2000.

[122] C. L. Cleveland, W. D. Luedtke, and U. Landman. *Physical Review B*, 60:5065, 1999.

[123] S. Valkealahti and M. Manninen. *Computational Materials Science*, 1:123, 1993.

[124] L. J. Lewis, P. Jensen, and J-L. Barrat. *Physical Review B*, 56:2248, 1997.

[125] Y. Teng, X. Zeng, H. Zhang, and D. Sun. *Journal of Physical Chemistry B*, 111:2309, 2007.

[126] T. X. Li, Y. L. Ji, S. W. Su, and G. H. Wang. *Solid State Communications*, 116:547, 2000.

[127] H. Duan, F. Ding, A. Rośen, A. R. Harutyunyan, S. Curtarolo, and K. Bolton. *Chemical Physics*, 333:57, 2007.

[128] F. Ding, K. Bolton, and A. Rosén. *Eur. Phys. J. D*, 34:275, 2005.

[129] Yue Qi, Tahir Cagin, William L. Johnson, and William A. Goddard I II. Melting and crystallization in ni nanoclusters: The mesoscale regime. *The Journal of Chemical Physics*, 115(1):385–394, 2001.

[130] R. Radhakrishnan, K. E. Gubbins, and M. Sliwinska-Bartolowiak. 2002.

[131] N. Quirke and Ping Sheng. The melting behavior of small clusters of atoms. *Chemical Physics Letters*, 110(1):63 – 66, 1984.

[132] S. C. Hendy. *Nanotechnology*, 18:175703, 2007.

[133] Yanting Wang, S. Teitel, and Christoph Dellago. Melting of icosahedral gold nanoclusters from molecular dynamics simulations. *The Journal of Chemical Physics*, 122(21):214722, 2005.

[134] F. Ding, K. Bolton, and A. Rosén. *J. Vac. Sci. Technol. A*, 22:1471, 2004.

[135] F. Ablid-Pedersen, J. K. Nørskow, J. R. Rostrup-Nielsen, J. Sehested, and S. Helveg. *Physical Review B*, 73:115419, 2006.

[136] E. Mora, J. M. Pigos, F. Ding, B. I. Yakobson, and A. R. Harutyunyan. *J. Am. Chem. Soc.*, 130:11840–11841, 2008.

[137] Q.-M. Zhang, J. C. Wells, X. G. Gong, and Z. Y. Zhang. *Physical Review B*, 69:205413, 2004.

[138] J. Gavillet, A. Loiseau, C. Journet, F. Williame, F. Ducastelle, and J.-C. Charlier. *Physical Review Letters*, 87:275504, 2001.

[139] D. E. Jiang and Emily A. Carter. Carbon atom adsorption on and diffusion into fe(110) and fe(100) from first principles. *Phys. Rev. B*, 71(4):045402, Jan 2005.

[140] O. V. Yazyev and A. Pasquarello. *Physical Review Letters*, 100:156102, 2008.

[141] F. Cinquini, F. Delbecq, and P. Sautet. *Phys. Chem. Chem. Phys.*, 11:11546–11556, 2009.

[142] X. Fan, R. Buczko, A. A. Puretzky, D. B. Geohegan, J. Y. Howe, S. T. Pantelides, and S. J. Pennycook. *Physical Review Letters*, 90:145501, 2003.

[143] S. Reich, L. Li, and J. Robertson. *Chemical Physics Letters*, 421:469, 2006.

[144] P. Larsson, J. A. Larsson, R. Ahuja, F. Ding, B. I. Yakobson, H. Duan, A. Rosén, and K. Bolton. *Physical Review B*, 75:115419, 2007.

[145] S. Reich, L. Li, and J. Robertson. Structure and formation energy of carbon nanotube caps. *Physical Review B (Condensed Matter and Materials Physics)*, 72(16):165423, 2005.

[146] G. Brinkmann, P. W. Fowler, D. E. Manolopoulos, and A. H. R. Palser. A census of nanotube caps. *Chemical Physics Letters*, 315(5-6):335 – 347, 1999.

[147] Morgana A. Ribas, Feng Ding, Perla B. Balbuena, and Boris I. Yakobson. Nanotube nucleation versus carbon-catalyst adhesion–probed by molecular dynamics simulations. *The Journal of Chemical Physics*, 131(22):224501, 2009.

[148] Z. Li, J. A. Larsson, P. Larsson, R. Ahuja, J. M. Tobin, J. O'Byrne, M. A. Morris, G. Attard, and J. D. Holmes. *J. Phys. Chem. C*, 112:12201–12206, 2008.

[149] J. P. O'Byrne, Z. Li, J. M. Tobin, J. A. Larsson, P. Larsson, R. Ahuja, and J. D. Holmes. *J. Phys. Chem. C*, 114:8115–8119, 2010.

[150] Feng Ding, Avetik R. Harutyunyan, and Boris I. Yakobson. Dislocation theory of chirality-controlled nanotube growth. *Proceedings of the National Academy of Sciences*, 106(8):2506–2509, 2009.

[151] Stephan Irle, Yasuhito Ohta, Yoshiko Okamoto, Alister J. Page, Ying Wang, and Keiji Morokuma. *Nano Research*, 2:755–767, 2009.

[152] Y. Shibuta and S. Maruyama. *Comp. Mat. Sci.*, 39:842 – 848, 2007.

[153] F. Ding and K. Bolton. *Nanotechnology*, 17:543, 2006.

[154] A. Martinez-Limia and j. Zhaoand P. B. Balbuena. *Journal of molecular modelling*, 13:595, 2007.

[155] Yasushi Shibuta and Shigeo Maruyama. Molecular dynamics simulation of formation process of single-walled carbon nanotubes by ccvd method. *Chemical Physics Letters*, 382(3-4):381 – 386, 2003.

[156] Perla B. Balbuena. Role of the catalyst in the growth of single-wall carbon nanotubes. *Journal of Nanoscience and Nanotechnology*, 6:1247–1258(12), May 2006.

[157] H. Amara, C. Bichara, and F. Ducastelle. *Physical Review Letters*, 100:056105, 2008.

[158] Y. Ohta, Y. Okamoto, S. Irle, and K. Morokuma. *ACS Nano*, 2:1437–1444, 2008.

[159] Y. Ohta, Y. Okamoto, S. Irle, and K. Morokuma. *J. Phys. Chem. C*, 113:159–169, 2009.

[160] Yasuhito Ohta, Yoshiko Okamoto, Stephan Irle, and Keiji Morokuma. Single-walled carbon nanotube growth from a cap fragment on an iron nanoparticle: Density-functional tight-binding molecular dynamics simulations. *Phys. Rev. B*, 79(19):195415, May 2009.

[161] A. J. Page, S. Irle, and K. Morokuma. *J. Phys. Chem. C*, 114:8206–8211, 2010.

[162] J. Gaviellet, A. Loiseau, C. Journet, F. Williame, F. Ducastelle, and J.-C. Charlier. *Physical Review Letters*, 87:275504, 2001.

[163] J.-Y. Raty, F. Gygi, and G. Galli. *Physical Review Letters*, 95:096103, 2005.

[164] H. Fehske, R. Schneider, and A. Weiße, editors. *Computational Many-Particle Physics*. Springer-Verlag, Berlin Heidelberg, 2008.

[165] R. P. Gupta. *Physical Review B*, 23:6265, 1981.

[166] F. Ercolessi and J. B. Adams. Interatomic potentials from first-principles calculations: The force-matching method. *EPL (Europhysics Letters)*, 26(8):583–588, 1994.

[167] J. Zhao, A. Martinez-Limia, and P. B. Balbuena. *Nanotechnology*, 16:575, 2005.

[168] I. L. Garzón, K. Michaelian, M. R. Beltrán, A. Posada-Amarillas, P. Ordejón, and E. Artacho. *Physical Review Letters*, 81:1600, 1998.

[169] A. Posada-Amarillas and I. L. Garzón. *Physical Review B*, 54:10362, 1996.

[170] I. L. Garzón and A. Posada-Amarillas. *Physical Review B*, 54:11796, 1996.

[171] K. Michaelian and N. Rendón andI. L. Garzón. *Physical Review B*, 54:11796, 1996.

[172] F. Ding, A. Rosén, and K. Bolton. *Physical Review B*, 70:075416, 2004.

[173] H. Amara, J.-M. Roussel, C. Bichara, J.-P. Gaspard, and F. Ducastelle. Tight-binding potential for atomistic simulations of carbon interacting with transition metals: Application to the ni-c system. *Phys. Rev. B*, 79(1):014109, Jan 2009.

[174] H. Amara, C. Bichara, and F. Ducastelle. *Physical Review B*, 73:113404, 2006.

[175] J. Kohanoff. *Electronic Structure Calculations for Solids and Molecules*. Cambridge University Press, 2006.

[176] J. C. Slater and G. F. Koster. *Phys. Rev.*, 94:1498, 1954.

[177] D. G. Pettifor. *Bonding and Structure of Molecules and Solids*. Oxford University Press, 1995.

[178] A. P. Sutton. *Electronic Structure of Materials*. Oxford University Press, 1993.

[179] C. H. Xu, C. Z. Wang, C. T Chan, and K. M. Ho. *J. Phys: Condensed Matter.*, 4:6047, 1992.

[180] G. Kresse and J. Furthmüller. *Phys. Rev. B*, 54:11169, 1996.

[181] J. P. Perdew, J. A. Chevary, S. H. Vosko, K. A. Jackson, M. R. Pederson, D. J. Singh, and C. Fiolhais. *Phys. Rev. B*, 46:6671, 1992.

[182] D. S. Sholl and J. A. Steckel. *Density functional theory : a practical introduction*. Wiley, 2009.

[183] Georg Kresse, Martijn Marsman, and Jürgen Furthmüller. Web. 5 May 2010.

[184] John P. Perdew, Kieron Burke, and Matthias Ernzerhof. Generalized gradient approximation made simple. *Phys. Rev. Lett.*, 77(18):3865–3868, Oct 1996.

[185] Wuming Zhu, Anders Borjesson, and Kim Bolton. Dft and tight binding monte carlo calculations related to single-walled carbon nanotube nucleation and growth. *Carbon*, In Press, Accepted Manuscript:–, 2009.

[186] D. Frenkel and B. Smit. *Understanding Molecular Simulation*. Oxford University Press, 1997.

[187] M. P. Allen and D. J. Tildesley. *Computer Simulation of Liquids*. Oxford University Press, 1997.

[188] R. J. Sadus. *Molecular Simulation of Fluids*. Elsevier Science B.V., 1999.

[189] H. J. C. Berendsen. *Simulating the Physical World*. Cambridge University Press, 2007.

[190] A. R. Leach. *Molecular Modelling, Principles and Applications*. Pearson Education Limited, 2001.

[191] H. J. C. Berendsen, J. P. M. Postma, W. F. van Gunsteren, A. DiNola, and J. R. Haak. *J. Chem. Phys*, 81:3684, 1984.

[192] K. Bolton, F. Ding, A. Börjesson, W. Zhu, H. Duan, A. Rosen, A. R. Harutyunyan, , and S. Curtarolo. Journal of Theoretical and Computational Nanoscience, Accepted 2008.

[193] D. Schebarchov and S. C. Hendy. *Nano Letters*, 8:2253, 2008.

[194] Wuming Zhu, Arne Rosén, and Kim Bolton. Changes in single-walled carbon nanotube chirality during growth and regrowth. *The Journal of Chemical Physics*, 128(12):124708, 2008.

[195] L. Ci, J. Suhr, V. Pushparaj, X. Zhang, and P. M. Ajayan. *Nano Letters*, 8:2762 – 2766, 2008.

[196] Yves De Smet, Lic Deriemaeker, and Robert Finsy. A simple comuter simulation of ostwald ripening. *Langmuir*, 13:6884 – 6888, 1997.

[197] P. W. Voorhees. *J. Stat. Phys.*, 38:231 – 252, 1985.

[198] A. S. Kabalnov and E. D. Shchukin. *Adv. Coll. Int. Sci.*, 38:69–97, 1992.